



VILNIUS UNIVERSITY
CENTER FOR PHYSICAL SCIENCES AND TECHNOLOGY
UNIVERSITÉ DE PAU ET DES PAYS DE L'ADOUR

Meera Stephen

**Charge Transport and Novel Poly(fullerene)s in
Organic Photovoltaics**

Doctoral thesis,
Technological sciences, Material engineering (08 T)

Vilnius, 2016

The work described in this thesis has been carried out at Vilnius University (Lithuania) and Université de Pau et des Pays de l'Adour (France) during 2013-2016.

This research has been funded by the European Union Seventh Framework Program (FP7-PEOPLE-2011-ITN) under grant agreement ESTABLIS no. 290022

Supervisors:

Prof. Dr. Gytis Juška (Vilnius University, Technological Sciences, Material Engineering – 08 T).

Dr. Roger C. Hiorns (Université de Pau et des Pays de l'Adour, Physical Sciences, Chemistry – 03P).

Acknowledgements

I would like to express my heartfelt gratitude to everyone who made this work possible, especially;

To Kris, Juška & Arlauskas, for taking me on as a PhD student, providing me with the opportunity to be part of Establis under their supervision.

To Roger, for the valuable guidance and constant encouragement throughout this time, that helped me to see it through.

To the frequent Establis meetings, which truly kept me going.

To Establis fellows, Anna, Alberto, Aurélien, Craig, Dargie, Graham, Hasina, Hugo, Isa, Jenia, Joanna, Mamadou, Shafkath, Simon & Stefan, for all the knowledge and fun we shared.

To my friends in Pau & Vilnius, Ariana, Aurélie, Bronè, Edilene, Eunkyung, HongYao, Julius, Nelly, Rayane & Shuanglong, for the much required company.

To Mélanie & Julija, for all the help with administration.

To my precious friends back home, who were up for a chat anytime I needed, regardless of the time-zone difference.

To my family, especially Kunjachan, for the endless support.

Abstract

Intense research in organic photovoltaics (OPV) during the past decade has been fuelled by the need for inexpensive renewable energy sources. OPV presents us with a new breed of coatable, semitransparent, potentially cheap, flexible photovoltaics that can be used in many applications where traditional photovoltaics cannot compete. Any progress in this field calls for the close cooperation of chemists and physicists owing to its very nature of interdisciplinarity.

This dissertation comprises of two distinct but interconnected topics. The first part consists of a detailed study of degradation behavior of working organic solar cell devices on prolonged exposure to simulated sunlight. Photo-induced charge carrier extraction by linearly increasing voltage (photo-CELIV) and time of flight (TOF) techniques are made use of to deduce the effects of photo-degradation on bulk charge transport in these devices. Firstly, benchmark devices based on P3HT:PCBM active layer are studied. Comprehensive investigations of charge carrier mobility, density and recombination are performed to get an insight into the irreversible degradation mechanism. An increased number of trapped charge carriers and enhanced bimolecular recombination is observed with progressive degradation, hinting at the destruction of the ideal nanomorphology of pristine P3HT:PCBM blends. Furthermore, the photo-degradation of a series of benzodithiophene (BDT) – diketopyrrolopyrrole (DPP) based polymers with different side-chains is documented. Analysis of extraction current transients indicated the progressive formation of trap states as being the most predominant effect influencing the process of charge extraction.

A second part of this work deals with synthesis of novel poly(fullerene)s for photovoltaic applications. A recently discovered route where the use of sterically cumbersome groups provided for a certain degree of control over the additions to the fullerene sphere is explored to provide for main-chain

poly(fullerene)s. The use of 2,5-bis(octyloxy)terephthalaldehyde and PCBM as co-monomers afforded high molecular weight, thermally stable polymers *via* the Sterically controlled Azomethine ylide Cycloaddition Polymerization (SACAP). Furthermore, the inclusion of large chromophore units to yield fullerene-dye alternating polymers and oligomers is proved to be feasible with the SACAP route, where DPP is co-polymerized with both C₆₀ and PCBM. This is the first time that alternating polymers containing dyes and fullerene in the main-chain have been prepared. Detailed characterizations using NMR (¹H, ¹³C and 2D HSQC), GPC, UV-Visible absorption, fluorescence emission, TGA and DSC are carried out to substantiate the structure and properties of these new materials. Moreover, their photovoltaic properties are validated by using them as acceptor materials in bulk heterojunction (BHJ) cells. They are found to yield high open circuit voltages relative to PCBM, as a result of raised LUMO levels, confirming predictions from modeling studies. The devices incorporating these novel materials were also found to be stabilized in response to thermal stress, their *burn-in* phases being greatly reduced. The reduction in short circuit currents on replacing PCBM with poly(fullerene)s in the BHJ is thought to be resulting from a non-ideal mixing with the donor polymer, a prospective for future studies.

Santrauka

Pastarąjį dešimtmetį atsinaujinančios energijos šaltinių poreikis skatino intensyvius nebrangių organinių saulės elementų (OPV - angl. Organic Photovoltaics) tyrimus. Dėka savo lankstumo, plastiškumo, galimybės padengti įvairius paviršius OPV gali būti naudojami įvairiose nišinėse srityse. Kadangi visos organinės elektronikos sritys pasižymi tarpdiscipliniškumu, todėl ir progresas OPV srityje reikalauja glaudaus chemikų bei fizikų bendradarbiavimo.

Ši disertacija susideda iš dviejų skirtingų, bet tarpusavyje susijusių, temų. Pirmąją dalį sudaro išsamūs saulės imitatoriumi apšviestų organinių saulės elementų degradacijos tyrimai. Fotogeneruotų krūvininkų ištraukimas tiesiškai kylančia įtampa (photo-CELIV - angl. photo-induced charge carrier extraction by linearly increasing voltage) ir lėkio trukmės (TOF - angl. time of flight) metodai buvo pasiteikti siekiant nustatyti fotodegradacijos įtaką krūvininkų pernašai šiuose elementuose. Pirmiausia buvo tirti plačiausiai paplitę P3HT:PCBM aktyvios srities elementai. Siekiant iširti negrįžtamą degradacijos mechanizmą buvo atlikti išsamūs krūvininkų judrio, tankio bei rekombinacijos tyrimai. Progresuojant degradacijai pastebėtas padidėjęs prilipusių krūvininkų kiekis bei išaugusi bimolekulinė rekombinacija, tai rodo idealios morfologijos, stebėtos nedegredavusiuose P3HT:PCBM bandiniuose, suardymą. Analogiškai tyrimai taip pat buvo atlikti su benzoditiofeno (BDT) – diketopirolopirolio (DPP) grupės polimerais, turinčiais skirtingas šonines grandines. Ekstrakcinių srovės kinetikų analizė leido nustatyti prilipimo būsenų susidarymą, kuris buvo vienas pagrindinių vyraujančių efektų, įtakančių krūvio ekstrakciją.

Šios disertacijos antrąją dalį sudaro fotovoltiniams prietaisams skirtų naujų polifulerenų sintetinimas. Neseniai atrastas erdviškai didžiulių grupių panaudojimo cheminėje sintezėje būdas, suteikia galimybę kontroliuoti atšakų prijungimo vietą bei patį polimerizacijos procesą. Naudojant 2,5-bis(oktiloksi)tereftalaldehidą bei PCBM ko-monomerus erdviškai

kontroliuojamoje azometino ilido ciklo prijungimo polimerizacijos reakcijoje (SACAP - angl. Sterically controlled Azomethine ylide Cycloaddition Polymerization) buvo gautas didelės molekulinės masės, termiškai stabilus polimerus. Taip pat, buvo įrodyta, kad didelių chromoforų panaudojimas leidžia sintetinti fulereno-dažų polimerus bei oligomerus ir tai įmanoma atlikti naudojant SACAP metodiką, pasitelkus DPP ko-polimerizuotą su C₆₀ bei PCBM. Tai yra pirmas kartas, buvo susintetinti polimerai, savo grandinėleje turintys organinio dažo fragmentą bei fulereną. Gautos medžiagos buvo charakterizuotos pasitelkus NMR (¹H, ¹³C ir 2D HSQC), GPC, sugerties spektrą, fluorescencijos emisiją, TGA bei DSC siekiant pagrįsti šių naujų medžiagų struktūrą bei savybes. Šių polifulerenų tinkamumas OPV buvo patvirtintas naudojant šias medžiagas kaip akceptorių tūrinės heterosandūros (BHJ - angl. bulk heterojunction,) celėse. Dėl aukštesnio LUMO lygmens (lyginant su PCBM) buvo nustatyta didesnė atviros grandinės įtampa nei naudojant PCBM, tai patvirtino modeliavimo rezultatus. Celės, pagamintos naudojant polifulerenus, yra stabilios šiluminiam stresui, todėl prognozuojamas jų tarnavimo laikas turėtų būti žymiai ilgesnis, nei naudojant PCBM. Manoma, kad trumpo jungimo srovės sumažėjimas celėse PCBM pakeičiant polifulerenais vyksta dėl neidealaus maišymosi su donoro polimeru.

Résumé

Au cours de la dernière décennie, des recherches intensives dans le domaine du photovoltaïque organique (OPV) ont été menées pour faire face aux besoins et à la nécessité de développer des sources d'énergie renouvelables bon marché. Les matériaux issus de cette technologie représentent une nouvelle génération de matériaux plastiques souples pouvant être utilisés dans de nombreuses applications où l'énergie photovoltaïque traditionnelle n'est pas compétitive. La majorité des progrès récents obtenus dans le domaine de l'OPV résultent d'une coopération interdisciplinaire étroite entre chimistes, physico-chimistes et physiciens.

Cette thèse se compose de deux sujets principaux. La première partie consiste en une étude détaillée des effets de la dégradation des dispositifs OPV après exposition prolongée à la lumière solaire artificielle. Les techniques « Photo-induced charge carrier extraction by linearly increasing voltage » (photo-CELIV) et temps de vol (TOF) ont été utilisées pour déduire les effets de la photo-dégradation sur le transport de charge dans les dispositifs organiques. Une première étude a été menée sur un système de référence basé sur une couche active constituée de P3HT:PCBM. Une étude approfondie de la mobilité des porteurs de charges, de la densité de charge et de la recombinaison a été menée pour obtenir un aperçu du mécanisme de dégradation irréversible. Un nombre accru de porteurs de charge piégés ainsi qu'un renforcement de la recombinaison bi-moléculaire ont été constatés au cours de la dégradation progressive du matériaux, menant à la destruction de la nano-morphologie idéale du mélange P3HT:PCBM. Basée sur ces conclusions, l'étude de la photo-dégradation de deux nouvelles séries de polymères et de leurs analogues possédant différentes chaînes latérales, i.e. benzodithiophene (BDT) et diketopyrrolopyrrole (DPP), a été menée dans ce travail. L'analyse des extractions de courants transitoires montre que la

formation progressive d'états de pièges prédomine le processus d'extraction de charge.

La seconde partie de ce travail concerne la synthèse de nouveaux matériaux de type poly(fullerène)s en vue d'applications pour le photovoltaïque organique. Une voie de synthèse récemment découverte, dans laquelle l'utilisation de groupes stériquement encombrants permettant de maîtriser les additions de polymères sur la molécule de fullerène, a été explorée dans ce travail pour assurer la formation des systèmes poly(fullerène)s de conformation contrôlée. L'utilisation conjointe des systèmes 2,5-bis (octyloxy)téréphtalique et du PCBM en tant que comonomères nous a permis d'obtenir des polymères thermiquement stables de haut poids moléculaires, *via* cette voie de synthèse appelée SACAP (« Sterically controlled Azomethine Ylide Cycloaddition Polymérisation »). En outre, cette technique de synthèse a rendu possible l'inclusion de grosses unités chromophores, conduisant à une macromolécule alternant polymères (fullerène) et oligomères (colorant). Cette synthèse fait appel à la copolymérisation du diketopyrrolopyrrole (DPP), à la fois par le fullerène et le PCBM, et a conduit pour la toute première fois à un polymère alterné associant fullerène et colorant. Une caractérisation fine, par RMN (^1H , ^{13}C et 2D HSQC), chromatographie en phase gaz, spectroscopie UV-visible, spectroscopie par émission de fluorescence, TGA et DSC, a été réalisée afin de prouver la structure de ces nouveaux matériaux et de justifier leurs propriétés. Par ailleurs, les matériaux ainsi obtenus ont été employés en tant qu'accepteurs en hétérojonction avec les deux accepteurs (C_{60} et PCBM), afin de tester spécifiquement leurs propriétés photovoltaïques. En accord avec les prédictions déduites des calculs théoriques, cette étude a prouvé que ces nouveaux matériaux, en comparaison du PCBM, conduisaient à une plus forte tension de circuit ouvert V_{oc} . De plus, les cellules constituées par ce type de matériaux se révèlent stables face aux contraintes thermiques. Ces travaux ouvrent de nombreuses perspectives, notamment concernant la recherche d'un donneur idéal associé au composés poly(fullerènes), ce qui devrait pouvoir permettre

d'améliorer de façon très significative la production de courant.

Table Of Contents

List of Abbreviations	13
Chapter 1 Introduction.....	15
1.1 Motivation	15
1.2 Photovoltaic Technology.....	16
1.3 Brief History of Organic Photovoltaics.....	17
1.4 Basic Principles of Bulk Heterojunction Cells.....	19
1.5 Theory of charge transport in disordered organic systems	24
1.5.1 Trap States.....	26
1.5.2 Charge Carrier recombination.....	28
1.6 Degradation in polymer solar cells.....	31
1.6.1 Photo-oxidation of active layer	33
1.6.2 Morphological stability	34
Chapter 2 Technique and Methods.....	38
2.1 Charge extraction by linearly increasing voltage (CELIV)	38
2.2 Time of Flight (TOF).....	42
2.3 Experimental setup.....	44
Chapter 3 Effects of Photo-Degradation on Charge Carrier Transport in P3HT:PCBM Solar Cells.....	47
3.1 Introduction.....	48
3.2 Degrading the devices	49
3.3 Results and Discussion	51
3.3.1 Equilibrium carrier concentration.....	51
3.3.2 Charge carrier mobility.....	53
3.3.3 Charge recombination studies	56
3.4 Conclusions	61

Chapter 4 Photodegradation in Encapsulated BDT-DPP based Solar Cells	62
4.1 Introduction	63
4.2 Experimental	67
4.3 Results and Discussion	68
4.4 Conclusion	74
Chapter 5 Novel poly(fullerene)s for photovoltaic applications	76
5.1 Introduction	77
5.2 Synthesis & characterization of PPCBMB	81
5.3 Synthesis & characterization of PDPF and PDPPCBM	95
5.4 Conclusions	110
Chapter 6 Photovoltaic properties and thermal stabilizing effects of poly-(pyrrolidino)fullerenes	111
6.1 Device fabrication procedure	113
6.2 P3HT:poly(fullerene) based devices	113
6.3 Exploring more donor systems	118
6.4 Thermal Stability Studies	123
6.5 Conclusions	126
Summary	128
Appendix 1	130
Appendix 2	138
References	149

List of Abbreviations

AM – air mass

BHJ – bulk heterojunction

BDT - benzodithiophene

CELIV – charge carrier extraction by linearly increasing voltage

CdTe – cadmium telluride

C₆₀ – buckminsterfullerene

CT – charge transfer

DOS – density of states

DPP – diketopyrrolopyrrole

DSC - differential scanning calorimetry

EQE - external quantum efficiency

EBL – electron blocking layer

eV – electronvolt

FF – fill factor

GaAs – gallium arsenide

GPC – gel permeation chromatography

HOMO - highest occupied molecular orbital

ITO - indium tin oxide

J_{sc} – short circuit current

LDA – lithium diisopropylamide

LUMO – lowest unoccupied molecular orbital

M_n - number-average molecular weight

M_w - weight-average molecular weight

M_p - peak molecular weight

NMR - Nuclear magnetic resonance

NREL – National Renewable Energy Laboratory

O.D – optical density

OSC – organic solar cells
OPV – organic photovoltaics
PCBM - phenyl-C₆₁-butyric acid methyl ester
PCE - power conversion efficiency
PDPF – poly[(dodecyl dithiophene-diketopyrrolopyrrole)-*alt*-bispyrrolidinofullerene]
PDPPCBM – poly[(dodecyl dithiophene-diketopyrrolopyrrole)-*alt*-(bispyrrolidino-phenyl-C₆₁-butyric acid methyl ester)]
PEDOT:PSS - poly(3,4-ethylenedioxythiophene):poly(styrenesulfonate)
PPCBMB – poly{[bispyrrolidino(phenyl-C₆₁-butyric acid methyl ester)]-*alt*-[2,5-bis(octyloxy)benzene]}

PPV – poly(p-phenylene vinylene)
P3HT - poly(3-hexylthiophene)
PV – photovoltaics
SACAP – sterically controlled azomethine ylide cycloaddition polymerization
TOF – time of flight
THF - tetrahydrofuran
TGA - thermogravimetric analysis
UV - ultraviolet
 V_{oc} – open circuit voltage

Chapter 1

Introduction

1.1 Motivation

Increasing global energy demand and raising concerns of preserving the environment has urged humankind to look for fossil fuel free alternatives.¹ Research in renewable energy is moving to the forefront in a variety of fields owing to its increasing relevance in today's world. Among various renewable energy technologies, solar energy is an incredibly abundant² and extremely clean source, which remains underexploited to date.³ The growth of solar photovoltaics (PV) has been tremendous recently, with more than 60% of all PV capacity in operation worldwide by the end of 2014 being added over the past three years.⁴ However, in developing and emerging economies, obtaining PV installations at affordable rates remains a common challenge.

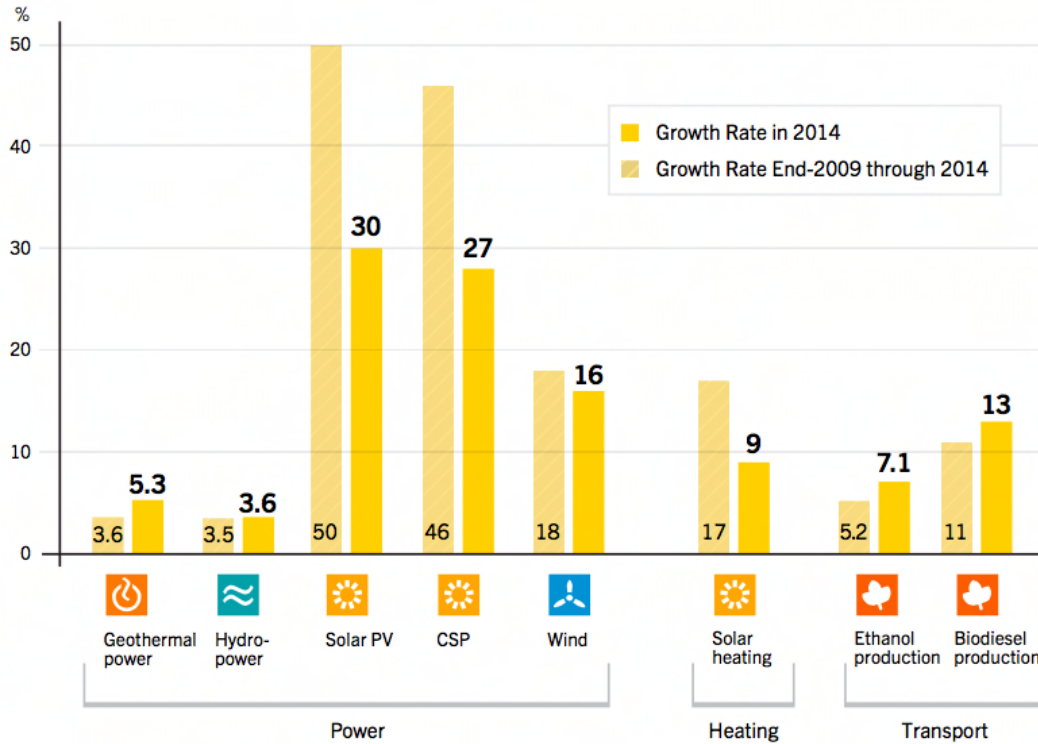


Figure 1.1 Average global growth rates of various renewable energy sources, reproduced from ref. 4

1.2 Photovoltaic Technology

The first practical photovoltaic cell was developed in 1954 at Bell Laboratories, which soon became popular for space applications.⁵ The field of PV technology has since seen many innovations and is traditionally divided into three generations. The first generation is mainly based on mono/polycrystalline Si wafers, second generation on amorphous Si and other thin film technologies such as CIGS and CdTe, and finally the third generation based on organic materials.⁶

The use of organic materials for photovoltaic applications can potentially reduce the fabrication costs and enable bulk production of modules *via* printing processes. The most exciting aspect of this kind of solar cells is perhaps their light weight and flexibility, making them promising for niche applications such as building integrated photovoltaics, smart windows (which are partially transparent)

and custom designed products. This is already realized by Belectric OPV GmbH in their recent series of customized solar cells under the name *solarte* as well as *HeLi-on*, a compact solar charger marketed by infinityPV ApS, a Danish start-up company founded by Frederik C. Krebs.



Figure 1.2 'Solarte' by Belectric.

The world record efficiency for organic solar cells (OSC) stands at ~12% today as certified by the National Renewable Energy Laboratory (NREL).⁷ Last decade has seen a steady growth in efficiencies of these devices but their relatively low stability remains a bottleneck, which is still poorly understood.

1.3 Brief History of Organic Photovoltaics

The first organic solar cell devices were made with light absorbing small organic molecules (dyes), developed by the group led by Dr. Ching Tang at Kodak Research Laboratories in 1986.⁸ The use of organic materials in solar cell technology is attractive owing to a number of advantageous features including low manufacturing energy requirements, low weight, mechanical flexibility, tunable material properties and high transparency.⁹ The pioneering work of A. Heeger, A. MacDiarmid and H. Shirakawa in semi-conducting polymers provided new

dimensions for OPV research.¹⁰ These are carbon-based materials whose backbones are comprised mainly of alternating C–C and C=C bonds, the semiconducting properties arising from electron delocalization along the conjugated backbone. Polymer materials generally have better film forming quality, befitting wet processing like inkjet printing, die-coating, etc. desirable for the fabrication of large scale devices. One of the major differences between organic semiconductors and inorganic semiconductors is the presence of tightly bound excitons (electron–hole pairs) resulting from their low dielectric constant ($\epsilon_r \approx 2 - 4$). The binding energy of these so-called ‘Frenkel excitons’ is in the range of 0.3–1 eV as opposed to 1–40 meV in inorganics.¹¹ Another important difference from crystalline, inorganic semiconductors is the relatively small diffusion length of primary photoexcitations (excitons) in these rather amorphous and disordered organic materials.¹² The relatively poor efficiencies of the initial single organic layer devices were boosted by the introduction of bilayer heterojunctions. Tang reported in 1986 about 1% power conversion efficiency for two organic materials (a phtalocyanine derivative as p-type semiconductor and a perylene derivative as n-type semi-conductor) sandwiched between a transparent conducting oxide and a semitransparent metal electrode.¹³ The energy difference between the lowest unoccupied molecular orbital (LUMO) of the donor and highest occupied molecular orbital (HOMO) of the acceptor could now serve as the driving force for the dissociation of the Frenkel excitons and consequently better efficiencies could be obtained. The observation of an extremely fast photo-induced electron transfer from optically excited conjugated polymers to the C₆₀ molecule (~50-100 fs) in the early 1990s led to the development of polymer–fullerene bilayer heterojunction devices.^{14,15,16} A further breakthrough was the concept of bulk heterojunction (BHJ)¹⁷, where the active layer was deposited from a physical blend of the polymer with fullerene, thereby increasing the donor–acceptor interfacial area leading to more efficient exciton dissociation. Typically,

a more soluble methanofullerene derivative of C₆₀ buckyball, phenyl-C₆₁-butyric acid methyl ester (PCBM) is used in BHJs and remains by far the most commonly used n-type component in organic photovoltaics, after its first successful synthesis by Fred Wudl's group.¹⁸

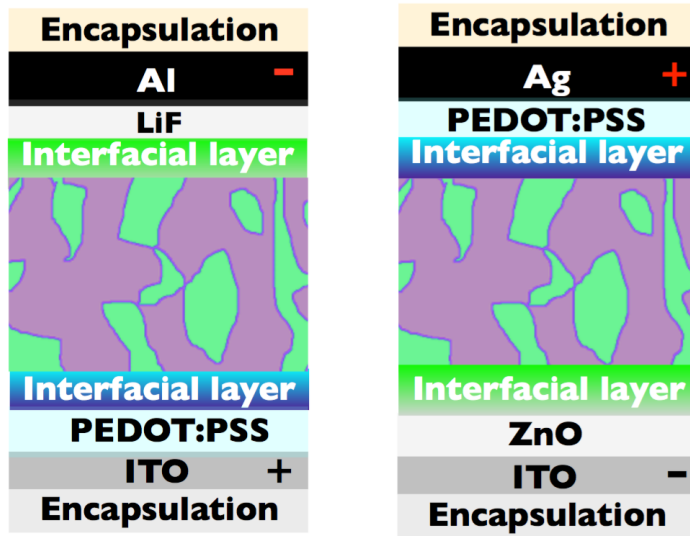
Even though the recent record for highest research cell efficiencies certified by NREL (quoted in the previous section) belongs to a polymer : fullerene BHJ system,¹⁹ non-fullerene acceptors have been gaining momentum lately, with rather high efficiencies of 11% being reported for indacene based small molecule acceptors.²⁰ Small molecule based OSCs with fullerene acceptors are reported to have efficiencies of 9%, with their unique benefits of simplified purification as opposed to long hours of washing to remove lower molecular weight products in the case of polymers and elimination of batch to batch variations, resulting in more well defined products.²¹ Polymer : polymer BHJ systems, where both donor and acceptor moieties are polymers, have also received considerable attention owing to the improved molecular flexibility of both donor and acceptor groups. Improved film forming properties and higher absorption coefficients are additional qualities to their credit.²² Albeit reduced electron mobilities and formation of large phase separated domains in active layer blends were encountered in many of the tested systems, recent reported efficiencies of 8% makes them as competent.²³

1.4 Basic Principles of Bulk Heterojunction Cells

The archetypal OPV device today (figure 1.3) consists of an active light absorbing BHJ layer of donor polymer/ small molecule with an acceptor molecule, like fullerene, sandwiched between two electrodes with different work functions. Intermediate layers called charge extraction layers are included for better charge transport by selectively blocking one type of charge carriers. Indium tin oxide

(ITO) is traditionally used as the transparent conducting electrode. A layer of poly(3,4-ethylenedioxythiophene)/poly(styrenesulfonate) (PEDOT:PSS) serves as the hole transport layer in many devices in use today. Additionally the PEDOT:PSS is known to smoothen the surface imperfections and reduce the surface roughness of ITO.²⁴ Upon illumination, the fraction of photons absorbed by photo-active layer induces electron excitation from its HOMO to LUMO creating neutral Frenkel excitons either in the donor or acceptor material. Excitons migrate and charge transfer occurs at the donor-acceptor interface, if it exists within the diffusion length. The exact mechanism by which electrons and holes overcome the Coulomb trapping is still unsolved, but increasing evidence points to the critical role of hot charge-transfer (CT) excitons in assisting this process.^{25,26,27} In the absence of a donor-acceptor interface to dissociate the excitons into free charge carriers, the excitons can undergo radiative and nonradiative decay, with a typical exciton lifetime in the range from 100 ps - 1 ns.²⁸ Once free charge carriers are generated, they are extracted and collected by the selective contacts. Hence, the external quantum efficiency (EQE) as a function of wavelength (λ) is the ratio between the number of collected photogenerated charge carriers and the number of incident photons, and is ultimately the product of four efficiencies (η): absorption (A), exciton dissociation (ED), charge separation (CS) and charge collection (CC), giving EQE (λ) = $\eta_A(\lambda) \times \eta_{ED}(\lambda) \times \eta_{CS}(\lambda) \times \eta_{CC}(\lambda)$.

(a)



(b)

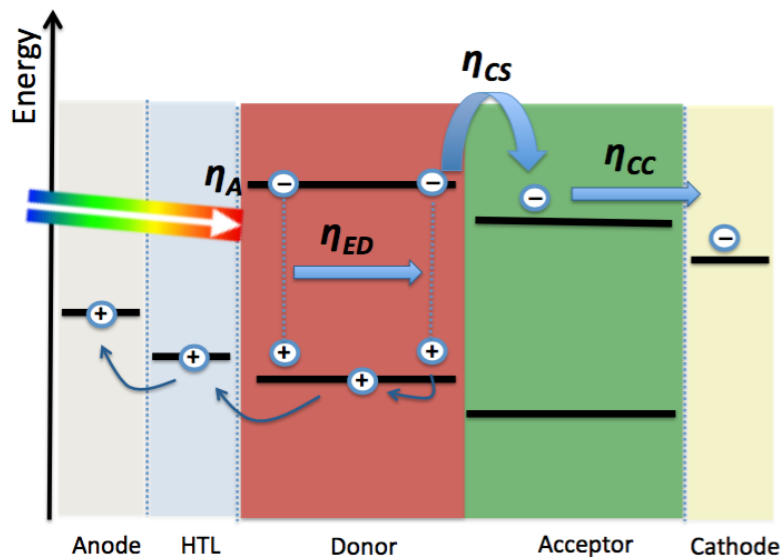


Figure 1.3(a) normal (left) and inverted (right) device architectures of an OPV cell; in the normal geometry the transparent electrode (ITO) serves as the positive electrode, and the metal electrode (Al) is the negative electrode. In the inverted geometry the two electrodes and the charge selective layers are switched around, such that ITO is the negative electrode and the high work function metal (Ag) is the positive electrode; **(b)** is a schematic of the cascade of energy levels across different layers of the device and the series of different processes which constitutes the photovoltaic performance.

An essential figure of merit to characterize solar cells is the power conversion efficiency (PCE), which is defined as the ratio of energy output from the solar cell to input light energy. It is calculated from the current-voltage (I - V) characteristics (Fig. 1.4) of the cell under illumination, as

$$\eta = \frac{P_{out}}{P_{in}} = \frac{I_{sc}V_{oc}FF}{P_{illumination}}$$

where I_{sc} is the short circuit current, V_{oc} is the open circuit voltage and $FF = \frac{I_m V_m}{I_{sc} V_{oc}}$ is the fill factor representing the maximum area in the fourth quadrant of the I - V curve under 1 sun. The globally used standard of 1 sun corresponds to an irradiation intensity of 1000 W/m^2 and the solar spectrum corresponding to air mass (AM) 1.5. Here AM indicates the amount of atmosphere sunlight must travel through to reach the earth's surface and AM1.5 describes the spectrum when the sun is at a zenith angle²⁹ of 48° .

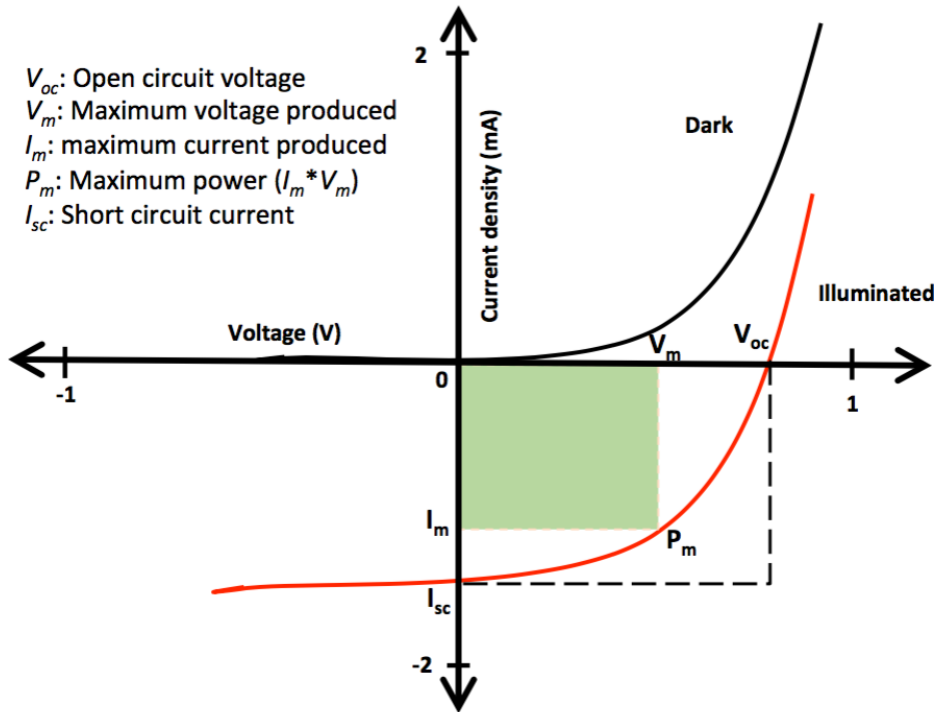


Figure 1.4: Schematic current-voltage characteristics of a solar cell, adapted from ref

In general, a combination of techniques are necessary to study the cascade of events from absorption to charge collection, as they occur at different time scales after illumination, within the BHJ device. The singlet exciton in organic materials is reported to have a lifetime of around 1 nanosecond³¹ while charge transfer in the presence of an acceptor like fullerene is an ultrafast process, occurring on the order of tens of femtoseconds.³² Briefly, the exciton can dissociate when its energy is larger than the energy of the electron–hole pair after the electron transfer, often called a polaron pair or a charge transfer complex.^{33,34} The energy gain herein is therefore not as straightforward as implied by some publications, where it is described as the energy offset between the LUMO of the donor and the LUMO of the acceptor. The immediate step after exciton dissociation is the formation of a Coulomb bound polaron pair which can either geminately recombine or dissociate into free charges, whose probability depends on the existent electric field, as given by Onsager-Braun model.³⁵

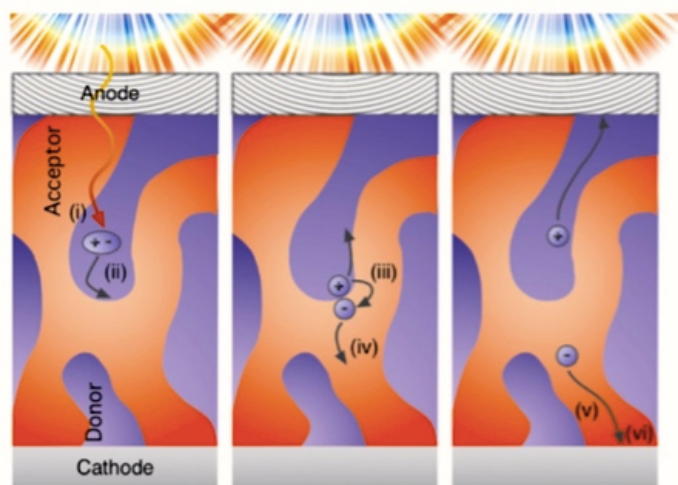


Figure 1.5: From light absorption to photocurrent in a bulk heterojunction solar cell, from a kinetic point of view, (i) singlet exciton generation from an absorbed photon in the donor material. (ii) diffusion of exciton to the acceptor interface. (iii) dissociation of exciton by electron transfer to the electronegative acceptor molecules. (iv) separation of the still Coulomb-bound electron–hole pair (v) charge transport of electron and respective hole by hopping between localized states. At this state, nongeminate recombination between independently generated electrons and holes can occur. (vi) extraction of the charges - photocurrent. Reproduced from ref. 31

1.5 Theory of charge transport in disordered organic systems

As mentioned in section 1.3, the alternating double bonds present in the back-bone of semi-conducting organic systems gives rise to their interesting electronic properties. Both small molecules and polymers of interest in this context comprise of a conjugated π electron system formed by the p_z -orbitals of sp^2 - hybridized C-atoms in these molecules. Since the π -bonding is significantly weaker than the σ bonds forming the back-bone of the molecules, the electrons are delocalized along the overlapping orbitals, giving rise to conjugation. Due to the lesser degree of overlap of p_z -orbitals, the resulting molecular π and π^* orbitals are less bonding or antibonding, thus forming the frontier orbitals of the molecule.³⁶ Therefore, the lowest electronic excitations of conjugated molecules are the π (bonding) – π^* (antibonding) transitions, corresponding to the highest occupied molecular orbital (HOMO) and lowest unoccupied molecular orbital (LUMO), respectively.³⁷

The energy levels become closely spaced as the delocalization length increases, (Fig. 1.6) giving rise to band like transport somewhat similar to that observed in inorganic solid state semiconductors in perfectly oriented crystals. However, since organic molecular crystals are van der Waals bonded solids, the intermolecular bonding is considerably weaker compared to covalently bonded semiconductors like Si or GaAs. This results in a much weaker delocalization of electronic wavefunctions among neighbouring molecules and hence a rather small bandwidth.³⁶ This has direct implications for optical properties and charge carrier transport, and room temperature mobilities in highly purified molecular crystals only reach values of 1 to 10 cm^2/Vs , which is two orders of magnitude less than in polycrystalline Si.³⁸

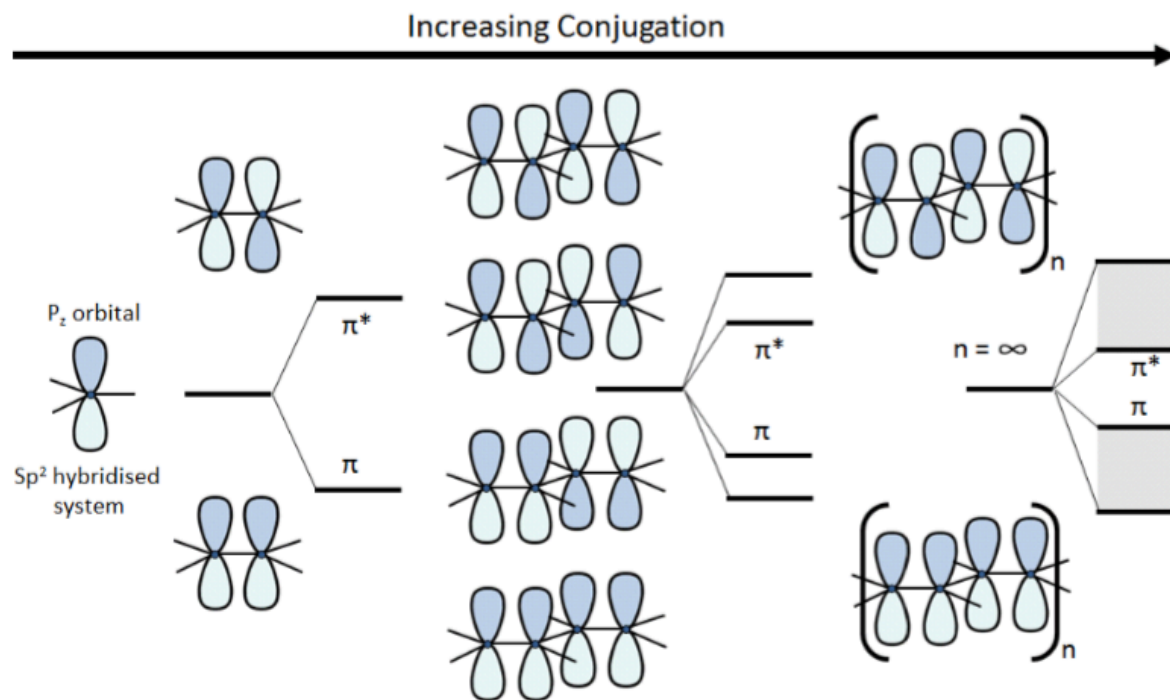


Figure 1.6: P_z orbitals of a conjugated system interact to form the Frontier Molecular orbitals. An array of atoms with efficient orbital overlap gives rise to a band like structure, reproduced from ref. 39

In going from molecular crystals to disordered organic solids, the transport properties are significantly affected by anisotropy arising from locally varying polarization energies due to different molecular environments.⁴⁰ This leads to random spatial distribution of absolute values of molecular energies and a Gaussian density of states for the distribution of transport sites. Experimentally, this is observed as an inhomogeneous broadening of optical spectra such as absorption, fluorescence and phosphorescence spectra. In the case of semi-conducting polymers, further inhomogeneity is brought about by the torsional disorder along the chain, which manifests itself in varying lengths of conjugated segments within a single polymer chain. Accounting for such inhomogeneity, the charge transport in disordered organic systems is best explained by the scenario of incoherent hopping of carriers via randomly distributed localized states. This

forms the core of Bässler's formalism⁴¹ where the energy of sites within the Gaussian distribution is given by

$$g(E) = \frac{N}{\sigma\sqrt{2\pi}} \exp\left(\frac{-E^2}{2\sigma^2}\right)$$

where E is the energy measured relative to the center of the density of states, σ is the standard deviation (width) of the Gaussian distribution of states (also called disorder-parameter), and N is the concentration of localized states that charge carriers can use for hopping transport.³⁶ The variation in intersite energy is termed as diagonal disorder while variations in intersite distances or positional disorder is termed off-diagonal.⁴² From his Monte Carlo simulations, using the Miller–Abrahams hopping rate, Bässler found the charge carrier mobility to depend on temperature T and field F :

$$\mu_{GDM} = \mu_{\infty} \exp\left(-\left(\frac{2\sigma}{3kT}\right)^2 + C\left(\left(\frac{\sigma^2}{kT}\right) - \Sigma\right)F^{1/2}\right)$$

Σ corresponds to spatial disorder, C and $2/3$ are scaling factors from the parametric fits. Thus the model accounts for reported dependencies of $\ln \mu \propto F^{1/2}$ and $\ln \mu \propto 1/T^2$ observed experimentally.

1.5.1 Trap States

Electrical transport is always accompanied by more or less frequent capture of the involved charge carriers in localized states. Such trapped carriers may be released after a specific retention period or may recombine with carriers of opposite charge. Traps are also classified as shallow or deep depending on their release time, even though it is hard to make a clear distinction. Classical semiconductor physics interprets trap states as energy sites situated in the energy gap of the semiconductor. In other words, each localized state below the conduction band edge, which is able to capture an electron, is an electron trap and each localized state above the valence band edge, which is able to capture a hole, is a hole trap.

In the case of strongly localized molecular states in amorphous organic systems, a distinction between trapped and regular transport sites is not obvious. The concept of transport energy level, which was first introduced for inorganic semiconductors⁴³ and later extended to organic systems^{44,45} comes across as a useful tool to this end. The transport energy level is analogous to band edge or mobility edge in inorganic semiconductors. It describes the energy level from which a trapped carrier is most probably released to move to a neighboring site and only has a statistical meaning. Consequently, each state below the transport energy level is a trap state while states above are regular transport sites. The transport energy is a function of temperature and hence a state acting as trap state at room temperature may become a transport site at lower temperatures.³⁶ The trap states maybe contributed by the inherent sites present in the tail of Gaussian DOS, arising from structural defects or additionally from presence of extrinsic impurities. An estimation of trap states can be experimentally obtained by the technique of thermally simulated currents. This technique uses a linear temperature ramp to thermally release trapped charge carriers and the resulting current is recorded as function of temperature.

The experimental findings of a carrier concentration dependent mobility,⁴⁶ due to filling of the Gaussian density of states, where lower states act as charge traps, were simulated by a hopping master equation approach and fitted parametrically, yielding an empirical description which is sometimes termed the enhanced Gaussian disorder model.⁴⁷

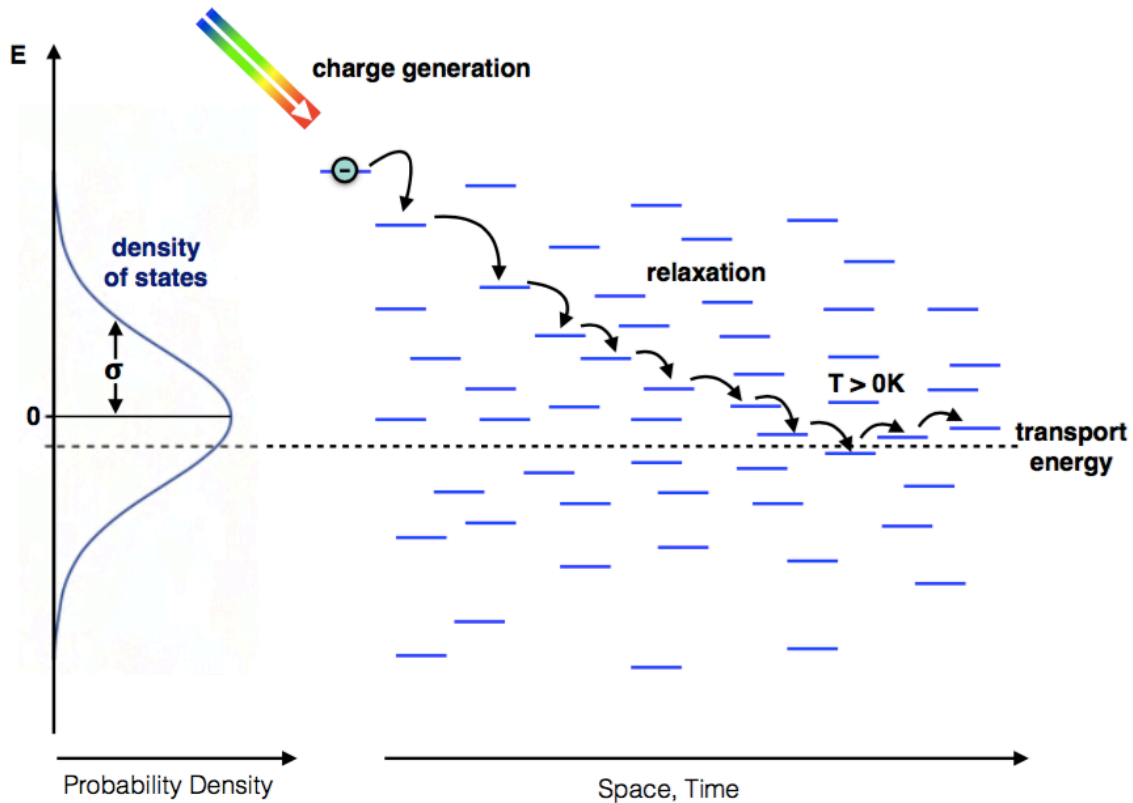


Figure 1.7: Schematic view of charge carriers transport by hopping between localized states with a Gaussian energy distribution and disorder parameter σ . Photogenerated (or injected) charge carriers can be generated at higher energies, followed by a relaxation of the charge carriers to a quasi-equilibrium. The steady-state charge transport takes place around the effective transport energy, which depends mainly on temperature and disorder. At 0 K temperature, the charge carriers relax to the deepest states where they remain trapped. Adapted from ref. 31

1.5.2 Charge Carrier recombination

During the transport of separated charge carriers to respective electrodes, the charge carriers can non-geminately recombine and no longer contribute to photocurrent. The order of recombination is, in principle, determined by the number of participants, and is thus crucial for the understanding of the origin of the loss mechanism. The dynamics of charge carrier density is given by the continuity equation

$$\frac{dn}{dt} = G - \beta n^2 - \frac{n}{\tau}$$

where G is the charge carrier generation rate, β is the bimolecular charge carrier recombination coefficient and τ is the carrier lifetime. (βn^2 quantifies bimolecular recombination rate and n/τ stands for monomolecular decay).

The type (order) of dominant recombination mechanism at a given point in time after photo-excitation depends on the density of mobile charges present relative to the trapped ones. Recombination of a mobile charge with a trapped carrier is considered to be a first order process, despite the participation of two constituents, if the density of trapped charges clearly exceeds the number of mobile ones, therefore seeming inexhaustible. If the concentration of trapped charges is similar or lower compared with the mobile ones, the bimolecular decay will indeed be of second order.³¹ In contrast, geminate recombination is considered monomolecular since both participants originate from the same initial state.

In low-mobility materials the second order recombination is expected to follow Langevin's theory,⁴⁸ with a recombination rate given by

$$R = \beta_L (np - n_i^2)$$

where n -electron concentration, p -hole concentration and n_i is the intrinsic carrier concentration.

In a homogenous medium, the Langevin bimolecular recombination coefficient β_L is directly related to the charge carrier mobility μ and is given by:

$$\beta_L = \frac{q}{\epsilon \epsilon_0} (\mu_e + \mu_h)$$

where q is the elementary charge, $\epsilon \epsilon_0$ the effective dielectric constant of the

medium, μ_e and μ_h the electron and hole mobilities, respectively.

Several experimental investigations have shown that in bulk heterojunctions, the observed bimolecular recombination is much weaker than predicted by Langevin.^{49,50} Explanations have been attempted based on the notion that the charge carriers are spatially separated due to the blend morphology, where electrons and holes reside in the acceptor and donor material, respectively, and can only recombine at the heterointerface, in contrast to Langevin's assumption of a homogenous medium. Thus, an additional factor for reducing the Langevin recombination strength γ is often encountered in reports on recombination studies and in some cases is inferred as a direct indicator of the percolative connectivity of the active layer blend.⁵¹ The direct relation between recombination and mobility in the Langevin equation also exemplifies the non-triviality of correlating separate parameters to overall efficiency of charge transport.

On a macrosecond timescale, considering a low conductivity regime where diffusion is negligible, the current through a material is given by the charge carrier density n and the carrier drift velocity v , where the latter is the product of mobility μ and electric field F ,

$$j = env = en\mu F$$

It is important to note that since both mobility and density can depend on applied electric field, a linear dependence of j on F is not obvious in case of disordered organic systems.³⁶

It is clear that knowledge of charge carrier mobility, density and their dynamics are pivotal to the understanding of performance of any photovoltaic device. Several techniques such as photo-induced carrier extraction by linearly increasing voltage (photo-CELIV), time of flight (TOF), double injection (DoI), Field effect transistors (FETs), space charge limited currents (SCLC), impedance spectroscopy, etc. are utilized for the characterization of charge transport in organic semiconductors. The work described herein makes use of photo-CELIV

and TOF techniques to study charge transport in working and degraded solar cell devices and will be further discussed in Chapter 2.

1.6 Degradation in polymer solar cells

Extensive research efforts through recent years have led to innovations in material and device engineering, greatly improving our understanding and contributing to achieving power conversion efficiencies (PCE) not far from the commercialization threshold.^{52,53}

As stated by M. Jørgensen *et. al.*,⁵⁴ there is however at least two other important factors that enters the recipe for successful marketing of OPV technology, one of them being lifetime and other one being the cost of processing. Only a combined progress in all these three areas will truly benefit the technology in terms of any application, which is termed ‘the unification challenge’.

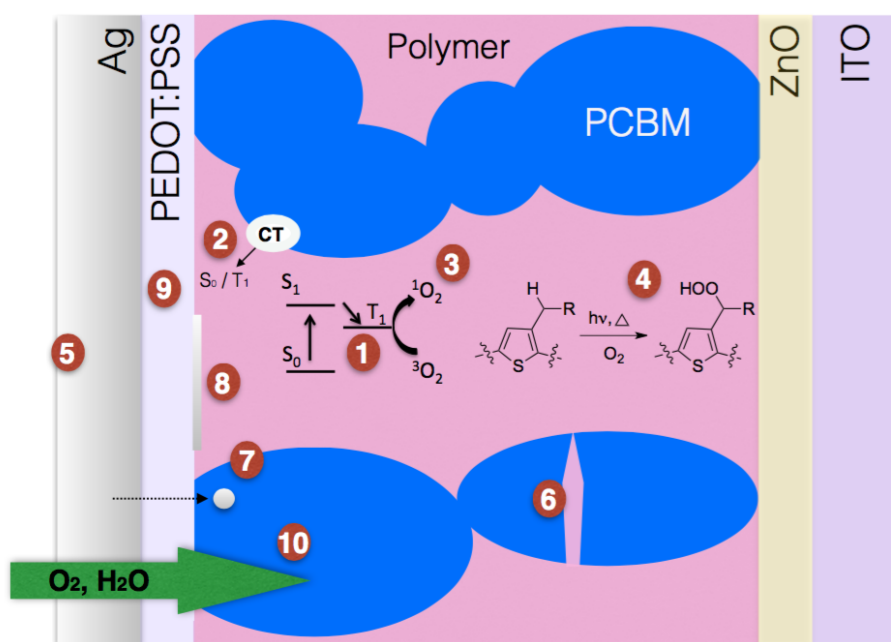


Figure 1.8 Schematic showing some of the degradation processes that commonly occur in organic solar cells, 1 - triplet formation; 2 - triplet formation from charge-transfer complex; 3 - singlet oxygen production; 4 - oxidation of polymer; 5 - oxidation of electrodes; 6 - morphological changes; 7 - diffusion of metal ions; 8 - delamination; 9 - poor conductivity and 10 - diffusion of H₂O and O₂.

The issue of degradation in polymer solar cells is rather complex owing to the plethora of degradation pathways that occur within the many layers comprising the device architecture (figure 1.8). Currently, significant literature can be found on this problem, including some excellent reviews,^{54,55,56} and lifetimes of several years has been achieved in few well-studied systems^{57,58} as a result of growing interest in this area. It is unfortunate that many of the systems used in the active layer blend often follow their own unique mechanism of degradation, which limits the development of a generalized model system. Research has identified numerous factors such as oxygen,^{54,59} water,^{60,61,62} light,^{63,64,65} heat^{66,67,68} and mechanical stresses^{69,70} as some of the crucial degradation triggers. Decline of photovoltaic performance with time is largely due to a combined action of several interrelated mechanisms taking place at different locations of the device, at specific kinetics. This often makes the realization of a holistic understanding and the identification of specific root causes of degradation challenging.⁷¹ Several strategies are employed to address either one or a combination of these degradation pathways. Use of an inverted device architecture where electrons flow from the high work function metal electrode to the transparent electrode, was found to be rather stable to water ingress while oxygen induced degradation was only partially addressed.⁷² Nevertheless, many groups further reported enhanced PCE and considerably improved lifetimes for inverted devices in the presence of both air and water.^{73,74,75,76} In P3HT:PCBM blends, the vertical phase segregation due to the different surface energy of the two components is found to be beneficial for inverted architecture.⁷⁷ Similar novel ideas in terms of device engineering^{78,79} have evidently contributed to addressing the issue of degradation and is still an active area in research. However, the work described herein is focused on the stability of the photo-active layer itself during long times of operational conditions and only this aspect will be discussed further.

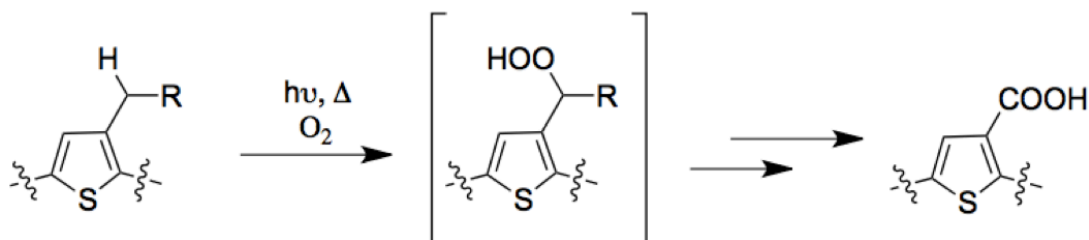
Considering the stability of photo-active layer, two crucial topics to be discussed are photo-oxidative stability and nano-morphological evolution of the active layer once being cast as a thin film.

1.6.1 Photo-oxidation of active layer

Most active layer polymers are stable to light in inert atmosphere. However they are prone to photo-oxidation as was evidenced by the fairly rapid photochemical decomposition of polyphenylenevinylene (PPV) based polymers in the early days of research. Initial work by S. Chambon *et al.* found that photo-oxidation by *via* abstraction of hydrogens on the carbon atom in the α position to the oxygen leads to a reactive radical species and hence a propogative reaction.^{80,81} However, recent studies found that the insertion of oxygen between the aromatic group and the alkyl side-chains actually reduces this photo-degradative pathway, in effect aromatic-oxy-alkyl side-chains can be preferably chosen while designing intrinsically stable molecules.⁸²

It was also observed that the presence of PCBM largely reduced the rates of degradation of blend films owing to its radical scavenging properties.⁸³

The succeeding work-horse material, the poly-3-hexylthiophene (P3HT), was found to be much more stable⁸⁴, following a different degradation pathway. The photo-oxidation was found to be triggered by the oxidation of side-chain starting with a hydroperoxide formation at the benzylic position as shown in Scheme 1.1⁸⁵



Scheme 1.1. Photo-oxidation mechanism of P3HT, reproduced from ref. 54

As observed for PPV based polymers, addition of PCBM was found to considerably lower the rate of the process in P3HT:PCBM blends⁸⁶ although further studies showed that oxidation of PCBM also formed traps for electron transport, thereby reducing the mobility of these blends.⁸⁷ The formation of an excited charge transfer complex between P3HT and oxygen was reported⁸⁸ resulting from photo-induced electron transfer from polymer to oxygen. Seemann *et al.* interestingly reported the partial reversibility of current density loss in P3HT:PCBM based devices, attributed to the p-doping of active layer by oxygen.⁸⁹

Stability studies of numerous polymers as neat and in blends with PCBM have been studied to date, notably by Manceau *et al.*,⁹⁰ who prepared a list of relative stability of most commonly used monomers, as a guide to consider while designing novel systems. General consensus from these studies is that the much desired alkyl side-chains which render these systems soluble enough to be solution processed, also deliver them prone to degradation. It is interesting to note that sometimes minor structural variations can have profound stabilizing effects, as demonstrated by the substitution of carbon by silicon in cyclopentadithiophene.⁹¹

1.6.2 Morphological stability

Active layer BHJs consisting of a mix of conjugated polymers and modified fullerenes often form phase-separated microstructures arising from limited polymer-fullerene miscibility. While maximizing the interfacial area facilitates exciton dissociation, reasonably sized pure domains are required for efficient charge transport to electrodes by forming complementary percolative pathways that minimize charge recombination.⁹² Many studies have shown that the performance of the device as a whole is linked to the morphology of the blend film, *i.e.*, the packing of molecules and size of domains formed. The active layer morphology can be controlled by varying parameters, like chemical

composition,^{93,94} choice of solvent,^{95,96} presence of additives^{97,98} and post-deposition techniques like thermal annealing^{99,100} or slow drying.¹⁰¹ While such developments definitely helped improve the device performance, it is now recognized that the microstructure evolves over time once it has been formed during production of the device. Small organic molecules like PCBM tend to diffuse slowly or recrystallize over time especially at elevated temperature.¹⁰² The best structure for device performance will in all probability not be the thermodynamically most stable. Such gradual changes in the microstructure eventually leads to a decline of the photovoltaic performance of the concerned devices. While many of the degradation pathways can be reduced to some extent by employing efficient barrier layers, degradation arising from morphological evolution needs to be addressed intrinsically. Morphology changes are clearly observed with prolonged times of device operation where the presence of light and temperature are inevitable.

PCBM is found reasonably well dispersed within the donor polymer rich phase after initial processing.¹⁰³ Under elevated temperatures typically reached during realistic working conditions, the enhanced molecular mobility acquired enables the PCBM molecules to diffuse through the film to form aggregates.¹⁰⁴ This lateral phase separation is found to enhance the PCEs during the initial few minutes (for temperatures $\sim 100^{\circ}\text{C}$) in blends with crystalline systems like P3HT due to improved percolation paths.¹⁰⁵ However, at longer times (>30 min) larger domains of the order of tens of micrometers are formed by molecular diffusion of PCBM out of the polymer matrix.¹⁰⁶ This clustering behavior, that starts from nuclei that can form under the presumption that the system is sufficiently saturated with its dispersed phase, and grows by adsorbing very small particles that diffuse toward them, fits into the theory of Ostwald ripening, which is an act of lowering the overall energy in the system.¹⁰⁷ Above a certain concentration, the PCBM crystals also provide mechanical stress on the metal electrode, therefore possibly

damaging the interface.¹⁰⁰ The major consequence of temperature on BHJ devices is thus the reduced interfacial area between the donor polymer and the acceptor fullerene. Electrically, this means that the current drawn from the device under illumination at short circuit drops.^{106,108}

Additionally, in the presence of light, PCBM is prone to dimerization in solution¹⁰⁹, neat films¹¹⁰ as well as potential active layer blends.¹¹¹ While the process of dimerization reduces the density of nucleation sites, it does not stop the growth of clusters.¹¹² The photo-induced dimerization and subsequent polymerization of fullerenes was found to occur in inert atmosphere by a [2+2] cycloaddition between (6,6) bonds on two adjacent fullerene cages^{113,114} and was found to be reversible at temperatures of *ca* 100 °C.¹¹⁵ Oxygen greatly inhibits this process, attributed to O₂ molecules quenching the photoexcited triplet state, which is thought to be a necessary precursor to the photo-polymerization process.¹¹⁵ In addition, light exposure has been reported to greatly accelerate the diffusion of any present O₂ molecules into interstitial voids of the fullerene lattice in the neat solid phase, ultimately forming oxidized fullerene end-products instead.¹¹⁶ Such photochemical reactions in the fullerene phase were reported to drive the intrinsic photo-degradation in many active layer blends in inert atmosphere.¹¹⁷

Thus, it is essential to develop strategies to “lock” the desired morphology achieved after the deposition of the active layer, which is extremely non-trivial, due in part to the fullerene derivatives miscibility in the polymer phase, where they readily diffuse throughout the polymer on short timescales.

Chemically cross-linking either or both the materials in the BHJ after deposition is a rationally adopted strategy to avoid aggregation of fullerenes into large domains.¹¹⁸ Photo-oligomerization of PCBM on low-level light exposure of already formed active layer films were reported to be beneficial in stabilizing the polymer:PCBM active layer morphology and enhancing the device stability under thermal annealing for an array of benchmark donor polymer systems.¹¹⁹ Addition

of small amounts of PCBM dimers in solution prior to deposition of active layer were similarly reported to enhance device thermal stabilities for a variety of polymer:fullerene BHJs.¹²⁰ The oligo(fullerene)s thus formed were reported to be identical in photo-physical properties with respect to PCBM. However, temperatures of 100 °C are sufficient to break the covalent bonds between the photo-transformed PCBM and the oligo(fullerene)s reverts back to their pristine state.¹¹⁹

A good part of the work in this thesis demonstrates the synthesis of novel poly(fullerene)s and their potential stabilizing effects in BHJ solar cells to this end. A recently discovered route called the Sterically controlled Azomethine ylide Cycloaddition Polymerization (SACAP) is explored to synthesize stable main-chain poly(fullerene)s. Chapter 5 details the synthesis and characterization of three novel poly(fullerene)s, and chapter 6 discusses their photovoltaic properties.



Figure 1.9: Coverpage of *Adv. Func. Mat.* 2013, 23, demonstrating photo-induced fullerene dimerization, by Edman et. al.¹²¹.

Chapter 2

Technique and Methods

The incoherent hopping of charge carriers and dispersive transport properties confers a high degree of complexity to the problem of probing charge transport in disordered organic systems. The fundamental transport properties, particularly mobility and recombination are subject to statistical distributions rather than single unique values and are influenced by a range of parameters such as temperature, electric field, morphology of film, purity and regio-regularity of the molecule used, etc. As mentioned in section 1.5, several experimental methods exist today to probe charge transport in organic systems, CELIV and TOF being of interest for the work described in this thesis.

2.1 Charge extraction by linearly increasing voltage (CELIV)

The technique of charge carrier extraction by linearly increasing voltage was introduced about fifteen years ago by Juška *et al.*¹²² to study charge transport in microcrystalline silicon at first and was soon applied in conjugated organic systems.¹²³ Conventionally, a linearly increasing voltage (triangular pulse) is applied to extract thermally generated carriers and the mobility is obtained from the peak extraction time of the corresponding transient. In organic semiconductors, where the thermally generated carriers are low, an input light pulse is typically employed to photo-generate the charges, wherein it is referred to as photo-CELIV.¹²⁴ The method was recognized to have overcome certain

limitations of the traditionally used time of flight (TOF) technique, discussed in the following section, including the possibility to study highly dispersive transients as commonly observed in organic disordered systems. It also allows the study of systems with high bulk conductivity and relatively short dielectric relaxation time (τ_o) in contrast to TOF. Additionally, photo-CELIV serves as one of the rare techniques to probe transport in samples with optimized fabrication conditions for real working devices in terms of architecture and active layer thickness.

A schematic illustration of the CELIV technique is given in Figure 2.1. In this method, a linearly increasing voltage is used to extract equilibrium/photo-generated charge carriers with density n and mobility μ from a film with a certain dielectric permittivity ϵ and thickness d . The whole device is represented as a capacitor with the film between two electrodes, with at least one of them being blocking. With the application of a voltage ramp, the resulting transient consists of an initial current step j_0 arising from the geometrical capacitance of the sample, given as

$$j_0 = \frac{\epsilon\epsilon_0 A}{d} \quad (1)$$

where A is the voltage rise speed (V/s) of the applied voltage pulse ($U(t) = At$)

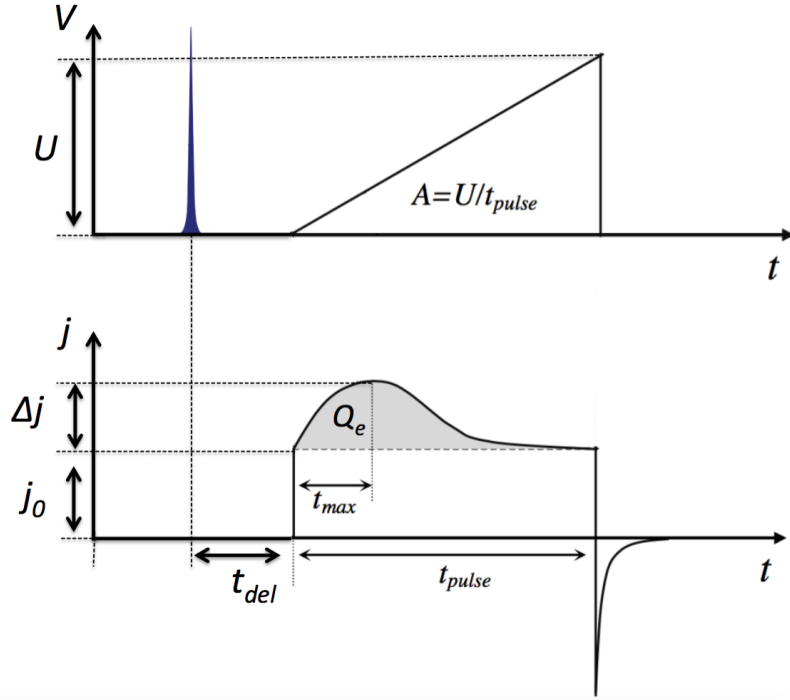


Figure 2.1: Depiction of the photo-CELIV technique – application of a ramp pulse in reverse bias after photo exciting the sample (above) results in the characteristic CELIV transient (below) from which mobility is calculated.

The rise speed of the current following j_0 is caused by the bulk conductivity of the sample. The time to reach the extraction current maximum t_{max} is used for the estimation of the drift mobility of equilibrium/photo-generated charge carriers.

Experimentally it is most convenient to make measurements when $\Delta j \cong j_0$ (*i.e.*, capacitive displacement current is comparable to conductivity current) so that $\tau_\sigma \cong t_r$, where t_r is the transit time of the packet of carriers. This condition may be achieved by choosing appropriate voltage ramp or adjusting input light intensity, in case of photo-CELIV. The bulk charge carrier mobility is then calculated as,

$$\mu = \frac{2d^2}{3At_{max}^2(1+0.36\Delta j/j_0)} \quad (2)$$

Equation (2) takes into account the numerically estimated correction factor for extraction length, assuming volume photogeneration.

Photo-exciting the sample prior to voltage sweep allows mobility estimation of photo-generated carriers, while measurements in dark provides drift mobility of equilibrium carriers. By varying the delay time between the application of input light and voltage pulse, one can obtain information about recombination on a microsecond time scale. The extraction of charge during the delay time can be prevented by the application of an offset voltage to configure flat band conditions or by the use of an electrical switch that holds the sample in open circuit during the delay time.

2.2 Time of Flight (TOF)

The time of flight technique was developed in early 1960s to study drift mobility in non-crystalline molecular solids and remains widely used to date.¹²⁵ In this technique, the transit time (t_r) of a two dimensional sheet of photogenerated charge carriers drifting through a sample of known thickness (d) is determined under a constant applied electric field ($E=U/d$). When the packet of charge carriers reaches the opposite contact the photocurrent drops forming a characteristic kink in the resulting current transient, corresponding to the transit time t_r .

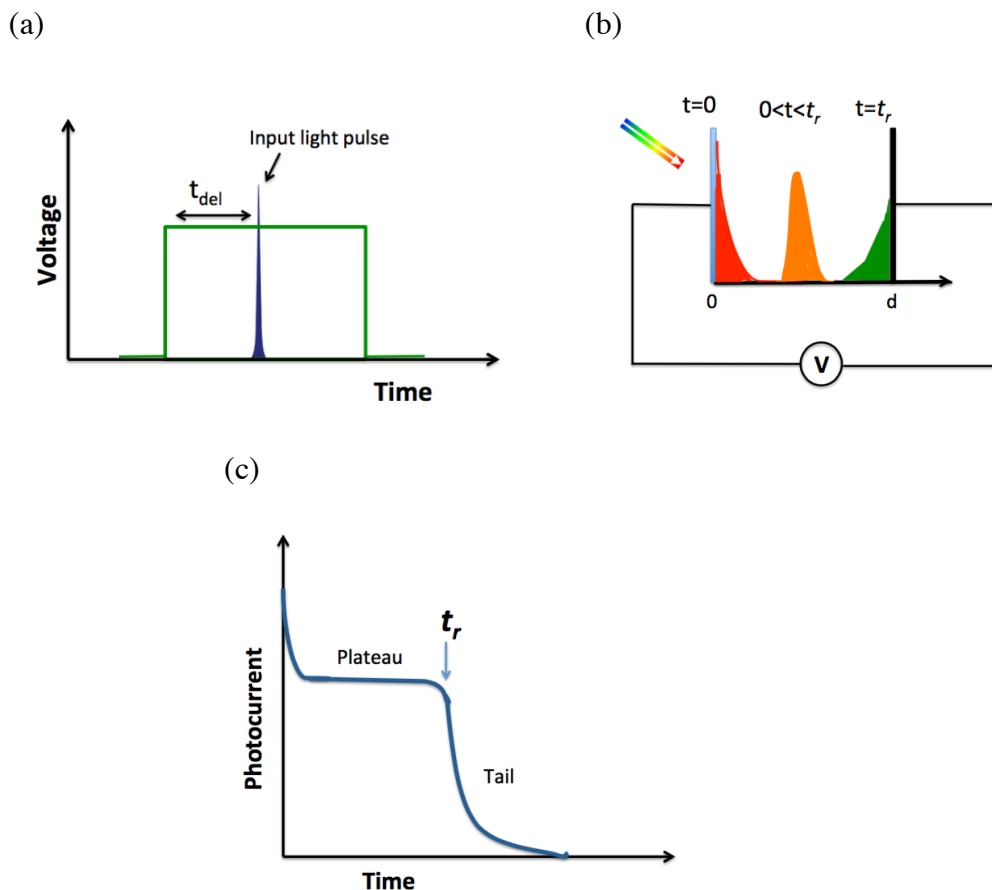


Figure 2.2 : (a) The sample under constant bias is illuminated by a short light pulse (b) charges photogenerated drift across the sample (c) shape of a typical TOF transient

Figure 2.2 depicts the technique and the shape of an ideal TOF transient. The sample is excited at time t_0 , after a certain delay time following the start of the applied voltage (square pulse). In the output signal, (figure 2.2 c) an initial current spike indicates the generation of both types of charge carriers. One species instantly recombines at the illuminated electrode, while the other starts moving at a constant velocity through the bulk of the sample. This uniform movement of the package results in a plateau region in the transient. When it reaches the opposite electrode, charge carriers from the packet start to recombine accompanied by a drop of the photocurrent, leading to a tail in the transient. Ideally, the transit time can be found from the time between this kink and the initial spike. However the dispersive transport in disordered systems like organics often makes it hard to observe a clear kink. Instead the initial spike and extraction blend together necessitating the transit time to be discerned from log-log plot of photocurrent *versus* time, from the intersection of an extrapolation of the plateau and a tangent to the tail. This method can be called current mode TOF since mobility is determined from the current signal.

The drift mobility is calculated as

$$\mu = \frac{d^2}{Ut_r} \quad (3)$$

Even though TOF is a technique widely used to estimate charge mobilities, the condition of surface photogeneration of charge carriers requires large film thicknesses with high optical densities ($OD > 10$) and hence its applicability is limited in optimized devices. However, volume photogeneration condition at high light intensities can be used in thin devices to obtain information on charge carrier recombination. A high intensity laser pump is used to photo-generate a reservoir of charge carriers inside the film such that the amount of charge in the reservoir is much larger than the charge stored on the sample electrodes (CU , C -sample capacitance) due to applied external voltage U . With increasing input light

intensity, the extractable charge Q_e also increases and eventually saturates when bimolecular recombination starts to dominate. As *Pivrikas et. al.*¹²⁶ explains, if the system exhibits fast Langevin type bimolecular recombination, the maximum extractable charge will not exceed CU , irrespective of the volume of photo-generated charge carriers. It is important to note that since the applied electric field is screened by both positive and negative charge carriers present inside, the electric field will be zero during carrier recombination and the diffusion controlled charge carrier recombination will dominate in the reservoir. The experimental bimolecular recombination coefficient (β) can be related to theoretically predicted Langevin type of recombination (β_L) as

$$\frac{\beta}{\beta_L} = \frac{CUt_r}{Q_e t_e} \quad (4)$$

where t_e is the extraction time.

The Langevin bimolecular recombination coefficient β_L can be calculated from the knowledge of mobility,

$$\beta_L = \frac{e(\mu_e + \mu_h)}{\epsilon\epsilon_0} \quad (5)$$

where e is the elementary charge, μ_e and μ_h are the electron and hole mobilities, respectively.

2.3 Experimental setup

A schematic of the experimental set up for photo-CELIV is shown in figure 2.3. A laser pulse is used to photogenerate charge carriers in the device. The laser is synchronized with the applied triangle pulse from the function generator, which controls the delay time as well. A standard oscilloscope can measure the output voltage. If desired, a resistor can be added to the circuit to change the load resistance for signal detection. The set up remains essentially the same for TOF, except the use of a square voltage pulse instead of triangular one.

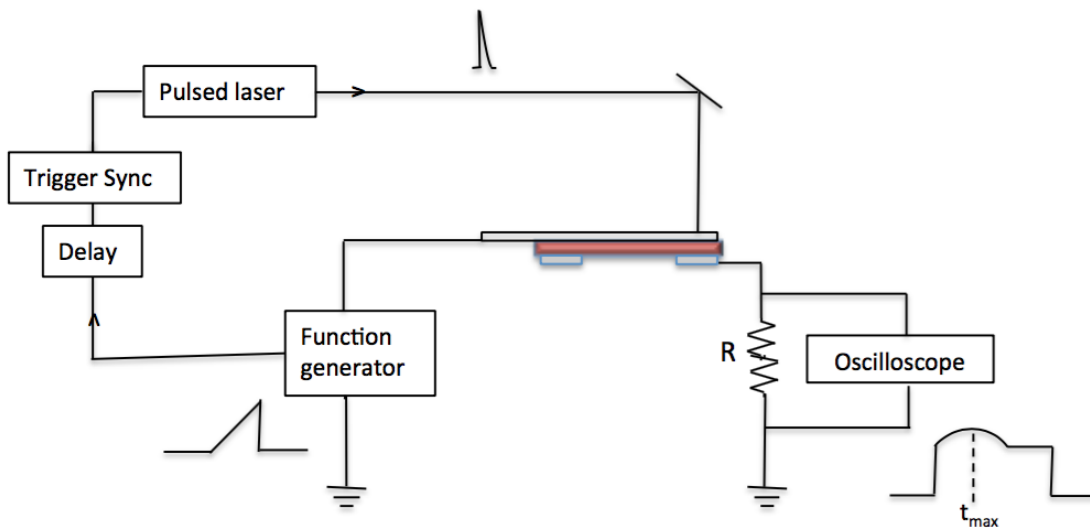
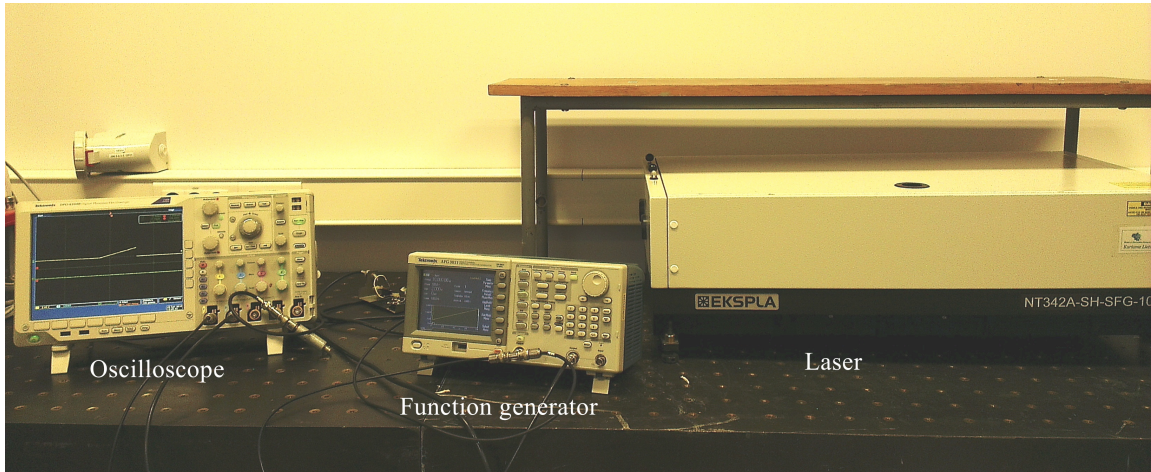


Figure 2.3 Image and schematic of CELIV experimental setup.

Integrating CELIV transients at different delay times (after subtracting the capacitance part) provides us with charge carrier density dynamics on a microsecond-millisecond time scale (figure 2.4). This provides us with knowledge of recombination within the studied system, along with complementary measurements.

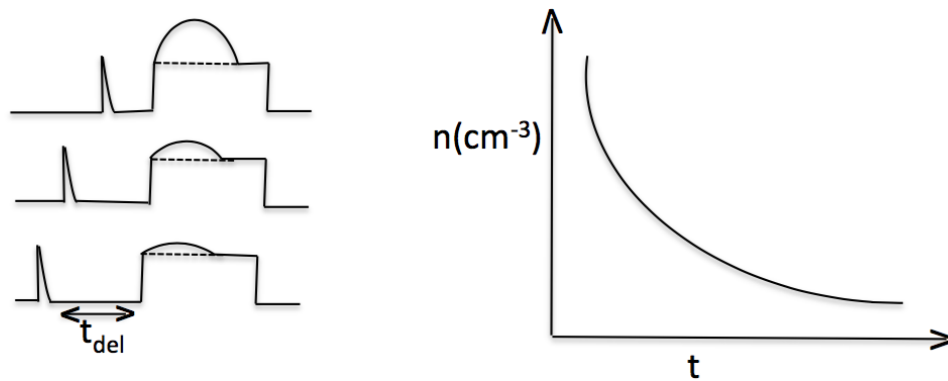


Figure 2.4 Schematic of obtaining charge density dynamics with respect to delay time

TOF measurements employ essentially the same set up except for the use of square pulse voltage.

Extraction current transient measurements detailed in this thesis were carried out using a 0.1 mJ, 4.3 ns pulsed wavelength-tunable laser (EKSPLA NT 340) as illumination source. Voltage pulses were applied from a function generator (Tektronix AFG 3011) and corresponding current transients were sampled and recorded using an oscilloscope (Tektronix DPO 4054B). Neutral density calibrated filters were used to vary the illumination intensity and the delay time was controlled by the function generator.

Chapter 3

Effects of Photo-Degradation on Charge Carrier Transport in P3HT:PCBM Solar Cells

In this chapter, photo-degradation in prototype P3HT:PCBM solar cells are studied with respect to charge carrier transport. Degradation of fully constructed solar cell devices is carried out in controlled conditions in the presence of oxygen. Evolution of charge transport parameters is probed by a combination of charge extraction techniques, photo-CELIV and TOF. While the reduction in photo-CELIV mobility is found to be within an order of magnitude over the course of degradation, an increased equilibrium (dark) carrier density and enhanced bimolecular recombination are inferred to be hindering the charge extraction process.

Parts of this chapter have been presented at 6th International Conference on Hybrid and Organic Photovoltaics (HOPV), Lausanne, Switzerland, May 2014 - 'Effects of photo-degradation in P3HT:PCBM solar cells studied by photo-CELIV' (poster); M. Stephen, S. Karuthedath, T. Sauermann, K. Genevičius, G. Juška, H.-J. Egelhaaf

*Parts of this chapter have been published in 'Degradation Effects on Charge Carrier Transport in P3HT:PCBM Solar Cells Studied by Photo-CELIV and TOF'; M. Stephen, S. Karuthedath, T. Sauermann, K. Genevičius, G. Juška, *Proc. of SPIE* 2014, 9184, 918424.*

The research leading to these results has received funding from the European Union Seventh Framework Program (FP7/2011) under grant agreement ESTABLIS no. 290022

3.1 Introduction

Among the many π -conjugated polymers developed for potential organic electronic applications, poly(3-hexylthiophene) (P3HT) is perhaps the most extensively studied. Despite the fact that new promising materials with improved properties exists today, P3HT remains of significant importance as a prototypical benchmark hole conductor material in OPVs. In this chapter the effect of photo-induced degradation in the presence of oxygen on bulk charge transport in inverted BHJ devices based on P3HT:PCBM active layer is studied. As discussed in chapter 1, the type of degradation dominating the device failure is governed by environmental conditions and device architecture, like, the choice of metal electrode.¹²⁷ Reese *et al.* showed that in devices with inverted structure, the degradation under illumination in dry air affects mainly the active layer, consisting of a reversible part, which is assigned to oxygen-induced doping and an irreversible part, which is due to photo-oxidation.¹²⁸ Seemann *et al.* went onto further detail that, for silver electrodes, the kinetics of degradation is clearly controlled by gas diffusion through or even around the top electrode into the photo-active layer.¹²⁹ While exposure of the cells to oxygen in the dark causes only small changes in the JV-curves, presence of oxygen and light at the same time rapidly deteriorates the device efficiency.¹³⁰ Illumination of devices in dry air (thus excluding any humidity effects) predominantly leads to a loss in short circuit current (J_{sc}), which decreases by more than 50% within 120 min of exposure. A partial recovery of J_{sc} and thus the efficiency was also observed on heat treatment of the degraded devices. The degradation of electrode being a possible contributor to these findings was excluded from the absence of an S-shape in the current-voltage characteristics of degraded samples.¹³¹ Both the reversible and the irreversible component of the observed degradation was thus attributed to be arising from the photo-active layer, since the increase in surface resistivity of PEDOT:PSS as a possible source was found to be negligible.¹²⁹ In

this chapter, the oxygen induced degradation of P3HT:PCBM solar cells under illumination is revisited. Detailed investigations including charge carrier mobility, charge carrier density and recombination measurements are performed to get an insight of the irreversible degradation mechanism due to oxygen in P3HT:PCBM solar cells.

3.2 Degrading the devices

BHJ devices based on P3HT:PCBM were fabricated in Belectric OPV GmbH, with indium doped tin oxide (ITO) cathode and silver (Ag) grids as anode, allowing them to be gas-diffusion open. Solutions of P3HT:PCBM (1 : 0.8) were prepared in water-free *o*-xylene (97%) by stirring at 80 °C overnight. The solar cells were made by applying a hole- blocking layer on an ITO–glass substrate, followed by the photo- active layer and the electron-blocking layer (EBL) with a transparent electrode. For the EBL, the commercially available HTL Solar 246 from Heraeus was used and the top electrode was realized by using the commercially available high conductive PEDOT PHCV6 (in isopropanol, 99.5% purity), combined with an evaporated silver grid electrode on top. All organic layers were applied by doctor blading, with a thickness of 250 nm for the resulting active layer.

Prior to degradation, devices were annealed at 140⁰C in glovebox for 5 minutes to gain a well-defined morphology for carrier transport often correlated with improved photovoltaic efficiency.¹³² All devices (non-encapsulated) were then exposed to AM 1.5 irradiation in dry synthetic air (80 % N₂, 20 % O₂, 0 % H₂O). The extent of degradation was monitored by UV/Vis-absorption spectroscopy and the optical density loss was categorized against the J_{sc} loss. To deconvolute the effect of possible electrode degradation, the degradation of partial devices (without top electrode) were compared with that of complete devices in similar conditions, and were found to follow similar kinetics.

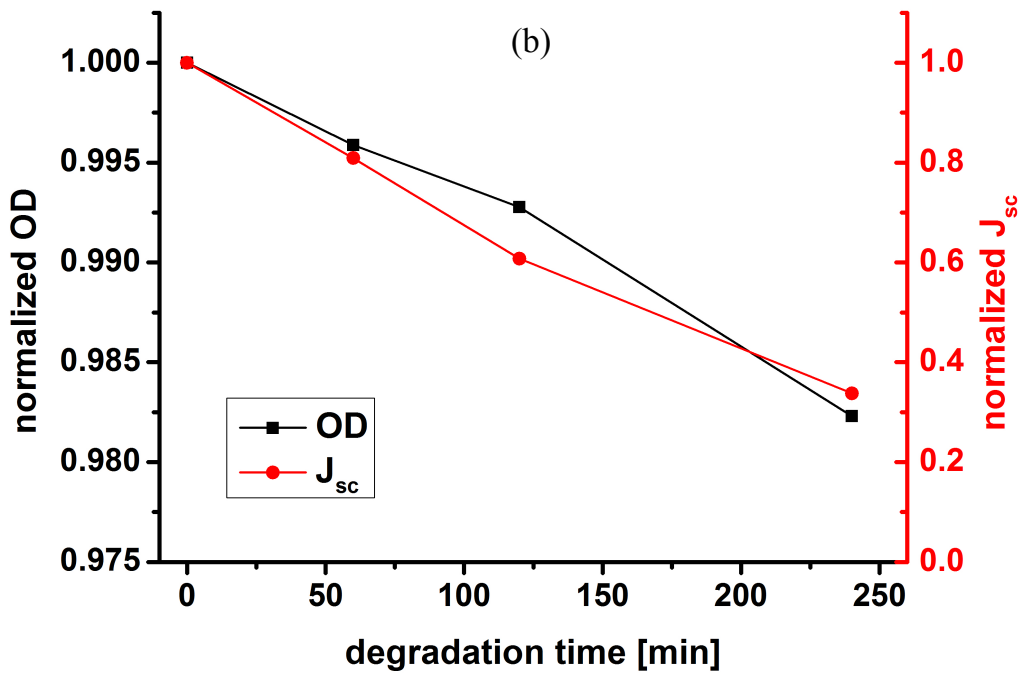
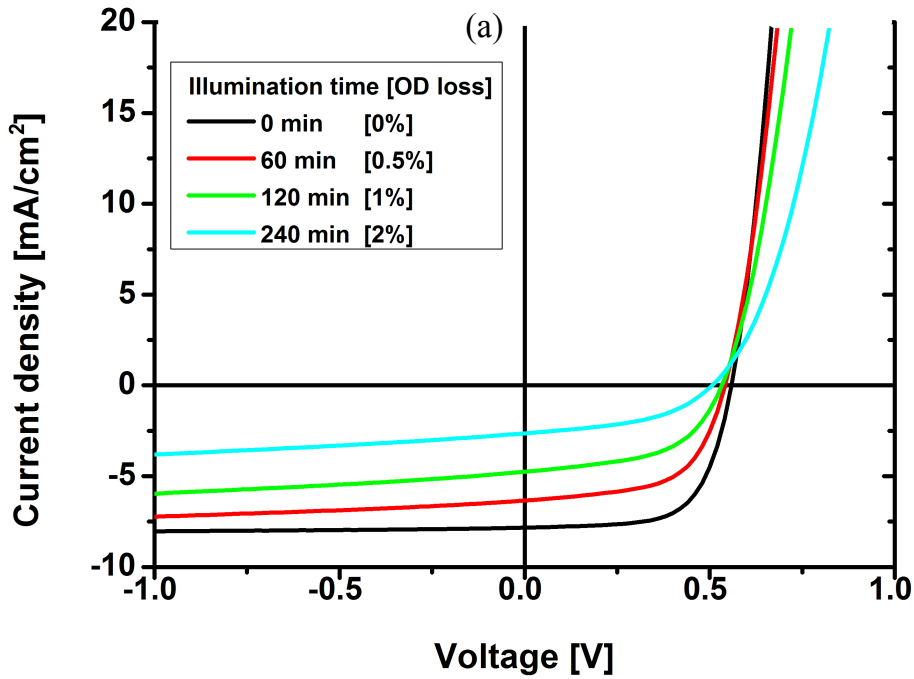


Figure 3.1: a) Current density - voltage characteristics of P3HT:PCBM solar cells and b) comparison of optical density loss with short circuit current loss; for different levels of photo-degradation.

Figure 3.1 shows the photovoltaic characteristics of the device at different stages of illumination. The short circuit current density irreversibly drops to $\sim 35\%$ within two hours of exposure, while the corresponding loss in OD is only 2%. Hence the huge loss in J_{sc} cannot be attributed to loss in absorption, in agreement with reports in literature.^{130,133} The loss in performance could then be associated with consequent steps during photovoltaic conversion, namely exciton dissociation, charge transport, extraction, etc., which we set about to investigate by photo-electrical methods in this work.

Throughout the experimental duration, samples were held in a cryostat (ICE) equipped with a temperature controller (Cryo-Con). All samples (pristine and degraded) were annealed under vacuum at 140°C for 5 minutes prior to measurements, in order to remove reversible degradation triggers. Photo-generation was achieved by exciting the sample at 532 nm, with experimental conditions detailed in section 2.3. For photo-CELIV measurements, the RC time was determined to be approximately 50 ns calculated from the geometrical capacitance and load resistance of 50Ω . Integral time of flight measurements were performed using the same set up but with a square pulse instead of triangular one for probing and a longer RC time of about $1 \mu\text{s}$.

3.3 Results and Discussion

3.3.1 Equilibrium carrier concentration

CELIV measurements in the dark reveal an increasing concentration of equilibrium carriers as degradation proceeds. Figure 3.2 shows the variation of extracted carriers in the dark with respect to degradation time, where the equilibrium carrier concentration is found to be increase four-fold within 4 h of illumination. Note that Figure 3.2(a) only provides a visual comparison and carrier density calculations were carried out from CELIV curves with optimized ramps

for each sample, keeping a constant input voltage, to ensure a complete extraction of charges without substantial injection.

The apparent increase in equilibrium carrier concentration is in good agreement with previous reports^{134,135,136} and is often attributed to the effect of doping of the active layer by oxygen. Hintz *et al.* identified the presence of at least two oxygen species with significantly different binding energies to P3HT. The reversibly bound species was attributed to physisorbed oxygen which probably forms a metastable charge transfer complex with the polymer upon photoexcitation of the latter. The irreversibly bound species was assigned to oxygen contained in photooxidation products.¹³⁵

The effect of such an increase in background concentration is expected to be detrimental in device performance owing to the screening of effective built-in field within the device. Such a trend in equilibrium carrier concentration with progressive degradation has also been observed in complementary transient absorption studies carried out by Karuthedath *et al.*¹³⁷ in samples prepared and degraded in same manner.

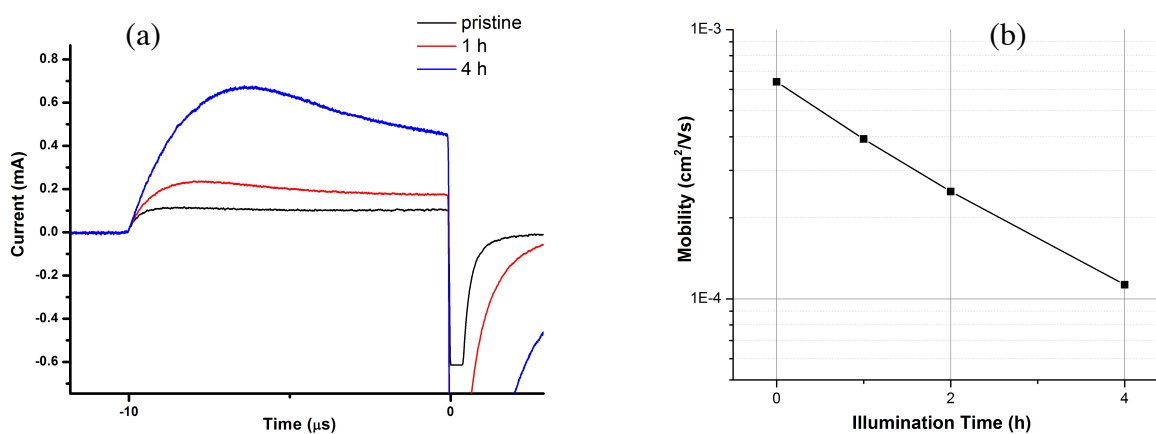


Figure 3.2 (a) Representative dark CELIV curves at identical experimental conditions of $R=50 \Omega$, $U=1V$ and ramp rates of $10^4 V/s$, recorded for samples with varying extends of degradation **(b)** Equilibrium carrier densities calculated from dark CELIV transients at $1V$ applied voltage and optimized ramp rates.

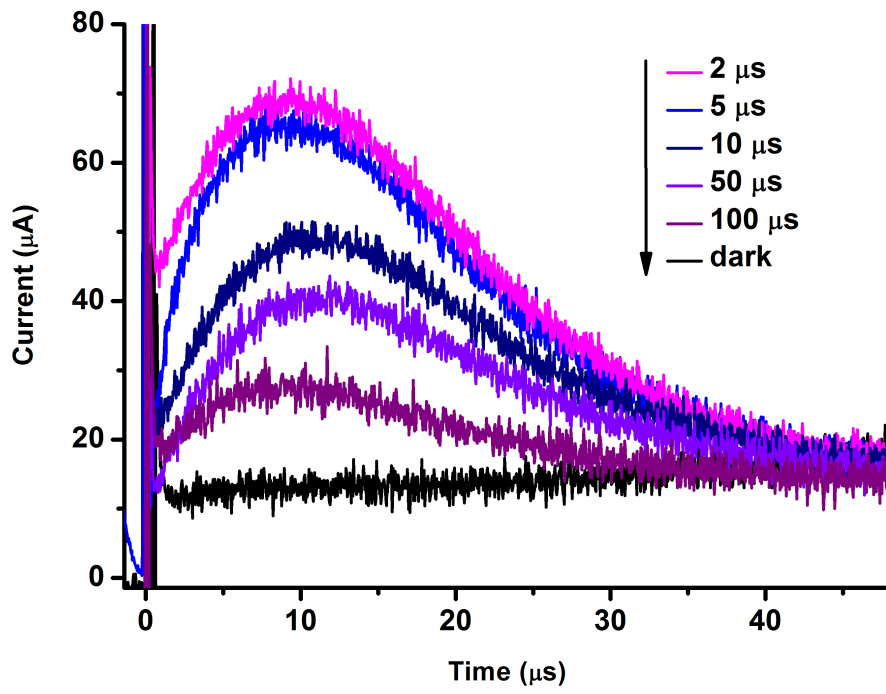
3.3.2 Charge carrier mobility

Photo-CELIV has been employed to estimate the charge carrier mobility at different times of degradation. The calculated values (Figure 3.3 b) correspond to a delay time of 5 μs with a ramp of 10^4 V/s and an applied offset bias of ~ 0.5 V for all the samples. An electrical set-up is used to compensate built in voltage before the application of triangle pulse and hence to avoid carrier extraction during the delay time. The photo-CELIV transients were recorded for a range of delay times from 2-100 μs for each sample and the mobility is observed to be more or less constant within this time range. Figure 3.3a shows the transients with respect to delay time for pristine sample. The photo-CELIV mobility could be argued to be the average mobility of both charge carriers, however, the characteristic t_{max} is said to be predominantly influenced by faster carrier, which becomes significant when the carrier mobilities extremely differ from each other.¹³⁸

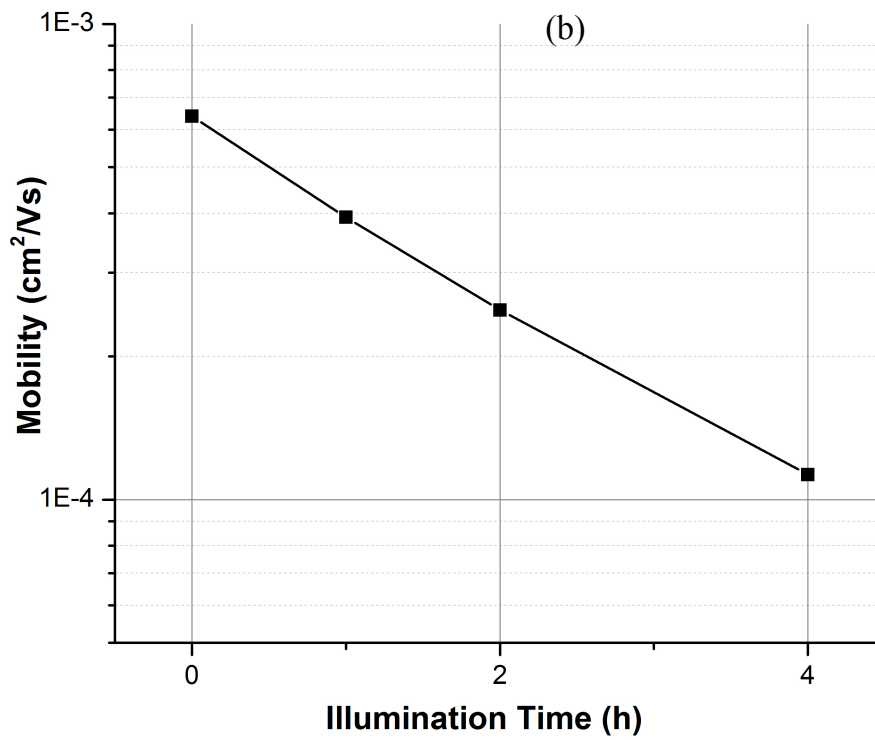
A reduction of the blend mobility of the order of four times is observed over the degradation time. We obtain a value of 6.4×10^{-4} cm^2/Vs for mobility of pristine sample, which reduces to 1.1×10^{-4} cm^2/Vs after 4 h of illumination.

The photo-CELIV transients also provide with relevant information regarding trapping, as observed in the overlay of transients shown in Figure 3.3 c. Note that the transients included here are not obtained from same intensity light pulse since we had to use slightly higher intensity for more degraded ones to fulfill the low conductivity condition. We cannot directly relate this to photo-generation because of the observed variation of equilibrium carrier concentration across samples. Another significant difference between the curves is the distinct tailing for degraded samples. Transients corresponding to longer degradation times fail to achieve complete extraction within the applied pulse duration, indicating the presence of traps. The trapping effect is also evident from the peaks getting broader, owing to a more dispersive transport.

(a)



(b)



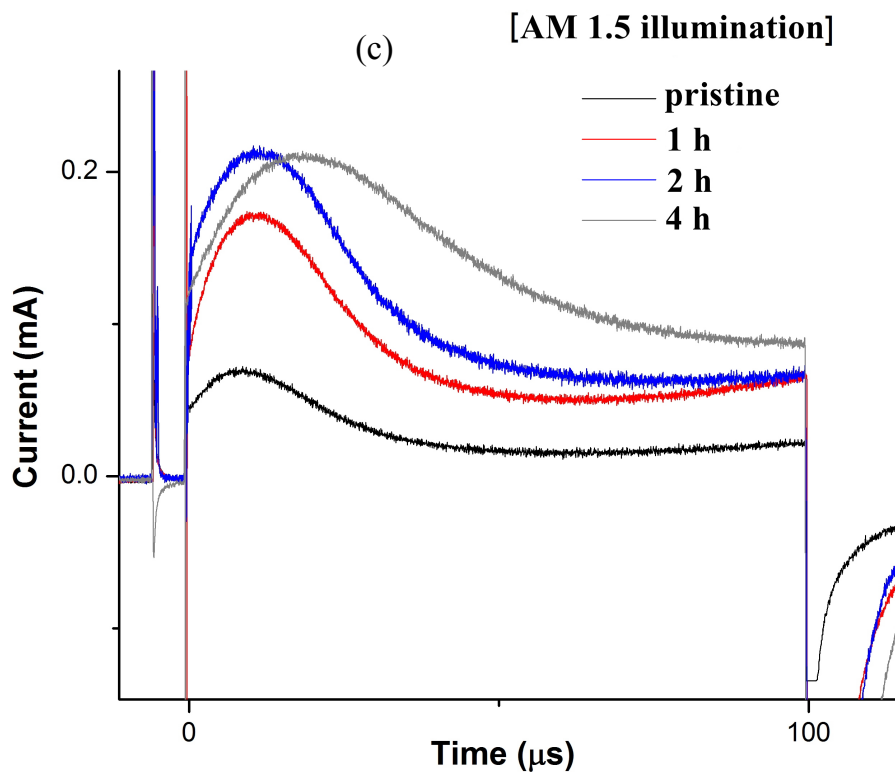


Figure 3.3: a) Representative photo-CELIV transients recorded for a range of delay times for the pristine sample at constant voltage and ramp rate b) Trend of mobility with respect to illumination time at $5 \mu\text{s}$ delay for all samples, and c) overlay of photo-CELIV transients at 1V applied voltage and 10^4V/s ramp rate for samples with varying extents of degradation

Time of flight measurements for determination of mobility were limited by the thickness of the samples and clear transit times were not obtained due to RC effects.

3.3.3 Charge recombination studies

To study recombination, firstly charge carriers density dynamics on a micro-second time scale was obtained from photo-CELIV measurements with long pulse times and use of an electrical key to avoid any extraction during delay time. This ensures that the drop in extracted charge density with increasing delay times is purely due to recombination of charges held within the device. Figure 3.4 a shows the transients recorded for delay times ranging from 100 ns to 1 ms with a ramp of 5×10^3 V/s, for the pristine sample. Figure 3.4 b summarizes the results obtained for extracted charge with respect to delay time at different degradation points. The plot suggests a slower recombination in more degraded samples and indicates that the extracted charges tend to be present inside the device for longer times as degradation proceeds. The recombination being slowed down could be an effect of reduction of mobility and also a manifestation of the deep trapping effect. With progressive degradation, more charges tend to be stuck in the device even after hundreds of microseconds. Note that recombination at this time scale could not be expected to be strictly of one kind throughout since the type of recombination is also dependent on carrier concentration and would be changing from bimolecular during short delay times when there exists a significantly larger photo-generated carrier concentration relative to the trapped ones below the mobility edge, to pseudo-monomolecular at longer times when most of the mobile carriers are extracted or have recombined. Thus the increase in number of traps can also have an influence on dynamics of interplay between these two mechanisms and time scales at which the latter one starts to predominate, further complicating any direct conclusions.

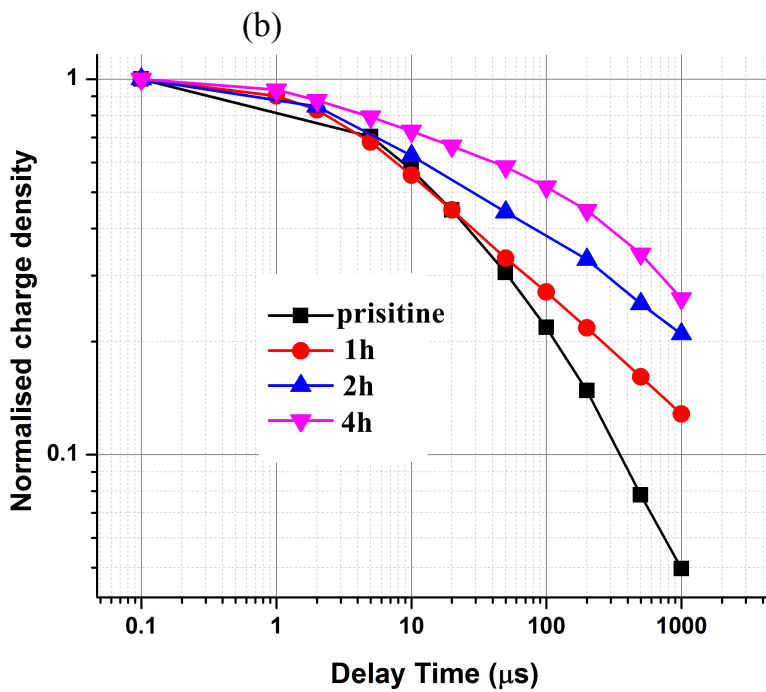
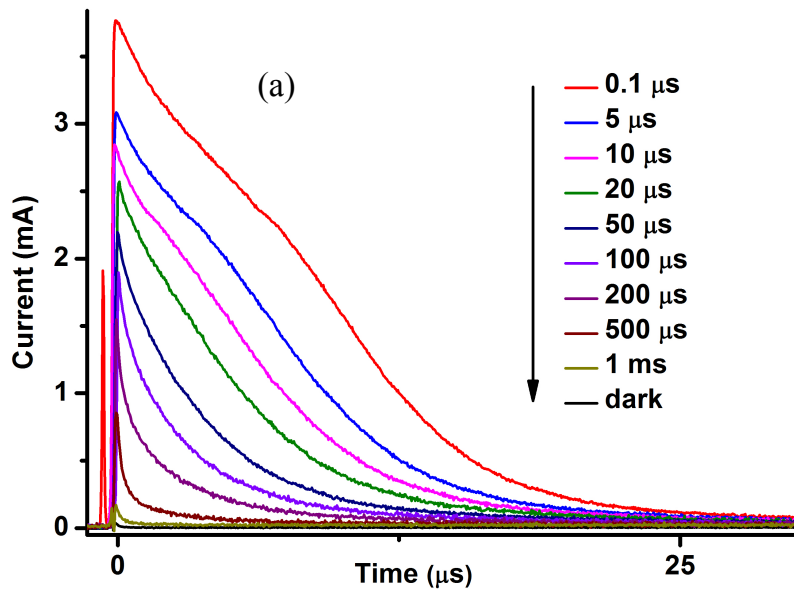


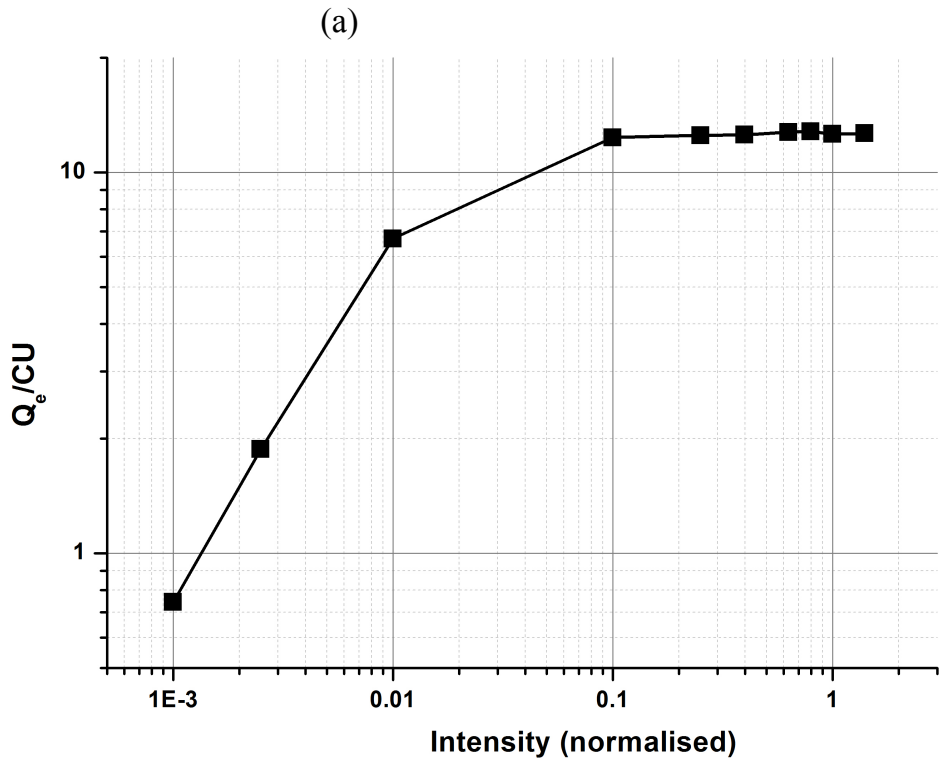
Figure 3.4: a) Overlay of photo-CELIV transients recorded over a range of delay times, without any applied offset, for the pristine sample with 1V pulse and a ramp rate of 5×10^3 V/s and b) overlay of calculated extracted charge density at each delay time across samples with varying extents of degradation.

Time of flight measurements at high light intensities and high resistances were carried out to examine the trend of bimolecular recombination and the Langevin reduction factor (β/β_L) with longer times of degradation. TOF transients are recorded at varying light intensities until they saturate, creating a reservoir of photo-generated charges within the sample. Figure 3.5 a shows the calculated extracted charge normalized to charge stored on contacts with respect to input light intensity, which initially increases linearly and then saturates at higher light intensities. The transients were recorded at 2V with 1 K Ω resistance. At high intensities the reservoir of charges formed inside the film screens the effective electric field and forms a space charge region. The shape of transient corresponding to reservoir extraction and its decay gives a quick view of whether the recombination in the test system follows Langevin mechanism. Figure 3.5 b shows an overlay of saturated transients for samples under study. The saturated transient for the pristine sample clearly exhibits a plateau region before the main current decay which is a signature of reduced Langevin recombination, as expected in regio-regular P3HT-PCBM blends. From figure 3.5 a, we see that the extracted charge reaches well above the capacitive charge, which further confirms this behavior. From this plot it is apparent that the extracted charge from the reservoir significantly reduces with progressive degradation and the decay becomes increasingly featureless. With 4h of illumination, the characteristic plateau almost disappears and tailing of the transient is also evident, resulting from increased number of traps, in agreement with photo-CELIV measurements as previously discussed. The extracted charge is quantified by integrating the transient, given as Q_e and extraction time, obtained by the difference between $t_{1/2}$ of transients corresponding to high and low intensities, as shown in Figure 3.5 c is given by t_e .

These results are summarized in Table 1.

Illumination (h)	Q_e/CU	t_e (μ s)	β_L ($\times 10^{-10}$ cm ³ /s)	β ($\times 10^{-12}$ cm ³ /s)	β/β_L
0	17.5	12.4	3.9	0.84	0.002
1	14.6	10.5	2.3	1.3	0.005
2	13.8	9.96	0.75	2.3	0.031
4	14.8	8.13	0.68	1.6	0.024

Table 1 : Parameters obtained from high light intensity TOF measurements.



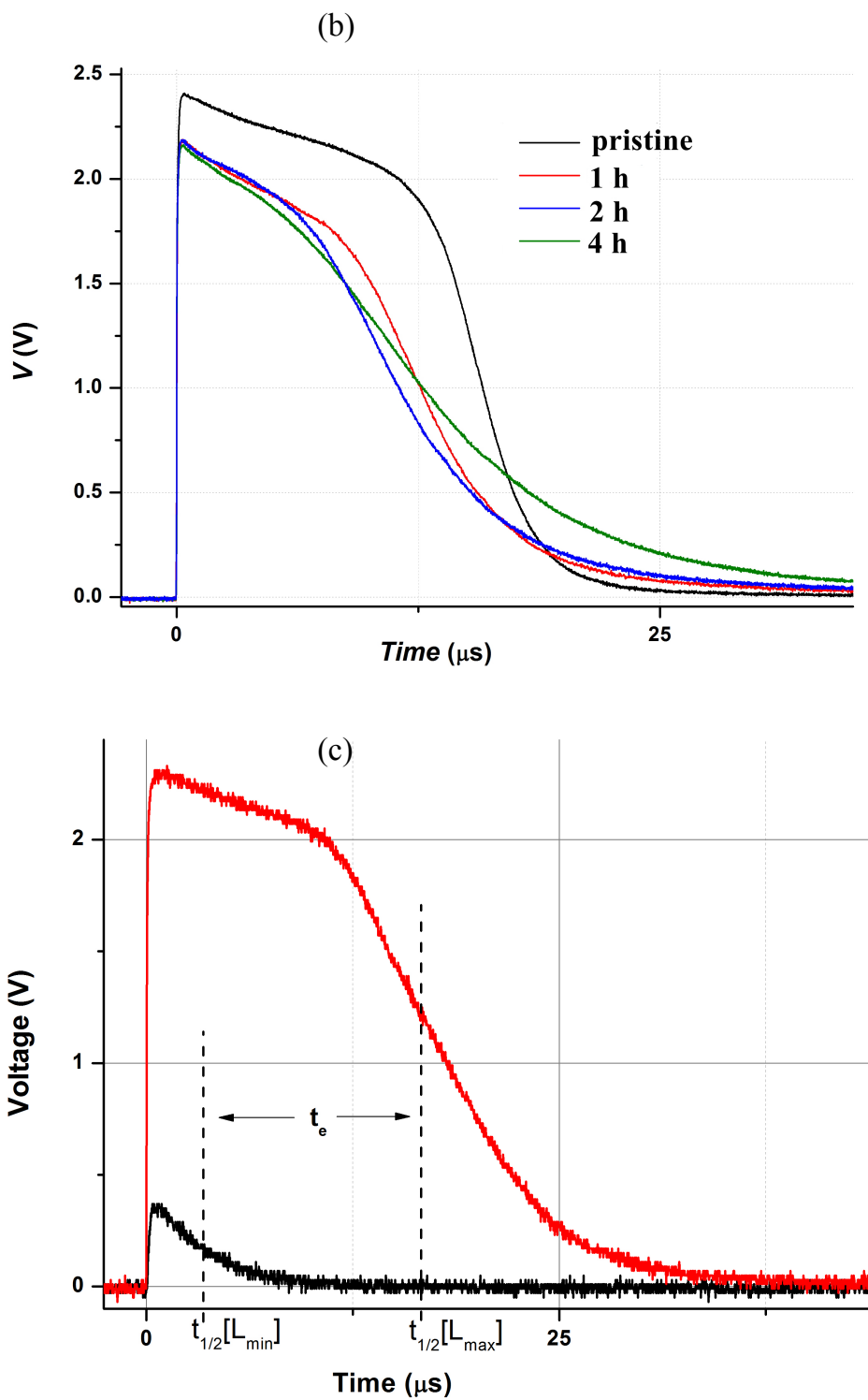


Figure 3.5: a) Extracted charge normalized to charge stored on contacts with respect to intensity for pristine sample, b) Overlay of saturated integral TOF transients for different samples, c) Representative integral TOF transients demonstrating extraction time t_e for pristine P3HT:PCBM

Since bimolecular recombination depends on mobility, comparison of the Langevin reduction factor β/β_L stands more rational than comparison of obtained bimolecular recombination coefficients (β) as such. Applying equation 4 gives a value of 0.002 for the reduction factor in case of pristine sample, in other words an observed recombination of 500 times reduced than theoretically predicted one. Such reduction in bimolecular recombination in annealed blends of P3HT (regio-regular) : PCBM is known from literature.¹³⁹ As the samples are degraded the reduction factor increases and reaches 0.02 for 2% O.D loss, which corresponds to a bimolecular recombination only 50 times reduced with respect to Langevin. These measurements imply that during the initial fast recombination phase when the photo-generated carrier density is sufficiently high and the recombination is predominantly bimolecular, the kinetics of recombination is enhanced as degradation proceeds.

3.4 Conclusions

In summary, an increase in the number of trapped charge carriers were evident from the extraction current transients of P3HT:PCBM solar cells with progressive degradation. The average mobility of the blend, as obtained from photo-CELIV was found to be gradually reducing with increase in degradation time. The increase in Langevin reduction factor with degradation, determined from integral TOF measurements at high light intensities, hints at the destruction of ideal nanomorphology reported for pristine P3HT:PCBM blends.

Chapter 4

Photodegradation in Encapsulated BDT-DPP based Solar Cells

In this chapter, the photo-degradation of a series of four benzodithiophene (BDT) – diketopyrrolopyrrole (DPP) based polymers with different side-chains is studied with respect to charge carrier transport. The devices were glass-encapsulated so as to eliminate additional degradation triggers like oxygen and water. Analysis of extraction current transients indicated the progressive formation of trap states as being the most predominant effect influencing the process of charge extraction. Probing the bulk charge transport by the techniques detailed herein, solely, was found to be insufficient to distinguish between the possible variations in photo-stability induced by a particular side-chain.

Parts of this chapter have been presented at European training school and conference on organic photovoltaic stability (ESOS), June 2015, Cargèse, Corsica, France – ‘Effect of degradation on bulk charge carrier transport in BDT-DPP based polymer solar cells’ (talk); M Stephen, G. E. Morse, G. Juška, K. Genevičius

*Parts of this chapter have been published in ‘The Effect of Polymer Solar Cell Degradation on Charge Carrier Dynamics in Benzodithiophene-Diketopyrrolopyrrole Polymers’; M. Stephen, G. E. Morse, N. Blouin, O. Lozman, K. Genevičius, G. Juška, **Materials Chemistry and Physics** 2016, 10.1016/j.matchemphys.2016.09.005.*

The research leading to these results has received funding from the European Union Seventh Framework Program (FP7/2011) under grant agreement ESTABLIS no. 290022

4.1 Introduction

Many classes of new polymers have been designed, synthesized, characterized and incorporated into photovoltaic devices owing to the extensive research efforts in improving the efficiency of these devices.^{140,141} One can depict these polymers as a combination of rigid π - conjugated backbone substituted by side-chain groups. The presence of side-chains is mandatory to ensure sufficient solubility in required solvents, a much-desired trait for solution processibility of active layer. Side-chains are also found to influence material properties like position of energy levels and packing of the macromolecular chains.^{142,143} Current state of the art polymer semi-conductors based on low band gap polymers are decorated with a selection of linear and/or branched solubilizing side-chains. So far the impact of these side-chains on the polymer order, phase separation and electronic properties has been investigated only in benchmark materials and few studies report on their impact on photostability. While in some cases the presence of side-chains itself is reported to trigger photo-degradation,^{144 145} optimizing the substituent chains/functional groups allows for optimum and stable photovoltaic performances. For example, the hexyl side-chain of P3HT is found to offer the best compromise between solubility, morphology and favorable steric interactions of side-chains (in case of regioregular P3HT) when compared to other alkyl side-chains.¹⁴⁶ Xia *et. al.* reported enhanced photo-stability of co-polymers based on indenofluorene unit by replacing the octyl side-chain with a phenyl ring.¹⁴⁷ More recently, insertion of ester or alcohol moieties on the side-chains was reported to be beneficial for improved thermal stability of the prototype low band gap polymer PCPDTBT based solar cells.¹⁴⁸

Herein we use charge extraction measurements to study the effect of photo-degradation in solar cell devices based on a series of benzodithiophene (BDT) – diketopyrrolopyrrole (DPP) based polymers, with varying side-chains. The studies

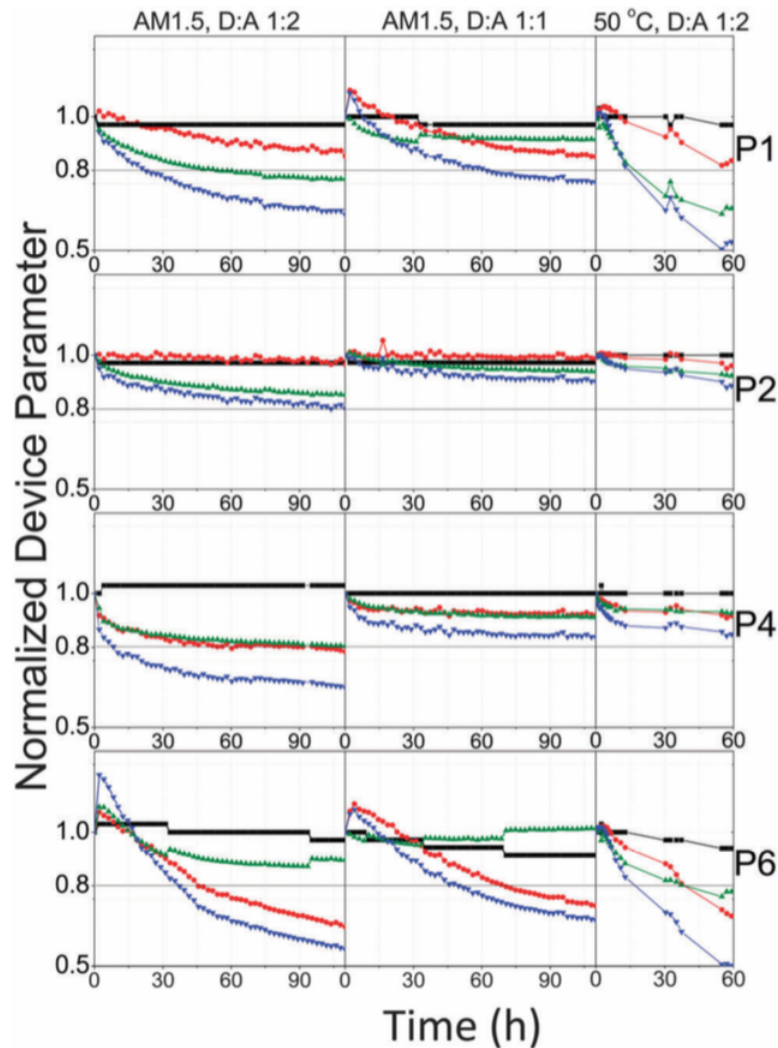


Figure 4.2. Evolution of J_{sc} (\blacklozenge), V_{oc} (\blacksquare), FF (\blacktriangle) and PCE (\blacktriangledown) upon AM 1.5 illumination in solar cell devices based on P1-P6/PCBM bulk-heterojunction active layer, taken from reference 10.

Excerpts from previously reported data is provided to convey the objective of work:

Optimized photovoltaic devices based on P1-P6/PCBM blends as active layer yields efficiencies of 5.1%, 4.4%, 2.7% and 2.9% for P1, P2, P4 and P6 respectively. On exposing the glass-encapsulated devices to continuous AM 1.5 illumination, devices based on P2 proved to be the most stable, retaining 80% of its initial PCE after 110 h of illumination, known as its T_{80} . The T_{80} for P6 (37 h),

P1 (23 h) and P4 (10 h) were significantly shorter (figure 4.2). Thus the observed photo-stability of devices were in the order P2>P6>P1>P4.

From UV-visible spectroscopy and AFM/XRD data, PCBM dimerization and ripening of blend morphology were hypothesized to be driving the photo-degradation in thin films of P1-P6/PCBM blends. Ripening refers to the nanomorphological evolution of the active layer blend as a consequence of PCBM diffusion, which is a purely thermal process. The diffusion strongly depends on the polymer matrix, in other words, PCBM diffusion is favored if the polymer chains are relatively mobile at the considered temperature.

The rather high stability of P2 was considered to be originating from densely packed polymer aggregates attributed to the highly ordered linear side-chains. This conforms to the co-relation of ordered molecular packing and resulting dense films to an improved photo-oxidative stability reported in literature.¹⁵⁰ Additionally, the relatively low solubility of the polymer indicated lower PCBM miscibility, resulting in a reduced PCBM diffusion rate within the film.

This work clearly showed that subtle changes in the side-chain could significantly affect the morphological evolution of the blend and consequently the device stability in well-encapsulated devices. Our work herein is of the interest of gaining insight into possible effects on charge carrier mobility and dynamics across the polymer series during the process of degradation. The technique of photo-CELIV is particularly advantageous to this end since it can be employed in fully constructed and operational OPV devices, allowing these measurements to be made during degradation analysis. To elucidate the evolution of charge transport parameters, photo-generated charge carriers were extracted and analysed by photo-CELIV and high light intensity time of flight (TOF) techniques through the course of degradation. Measurements were carried out on glass-encapsulated

devices, which were exposed to AM 1.5 illumination for as long as 80 h, data points being collected every 20 h.

4.2 Experimental

Device fabrication

Inverted structure devices were fabricated on $13 \text{ } \Omega/\text{cm}^2$ photo-lithography patterned ITO. The zinc oxide transport layer was formed by spin-coating a solution of zinc acetate dihydrate in dimethylsulphoxide at 160 g/L at 4000 rpm for 10 seconds followed by a 5 minutes thermal anneal at 300°C . The active layer was deposited by blade coating. On top of the active layer a uniform layer of PEDOT:PSS was spin-coated at 1100 rpm for 130 s. The silver top electrode was applied by vacuum deposition at 2×10^{-6} mbar at $1\text{-}5 \text{ } \text{Å}/\text{s}$. The devices were subsequently encapsulated with a top glass cover slide containing a $120 \text{ } \mu\text{m}$ cavity in the center of the slide. The outer edge of the cover slide was sealed using UV curing epoxy. The devices were exposed to AM 1.5 from a Newport 94082A Solar Simulator and data was collected using a sourcemeter (Keithley 2400) connected through a switch system (Keithley 2750).

Measurements

Experimental setup for photo-CELIV and TOF measurements were same as detailed in section 2.3, the laser was tuned at 700 nm to better match the absorption of the polymers under study. Due to the large RC time constant (small thickness and large contact area), TOF measurements were limited to volume photo generation regime under high light intensities.

4.3 Results and Discussion

Dark CELIV transients are found to be increasing in amplitude in all the devices as degradation proceeds (figure 4.3). A clear distinction between capacitive part and conductive part is not apparent since the contacts are not completely blocking, as usually observed in inverted structured devices. This could be due to the effect of charge blocking layers being not strictly selective to the transport of one type of charge carrier.

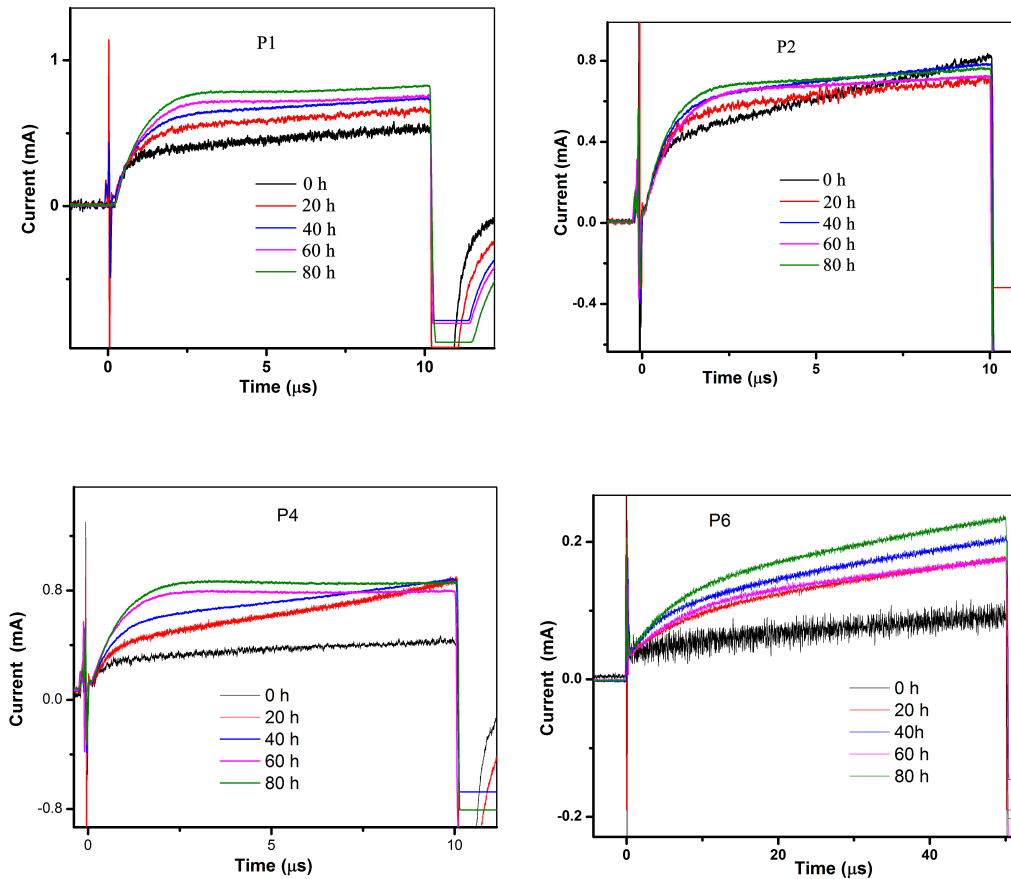
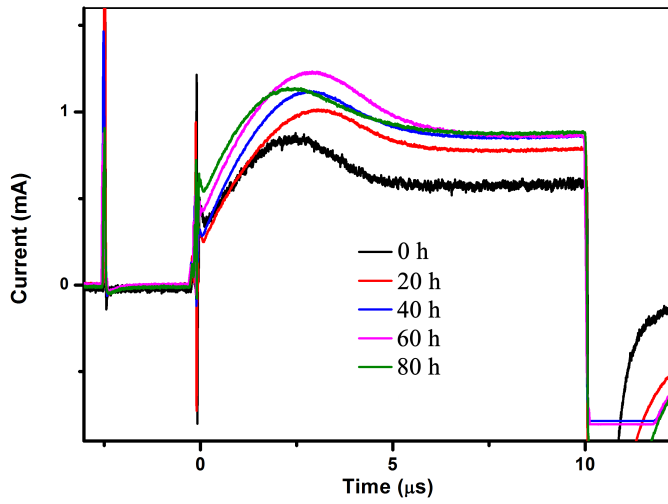


Figure 4.3. Dark CELIV transients at various points in degradation for devices based on polymers P1-P6.

As discussed in chapter 3, unintentional doping upon degradation is reported in literature and is thought to serve detrimental to the photovoltaic performance by potentially redistributing the built-in field within the device.^{151,152} Since the process of degradation in this study is oxygen free, as detailed in reference 149, the doping of the active layer being oxygen induced does not suffice a justifiable explanation. A change in dielectric constant of the photo-active layer upon degradation cannot be ruled out since the trapped carriers (as will be discussed in following sessions) can potentially induce polarization effects within the medium. The evolution of nanomorphology into large phase separated domains could result in isolated regions with distinct crystallinity and conductivity. Change in dielectric permittivity and consequently the capacitive current j_0 stands as a reasonable proposition in this scenario.

The mobility values obtained from photo-CELIV transients for the series of polymers at various illumination times can be seen in figure 4.4b. The mobility values of pristine devices are an order of magnitude lower than reported hole mobilities of neat polymers from field effect transistor measurements, except P4, which exhibits similar mobilities in both measurements. A difference in transistor and photo-CELIV mobilities can result from the basic difference in configuration of samples used for these measurements and consequently the direction of transport being probed (vertical/horizontal to substrate). At the moment a reason for the rather high photo-CELIV mobility particularly in case of P4 is not obvious. It has been acknowledged that the CELIV peak is influenced by both carriers and hence the average mobility is obtained. However, in cases where the electron and hole mobilities are highly unbalanced, it could be argued that the obtained mobility is predominantly of the faster carrier.¹⁵³ Considering this gain in mobility not being reflected in the short circuit current density of P4 based devices, it is probable that the CELIV peak is predominated by electron transport in this case.

(a)



(b)

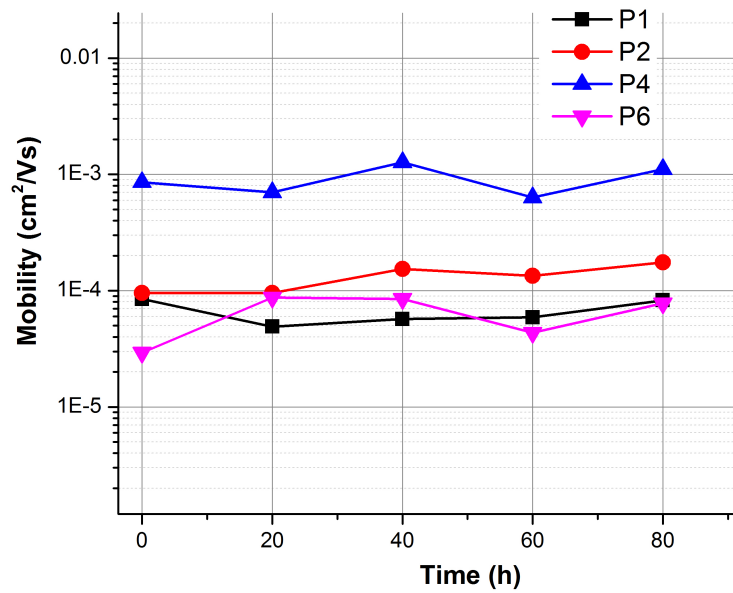


Figure 4.4 (a) Overlay of representative photo-CELIV transients at 2 μs delay time at different points in degradation for P1; (b) Photo-CELIV mobilities obtained for devices based on polymers P1-P6 at different points in degradation.

Through the course of degradation, the photo-CELIV mobilities of all studied systems are found to remain unchanged, within the experimental error. Clarke *et. al.* reported a similar trend in photo-CELIV mobilities during the photo-degradation of silole-based solar cells.¹⁵⁴ Evidently, the amplitude of the transients at longer times increases in degraded samples, which might result from trapped charge carriers being extracted, as the higher voltages at longer times promote emission from traps.

While the tailing of transients provide clear evidence for increasing number of trapped carriers, this technique does not afford information about the energy of additional levels created or time-scales of trapping and de-trapping. However, the fact that mobility remains more or less constant, together with the appearance of tailing of transients, suggests that the release time for trapped carriers are longer than transit time, indicative of deep trapping. The representative t_{max} of the transients being not affected by trapped carriers is even more probable if it is the slower carriers that are primarily trapped.

Micro-second time scale dynamics of charge carrier density at each point of degradation was obtained by varying the delay time between illumination and voltage pulse (Figure 4.5) in photo-CELIV. An electrical key is used to keep the device in open circuit during the delay time, ensuring no extraction of charges and hence the charges lost during delay time are solely due to recombination.

The plot reveals the recombination rate being considerably slower than bimolecular (slope <1), even in pristine case, for the series of polymers. The recombination dynamics in this time scale (μ s-ms) appears to remain unaltered during degradation for P1 and P4, while P2 and P6 shows slightly slower recombination once degraded, as discerned from the reduced slope of the plot for degraded samples. Large-scale phase separation of donor and acceptor domains

within the bulk heterojunction is expected to reduce the recombination rate by the reduced probability of charge carriers to meet.

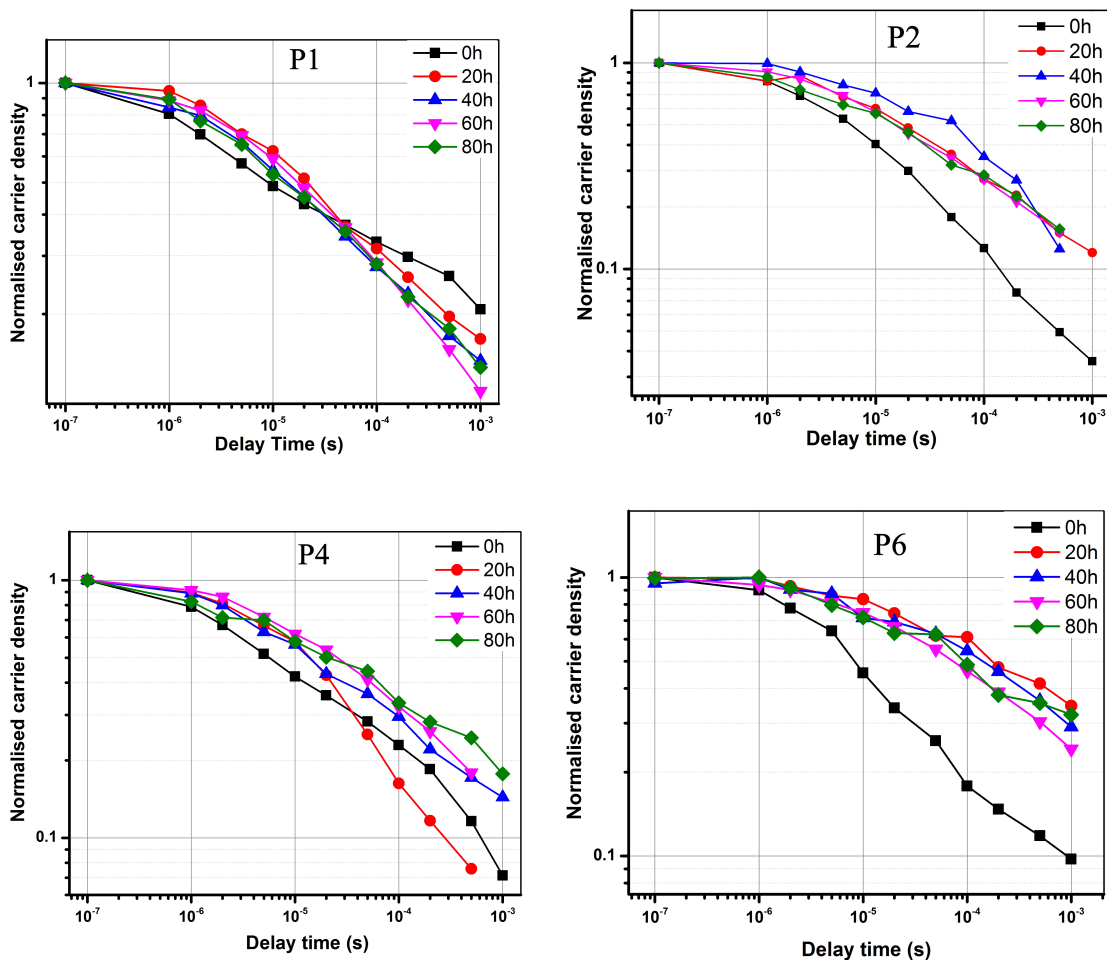
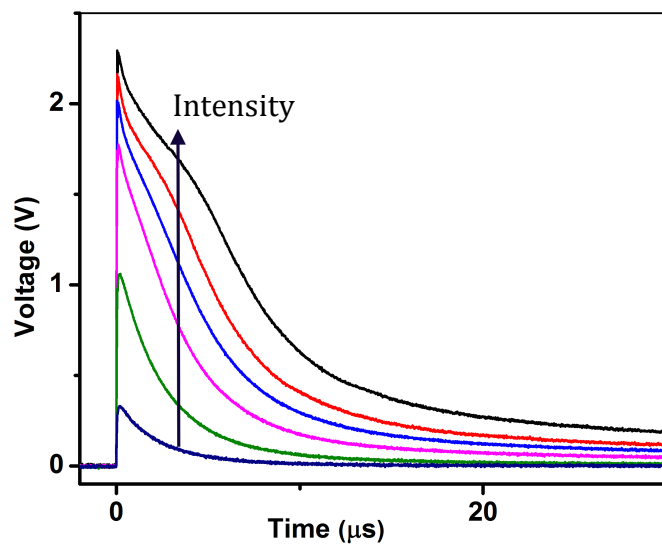


Figure 4.5. Charge carrier density dynamics with respect to delay time obtained from photo-CELIV for devices based on polymers P1-P6 at different points of degradation.

Volume photogeneration TOF studies ($RC \gg t_r$) have been carried out at illumination intensities high enough to saturate the observed transients, thereby creating a reservoir of photo-generated charges within the film. The extraction time t_e is obtained from difference between $t_{1/2}$ of transients corresponding to highest (saturated) and low (amount of photogenerated charge is much lesser than CU) intensities, as detailed in Chapter 3.

(a)



(b)

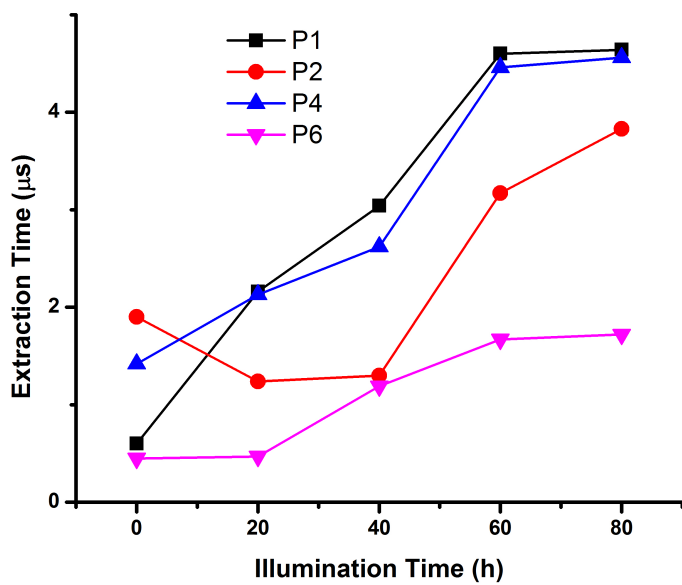


Figure 4.6. (a) Representative TOF transients for pristine EP1, with increasing input light intensity until the transient saturates; (b) Extraction times obtained from TOF for devices based on polymers P1-P6 at different points of degradation.

The high light intensity TOF transients (figure 4.6) reveal increasing extraction time with progressive degradation in all the studied polymers in the series. This supports the observation of longer-lived charges in degraded samples in photo-CELIV. The reservoir of charges created would be expected to fill in the trap states and hence the decay of charges should be predominantly resulting from bimolecular recombination. The fact that the extracted charge density as well as the extraction time increases with progressive degradation could be directly related to the probability of meeting of the type of carriers. This implies the increasing phase separation between the domains of the bulk heterojunction, resulting in purer domains of each phase. The observed tailing of TOF transients further suggests that more charges are trapped within the device as degradation proceeds.

4.4 Conclusion

The evolution of charge transport properties of solar cell devices based on a series of poly(benzodithiophen-*alt*-diketopyrrolopyrrole) derivatives with different side-chains have been analysed using current extraction techniques. Based on the obtained results, we conclude that increase in trapped carriers play the most dominant role in determining charge transport properties of the blend on a macroscopic time scale. Since our devices were glass encapsulated, this behaviour is considered to be arising from inherent properties of the blend rather than external triggers from water or oxygen ingress. However, complementary studies are required to single out the potential effects of side-chain variation in terms of charge transport and photo-stability. More time-resolved measurements as well as methods that can quantify the number of trap states are considered desirable to this end.

The present study also highlights the significance of inherent photo-thermal stability of active layer blends. The degradation of devices herein have been evidently driven by evolution of the blend morphology, as reported by Morse *et al.* As discussed in section 1.6.2, the diffusion of fullerene molecules within the BHJ is acknowledged to be a root cause of this undesirable phenomenon. Recent work in our group revealed the potential of oligofullerenes in combating the fast initial degradation of OPV devices on exposure to thermal stress, effectively improving their shelf-lives.¹⁵⁵ This concept is further exploited in the following chapters, which details the formation of stable main-chain poly(fullerene)s via a one-pot synthetic route and further discusses their photo-physical and photovoltaic properties.

Chapter 5

Novel poly(fullerene)s for photovoltaic applications

This chapter details the synthesis and characterization of three different poly(pyrrolidinofullerene)s obtained via the SACAP route, which is based on the Prato reaction. The use of PCBM in place of C₆₀ as a co-monomer is found to yield higher molecular weights and improved solubilities, affording easier handling and purification. First part of the chapter reports on the formation of poly(PCBM-benzene) with weight average molecular weights (M_w) as high as 25500 g mol⁻¹ as obtained from GPC. A second part of the chapter explores the use of thiophene flanked DPP in SACAP polymerizations to yield structures with alternating fullerene and chromophoric units.

Parts of this chapter have been published in

‘Sterically Controlled Azomethine Cycloaddition Polymerization of Phenyl-C₆₁-Butyric Acid Methyl Ester’; M. Stephen, H. H. Ramanitra, H. Santos Silva, S. Dowland, D. Bégué, K. Genevičius, K. Arlauskas, G. Juška, G. E. Morse, A. Distler, R. C. Hiorns, *Chem. Commun.* **2016**, 52, 6107

And will be published in

‘An alternating poly(fullerene) containing dyes for photovoltaic applications’; M. Stephen, S. Dowland, A. Gregori, H. R. Ramanitra, H. S. Silva, C. M. S. Combe, D. Bégué, C. D.-Lartigau, K. Genevičius, K. Arlauskas, G. Juška, A. Distler, R. C. Hiorns, *submitted*.

Modelling studies included in this chapter have been carried out by Dr. Hugo. S. Silva and Dr. Didier Bégué at UPPA.

Cyclic Voltammetry measurements have been carried out by Mr. Artiom Magomedov at Kaunas University of Technology.

The research leading to these results has received funding from the European Union Seventh Framework Program (FP7/2011) under grant agreement ESTABLIS no. 290022

5.1 Introduction

Since the initial discovery of fullerenes by Kroto *et al.* in 1985,¹⁵⁶ their unique properties promising for diverse applications has attracted scientists across various disciplines. The science of fullerenes has thus evolved into a rich multidisciplinary field including organic/bio electronics¹⁵⁷, pharmaceuticals¹⁵⁸ and nanotechnology.¹⁵⁹ The name “fullerene” derives from the US-American architect Richard Buckminster Fuller, who became famous for the development of geodesic domes in the 1960s. Fullerenes consist of carbon atoms only and, thus, constitute a novel carbon allotrope next to the well-known graphite and diamond.¹⁶⁰ The smallest fullerene that has been identified is C_{20}^+ , and the largest has well over 100 carbons. The most symmetrical, and therefore the most stable fullerene is C_{60} , followed by C_{70} , with the others being much less stable.¹⁶¹ However, these carbon clusters are insoluble or sparingly soluble in most solvents and consequently, are difficult to handle.

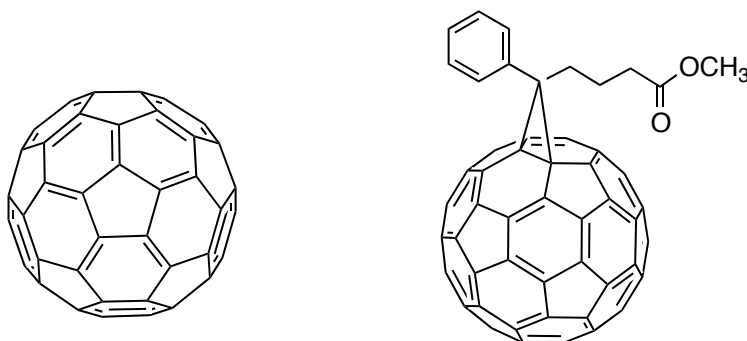


Figure 5.1. Structures of C_{60} (left) and $PC_{61}BM$ (right)

The structure of C_{60} (figure 5.1) resembles that of a soccer ball, consisting of 20 hexagonal and 12 pentagonal rings as the basis of an icosahedral symmetry (I_h) closed cage structure.¹⁶² Each carbon atom is bonded to three others and can be described approximately by an sp^2 configuration. However, curvature of the fullerene cage leads to a small admixing of the sp^3 character,¹⁶³ effectively exhibiting an orbital hybridization of $sp^{2.27}$. The bonds between two hexagons

([6,6] bonds) are found to be shorter than those between a hexagon and a pentagon ([5,6] bonds) and the lowest energy Kekulé structure of C₆₀ is that with all the double bonds located at the junctions of the hexagons ([6,6]-double bonds).¹⁶⁴ Consequently, the [6,6]-double bonds are found to be most susceptible to chemical reactions. The chemistry of C₆₀ is characteristic of electron deficient alkenes, hence it reacts with nucleophiles with its [6,6] bonds being good dienophiles. Nucleophilic addition and cycloaddition reactions are commonly exploited for chemical modifications on the fullerene sphere.¹⁶⁵ Release of surface strain is known to be an additional driving force for the formation of exohedral adducts.¹⁶⁶

Functional fullerenes not only can maintain the unique characteristics of pristine fullerenes, such as high electron affinity¹⁶⁷ and superior ability for electron transport,^{168,169} but also can provide desirable processability. So far, the soluble methanofullerene derivative, 6,6-phenyl-C₆₁-butyric acid methyl ester (PC₆₁BM) and its C₇₀ analogue PC₇₁BM remain the most widely used acceptors for BHJ solar cells. Their use in organic photovoltaics (OPV) was cemented by the observation of an extremely fast photo-induced electron transfer from optically excited conjugated polymers to the C₆₀ molecule in early 1990s.^{170,171} The additional quality of self-organisation in such a way as to favour electron collection and percolation in active layer blends has benefited their use in BHJs.^{172,173}

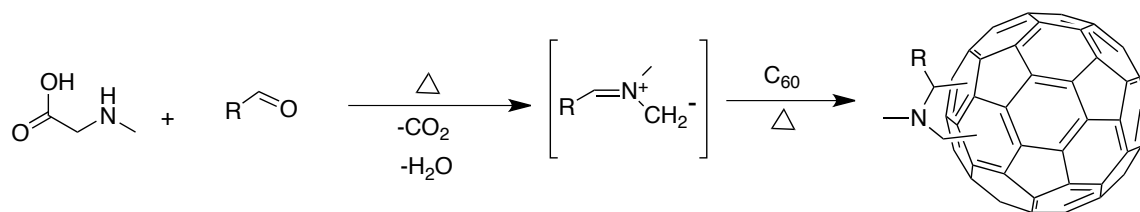
Today, as the OPV community is focused on improving stability of these devices, controlling the nanomorphologies of active layer blends over longer working periods becomes increasingly relevant.¹⁷⁴ As discussed in section 1.6, the tendency of fullerene spheres to diffuse through the film to form aggregates, especially at elevated temperatures typically reached during realistic working conditions, is undesirable in this regard.¹⁷⁵ Functionalized fullerenes have been reported to restrain the diffusion and crystallization of PCBM, greatly enhancing the morphological stability of active layer blends.¹⁷⁶ Use of copolymers in which

the donor and acceptor moieties are covalently bound so as to prevent their large-scale segregation comes across as a stimulating concept in this regard. A few examples found in literature include diblock co-polymers bearing bridged iminofullerenes,^{177,178,179} or double-cable polymers where fullerene moieties are covalently grafted onto a π -conjugated polymer backbone through an alkylphenylene linkage.^{180,181} However, such structures obtained *via* grafting approaches do not strictly preclude the aggregative behavior of fullerenes.¹⁷⁹

Incorporating fullerenes into the main-chain of a polymer is a rational strategy to this end, since it effectively restricts the motion of individual spheres within the film. However, co-polymers with C₆₀ units in the main-chain of the polymer are scarcely known, primarily due to the difficulty in monitoring the number of additions to the C₆₀ sphere, resulting in cross-linked products, besides the formation of regioisomeric mixtures due to the unique symmetry of fullerenes.¹⁸² Nevertheless, prior work by Hiorns *et al.* demonstrated directed, paired radical additions to C₆₀ ring at 1,4-positions *via* the atom transfer radical addition polymerization (ATRAP) route.¹⁸³ However, the requirement of CuBr for the formation of radicals in ATRAP elicits concerns of detrimental impact on device operation with even minute residual impurities.¹⁸⁴

Recent work in our group showed the potential employability of so-called Sterically controlled Azomethine ylide Cycloaddition Polymerization (SACAP) route for obtaining high molecular polymers, where the use of sterically cumbersome groups provided for a certain degree of control over the additions to the fullerene sphere.¹⁸⁵ The added benefits of being a one pot synthesis and free from metal catalysts makes this route particularly interesting. As reported in reference 185, studies carried out by Ramanitra *et al.* explored correlations between steric bulk of co-monomer, temperature and reaction times to the final yield and properties of the product formed with C₆₀ *via* SACAP. Molecular weights as high as 10840 g mol⁻¹ (M_n against polystyrene standards) were obtained using dodecyl-terephthalaldehyde as co-monomer in dichlorobenzene. It was

found that the choice of comonomer has a great role in determining the molecular weights of the final products: the greater the bulk of the comonomers, the more effective the blocking of multiple attacks on the fullerene and the reduced the number of cross-links.



Scheme 5.1. *The Prato reaction.*

The mechanism of SACAP is based on the well-known Prato reaction, which is a [1,3] dipolar cycloaddition of azomethine ylide across the [6,6] position of the fullerene (Scheme 5.1). The required ylide is produced by condensation of *N*-methylglycine (sarcosine) with an aldehyde, which in turn reacts with fullerene affording exclusively the product of cycloaddition across a 6,6 ring junction of the fullerene.¹⁸⁶ The Prato reaction is a powerful route to obtaining 2-substituted *N*-methyl-3,4-fulleropyrrolidines with the choice of starting aldehyde. When the reaction is carried out in the presence of large excesses of reagents, up to nine pyrrolidine rings can be introduced.¹⁸⁷

This chapter demonstrates the extended scope of SACAP route to yield copolymers incorporating C_{60} as well as PCBM in the main-chain. The first part follows up on the work reported by Ramanitra *et al.*, where the feasibility of incorporating PCBM instead of C_{60} as co-monomer in obtaining poly(fullerene) structures is exemplified. Synthesis and detailed characterization of an alternating poly(fullerene) based on terephthalaldehyde and PCBM units is reported. The product poly{[bispyrrolidino(phenyl- C_{61} -butyric acid methyl ester)]-*alt*-[2,5-bis(octyloxy)benzene]} (PPCBMB) is found to be soluble in common organic solvents and displays molecular weights (M_w) $>25000 \text{ g mol}^{-1}$ from GPC data, against polystyrene standards. When compared to the SACAP of C_{60} ,¹⁸⁵ it is found

that PCBM permits the formation of even higher molecular weight polymers with greater solubilities and easier handling.

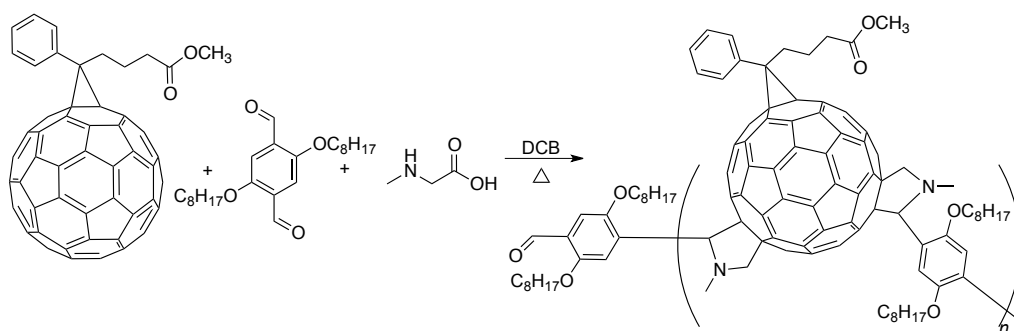
A second part of the chapter (section 5.3) reports on inclusion of dye moieties to obtain polymers and oligomers made of alternating dye and fullerene units, with an extended absorption in the visible region. The SACAP route is employed with diketopyrrolopyrrole (DPP) as co-monomer to yield polymers and oligomers with molecular weights greater than 5600 g mol⁻¹ with C₆₀ and greater than 11200 g mol⁻¹ with PCBM. The products obtained are named poly[(dodecyl dithiophene-diketopyrrolopyrrole)-*alt*-bispyrrolidinofullerene] (PDPF) and poly[(dodecyl dithiophene-diketopyrrolopyrrole)-*alt*-(bispyrrolidino-phenyl-C₆₁-butyric acid methyl ester)] (PDPPCBM).

5.2 Synthesis & characterization of PPCBMB

The polymerization was carried out in accordance with Scheme 5.2 as a one-pot reaction using commercially supplied products. Comonomers with alkoxy-aromatic groups were chosen due to their expected high solubility and stability against photo-oxidation.⁸² From the SACAP of C₆₀,¹⁸⁵ it was found that 2,5-bis(octyloxy)terephthalaldehyde provides reasonably high molecular weights, however, the reaction did tend towards slight crosslinking due to the relatively small size of the comonomer; the use of 2,5-bis(dodecyloxy)terephthalaldehyde yielded much higher molecular weights. However, the latter was not commercially available, whereas 2,5-bis(octyloxy)terephthalaldehyde was. Furthermore, it was expected that the phenyl butyl methyl ester group on PCBM would arrest any tertiary additions to the C₆₀ sphere.

The knowledge acquired from previous experiments with SACAP in our group went a long way towards optimising the reaction conditions. The required ylide is afforded from the reaction of *N*-methylglycine (sarcosine) with 2,5-bis(octyloxy)terephthalaldehyde. Given the relatively low reactivity of C₆₀ bonds,

the temperature was elevated to 150 °C to help the reaction forward. The ratio of reagents (1:2:1, respectively, PCBM : sarcosine : 2,5-bis(octyloxy)terephthalaldehyde) was chosen so as to avoid the formation of tris-adducts, known to appear when reaction times are relatively long.¹⁸⁸ Fullerene is known to undergo sigma-sigma reactions under exposure to light, and forms crosslinked ethers with oxygen.¹⁸⁹ PCBM also forms ethers.¹⁹⁰ Therefore the reaction was carried out under anaerobic conditions and under cover from UV light.



Scheme 5.2 Synthetic route to PPCBMB. Note that a most probable regioisomer is shown.

It is known that purifications of polymers containing fullerene can be troublesome; the C₆₀ tends to aggregate with the product. However, we found that the product was easy to purify. It was reprecipitated from methanol and Soxhlet-washed with acetone for three days (until the brownish colour of the wash solution disappeared). The product was then recovered by toluene and dried under vacuum for two days. It was found to be well soluble in common organic solvents (for example, 30 mg mL⁻¹ in xylene was feasible), indicating a very low degree of crosslinking between chains. The product was shiny black in appearance and formed smooth thin films when cast from solution. (Figure 5.2)

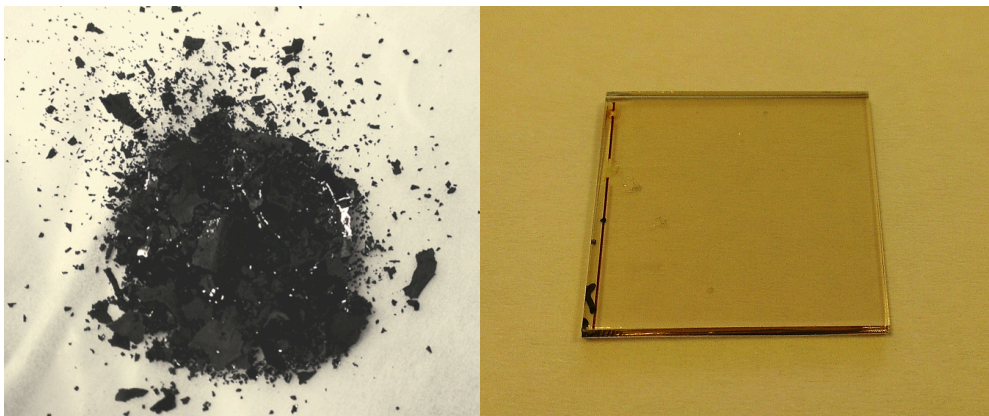
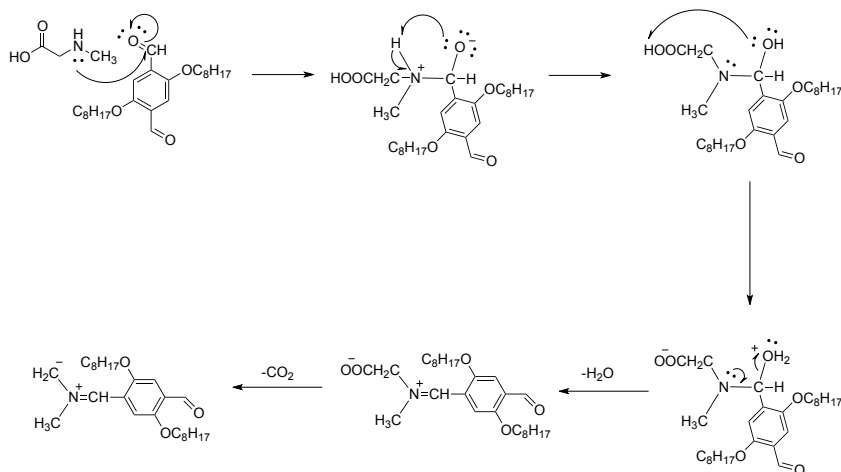


Figure 5.2. Image of PPCBMB powder (left) and thin film (~50 nm) of PPCBMB on ITO-glass substrate casted by blade coating from *o*-xylene.

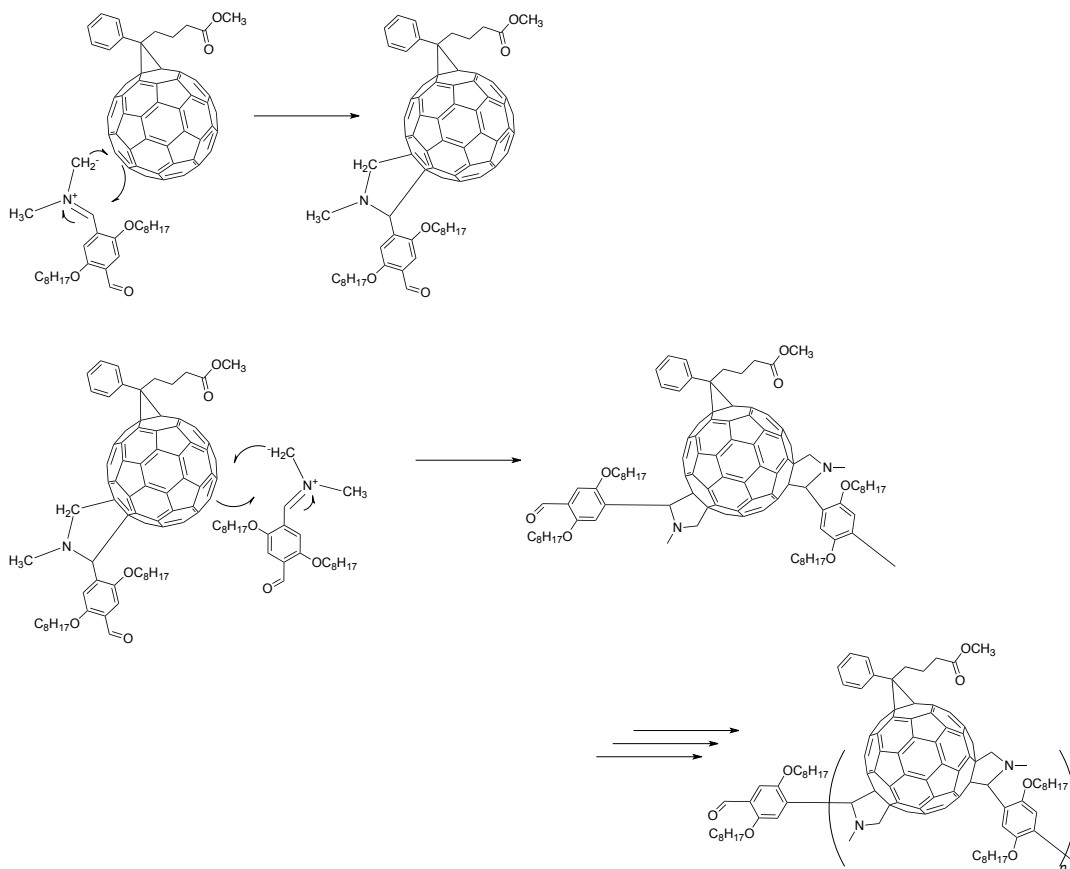
A general mechanism of the reaction is given in scheme 5.3. Firstly, the dialdehyde reacts with sarcosine to generate the azomethine ylide, which is a 1,3 dipole. Since our reaction consists of two equivalents of sarcosine with one equivalent each of dialdehyde and PCBM, it is reasonable to expect ylide formation on both sides of terephthalaldehyde, which in turn carries forward the polyaddition as shown in scheme 5.3 b. It is thought that in SACAP, tertiary additions are reduced by employing sterically cumbersome comonomers.

The number of additions is controlled to just two per fullerene by the ratio of reagents and the steric bulk of the DPP. There are, however, 30 [6,6]-bonds around the C₆₀ and therefore when there are two additions to the sphere, there are eight possible regioisomers (figure 5.3).¹⁸⁸ When there are three additions, 46 regioisomers are possible. Therefore, in the case of PDPPCBM, there are the two additions as well as the phenyl ester group already present; in effect, we can expect anywhere up to 46 regioisomers along the chain.

(a)



(b)



Scheme 5.3 Mechanism of SACAP reaction; (a) dialdehyde reacts with sarcosine to generate the 1,3 dipole - azomethine ylide; (b) The 1,3-dipole generated in-situ reacts with dienophile ([6,6]-bond of PCBM) in a concerted fashion (1,3 dipolar cycloaddition) to provide the corresponding pyrrolidine and repeated cycloadditions yields the polymer. Note, for the sake of clarity, only the most probable regioisomer is shown.

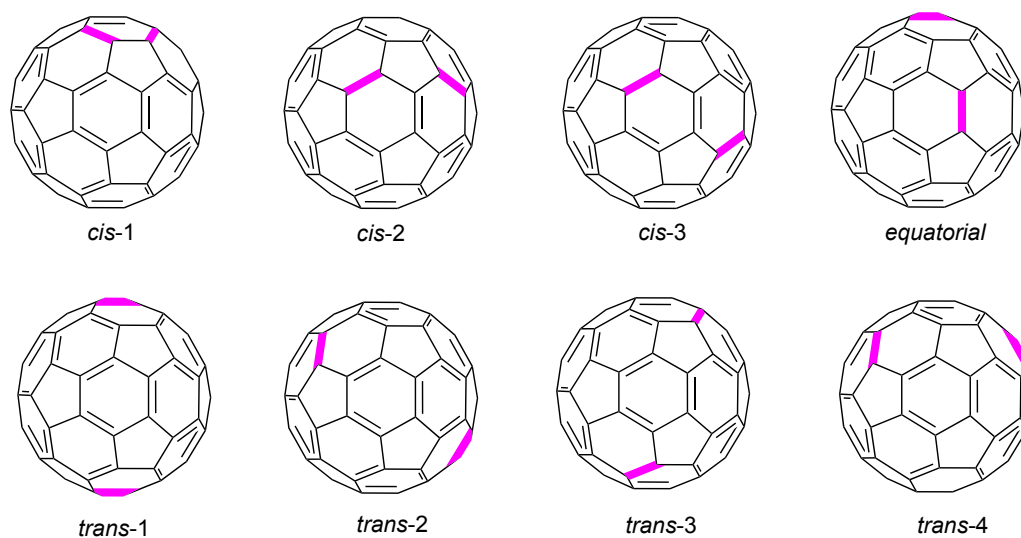


Figure 5.3. Addition patterns of bisadduct isomers.¹⁸⁸

The GPC curve of a representative sample of PPCBMB in THF is shown in Figure 5.4. The monomodal peak eluting at *ca.* 17 min indicates an absence of oligomers and unreacted reagents. The estimated molecular weights, against polystyrene standards, are 7000 g mol⁻¹ (M_n) and 23000 g mol⁻¹ (M_w), with a dispersity ($D = M_w/M_n$)¹⁹¹ of 3. It is acknowledged that molecular weights of fullerene containing polymers with respect to polystyrene standards are extremely underestimated due to reduced solubility of these materials in THF relative to polystyrene, resulting in a lower hydrodynamic volume¹⁹² as well as possible π - π interactions between fullerene units and polystyrene stationary phase retaining them for longer times.¹⁹³ Indeed, we found that in our apparatus, PCBM and toluene eluted at *ca.* 22 min, erroneously indicating that PCBM would have a mass of 110 g mol⁻¹! Therefore these values considerably underestimate the real molecular weight of the materials. The small bump at 21.85 min corresponds to PCBM (figure A2.12, appendix 2). Deconvolution of the peaks indicated that there was less than 0.3% residual PCBM.

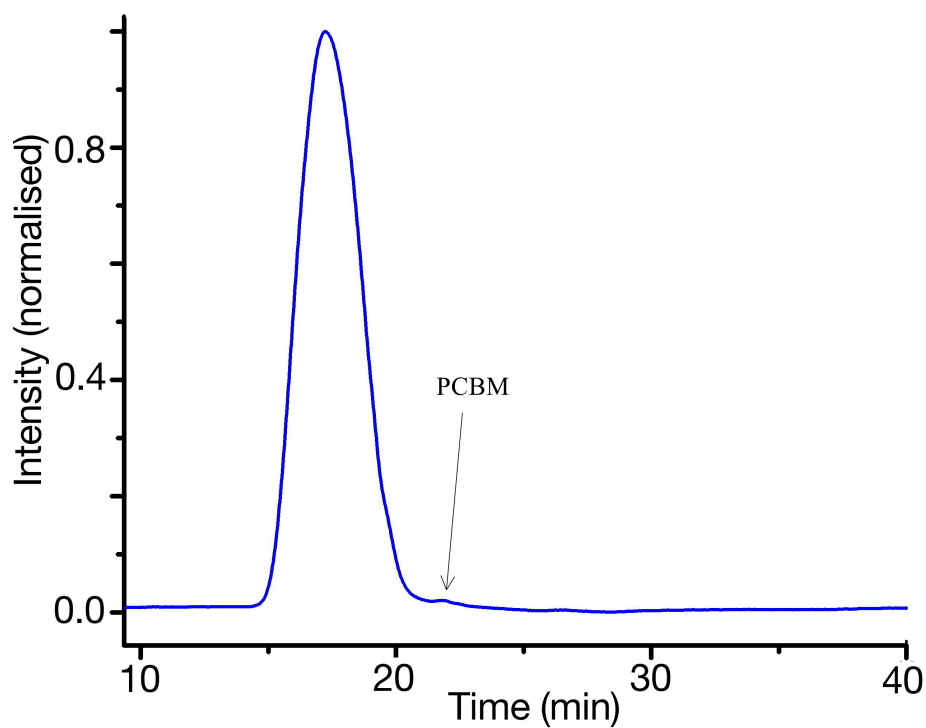


Figure 5.4 Representative GPC profile (THF, 30 °C, 330 nm) of PPCBMB.

Representative NMR spectra of the starting materials and the product are shown in Figure 5.5. The only new peaks seen in the polymer fall in the region where one would expect the protons on the pyrrolidine ring to appear, where the comonomers do not have any contributing protons. The peak in the aldehyde region seen with bis(octyloxy)terephthalaldehyde disappears.

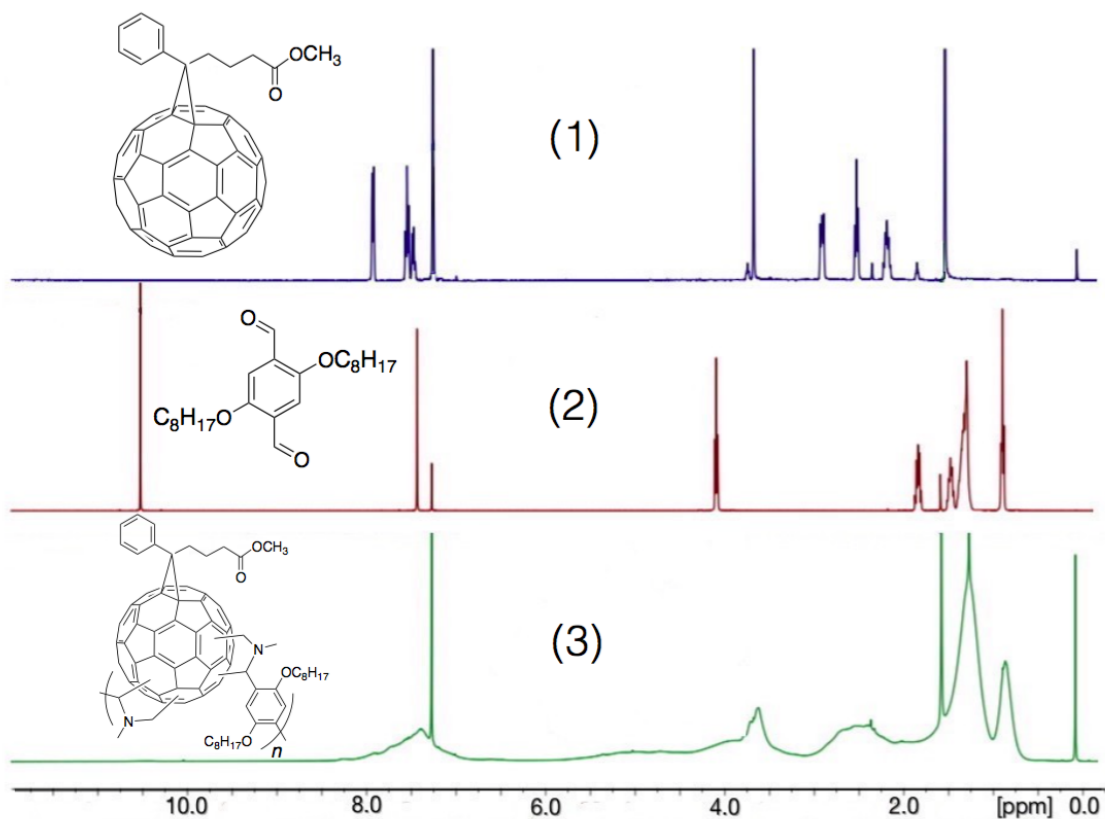


Figure 5.5 Overlay of ^1H NMR (CDCl_3 , ambient temperature) of: (1) PCBM; (2) 2,5-bis(octyloxy)terephthalaldehyde; and (3) PPCBMB

The ^1H NMR (figure 5.6) shows a broad signal in the aromatic region peaked at 7.38 ppm that appears to have six shoulders spanning from 8.25 to 7.00 ppm. From the NMR spectrum of monomer, it was observed that the phenyl substituent on PCBM showed multiplets centred at 7.94 ppm, 7.55 ppm and 7.47 ppm. The phenyl group of 2,5-bis(octyloxy)terephthalaldehyde resonates at 7.42 ppm. Hence at this moment it is not clear whether the presence of different isomeric forms, or variations along the polymer chain, contribute to the shoulders. The general broadness of all the peaks confirm that the material is polymeric in nature. The broad signal centered at 5.02 ppm arises from protons within the pyrrolidine linkage, whereas the rather sharp signal at 3.61 ppm is attributed methyl esters and is convoluted with oxymethylene protons in the alkyl side-

chain. The pyrrolidine *N*-methyl protons and PCBM propylene protons create a broad signal centred at 2.52 ppm. The aldehyde end groups afford the small broad bump at 10.46 ppm while a sharp peak at 10.03 ppm represents a tiny amount (*ca* 0.1 wt%) of comonomer.

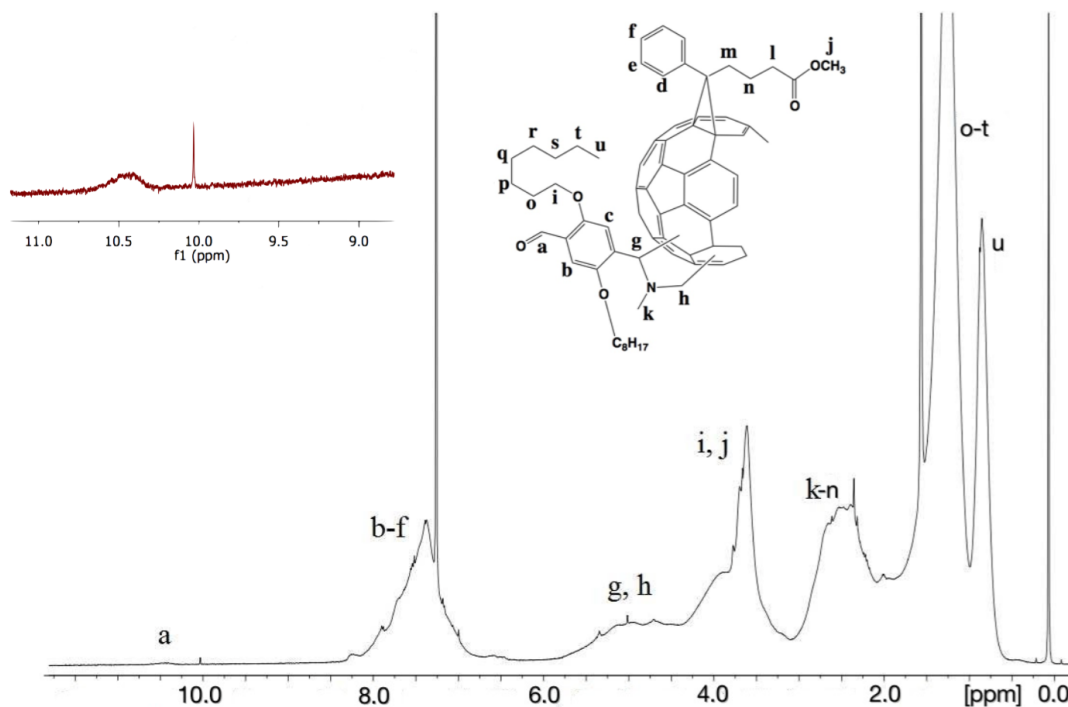


Figure 5.6 ¹H NMR (CDCl₃, ambient temperature) of PPCBMB, with the inset showing the aldehyde region enlarged.

Given the aforementioned mismatch between GPC estimated and real molecular weights, an attempt at a further estimation was made using ¹H NMR. It was assumed that each macromolecule carried on average one –CHO group, not unreasonable given that the polymerization is a polyaddition.¹⁹⁴ Integrating the ¹H NMR peak at 0.85 ppm for pendent comonomer methyl groups gave a value of 109 *versus* 1 for the aldehyde protons at 10.46 ppm. Assuming a respective ratio of six methyl protons to 1 aldehyde proton in the repeating unit, we infer the

degree of polymerization to be $109/6 = 18.2$. Multiplying this by the repeating unit molar mass affords $M_n = 24670 \text{ g mol}^{-1}$, which is considerably higher than that shown by GPC, and most likely closer to the real value.

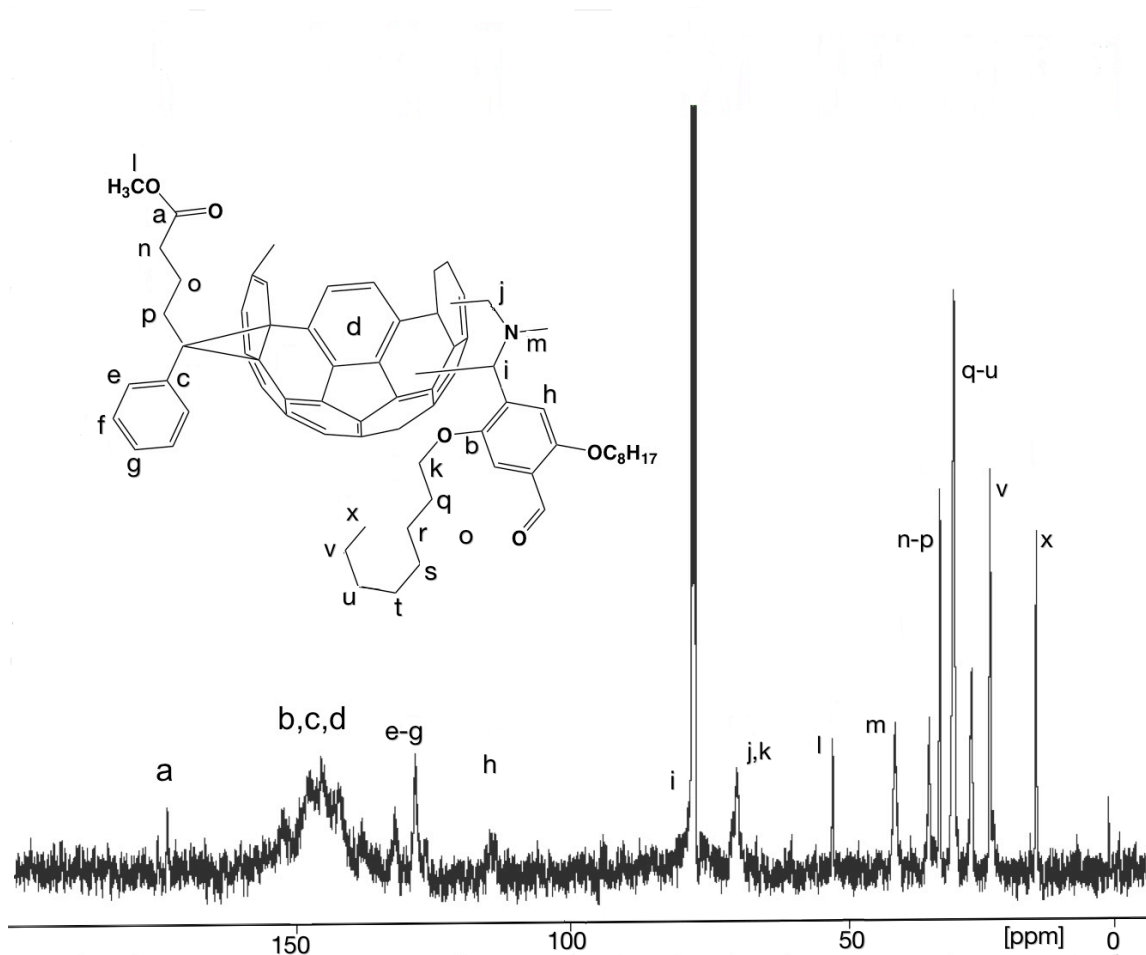


Figure 5.7 ^{13}C NMR (CDCl_3 , ambient temperature) of PPCBMB

Figure 5.7 shows the ^{13}C NMR of PPCBMB. The peaks corresponding to the fullerene cage are broadened by the polymeric nature of material and merged with peaks due to substituent phenyl quaternary carbons. The carbons associated with the pyrrolidine linkage are observed at 40.1 ppm and 69.2 ppm, corresponding to *N*-methyl and methine groups, respectively. The resonance of the methylene group appears to have merged with the triplet of chloroform, as revealed by the 2-D NMR shown in figure 5.8. The 2-D NMR further confirms

these results, with notable correlations for methine, methylene and methyl groups of the pyrrolidine linkage.

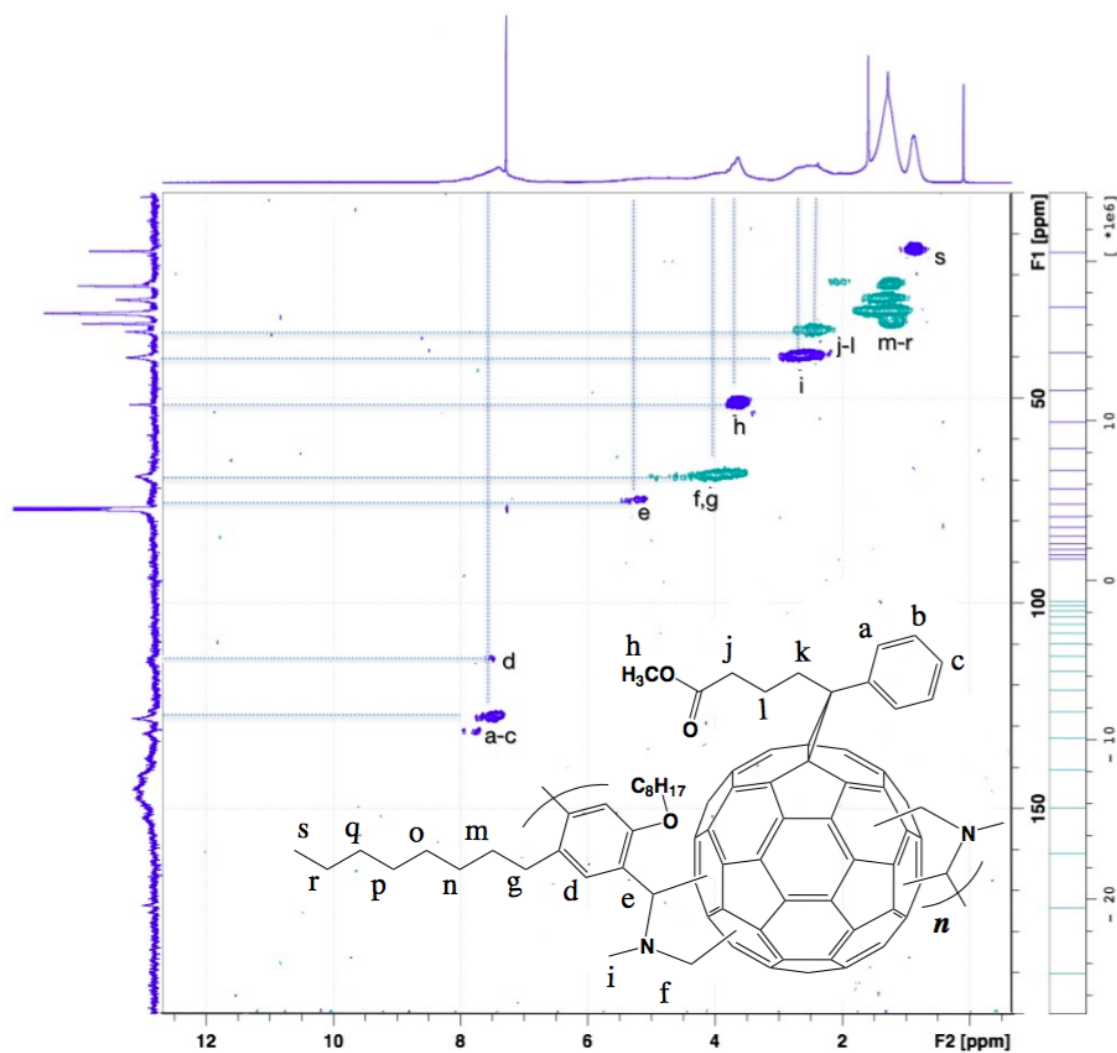


Figure 5.8 HSQC 2D NMR (CDCl_3 , ambient temperature) of PPCBMB. Data points in blue correspond to methine and methyl groups while those in green indicate methylenes.

The DOSY ^1H NMR spectrum of PPCBMB (figure A1.1, appendix 1) shows the diffusion profile of the polymer. The protons are all in the same regime, confirming the monomodal nature of the molecular weight distribution.

Theoretical calculations were carried out to gain insight into the molecular geometry of PPCBMB. Marchesan *et al.* demonstrated the order of preferential additions among the numerous possible tris-adduct structures for azomethine ylide

cycloadditions to the C_{60} sphere.¹⁹⁵ The relative yields of the tris-adducts indicated the favored formation of *trans*-2, *trans*-3, *equatorial*, followed by *trans*-3, *trans*-4, *equatorial* and by the tris-adducts displaying a *cis*-2 addition pattern. The nomenclature used here is adopted from Hirsch *et al.*¹⁹⁶ Basically, if we call the three addends 1, 2, and 3, the first stereo chemical relationship is between 1 and 2, the second between 2 and 3, and the third is between 3 and 1. However, the relative complexity of the peaks and the numerous isomers that are possible means that the identification of regioisomers cannot be performed without extensive studies using model molecules. It is expected that this will be the focus of future work. It is most likely though, given the steric bulk of the substituents considered, that *cis*-isomers are excluded. Furthermore, we would expect the polymer to be regio-irregular.

To model the most probable isomeric structure of the repeating unit, PCBM was treated using DFT with B3LYP/6-31G** theoretical level (*appendix 2*).¹⁹⁷ Calculations were carried out assuming the regions of highest LUMO density to be the target of successive attacks,²⁴ to give the most probable tris-adduct PCBM-2 in Figure 5.9. Calculations detailed in appendix 2 estimate the relative LUMO levels to be raised in case of PPCBMB with respect to PCBM. It also predicts the reduction of electron affinity and the electrophilicity.

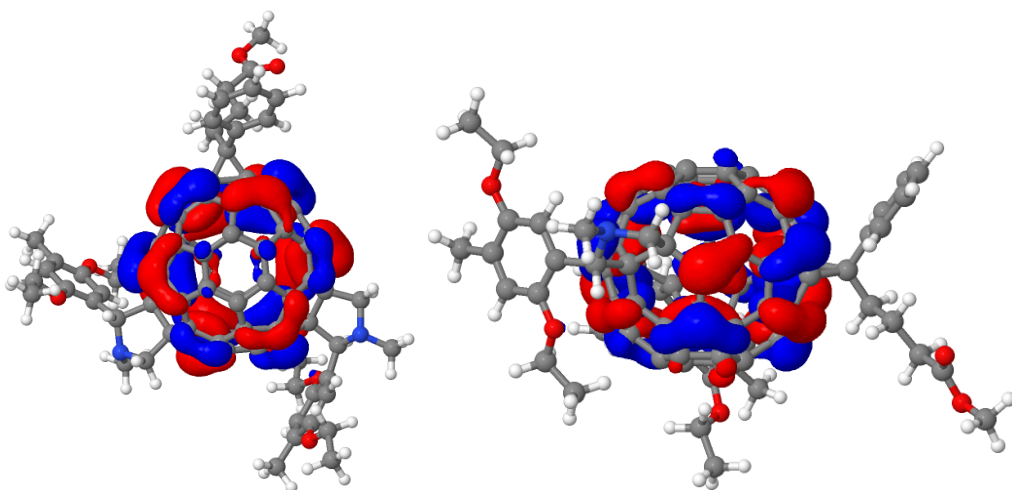


Figure 5.9. LUMO frontier orbitals for the most probable tris-adduct constituting the repeating unit of PPCBMB optimized using DFT B3LYP/6-31G** level of theory.

The U.V visible absorption spectrum of PPCBMB in toluene is shown in figure 5.10. In comparing the absorption spectra of PCBM, PPCBMB and 2,5-bis(octyloxy)terephthalaldehyde, it is found that the characteristic absorption maximum of 2,5-bis(octyloxy)terephthalaldehyde is lost due to disruption of conjugation by removal of aldehyde groups during the reaction. The absorption maximum of PPCBMB is also blue shifted with respect to PCBM owing to a disruption of fullerene cage conjugation.¹⁹⁸

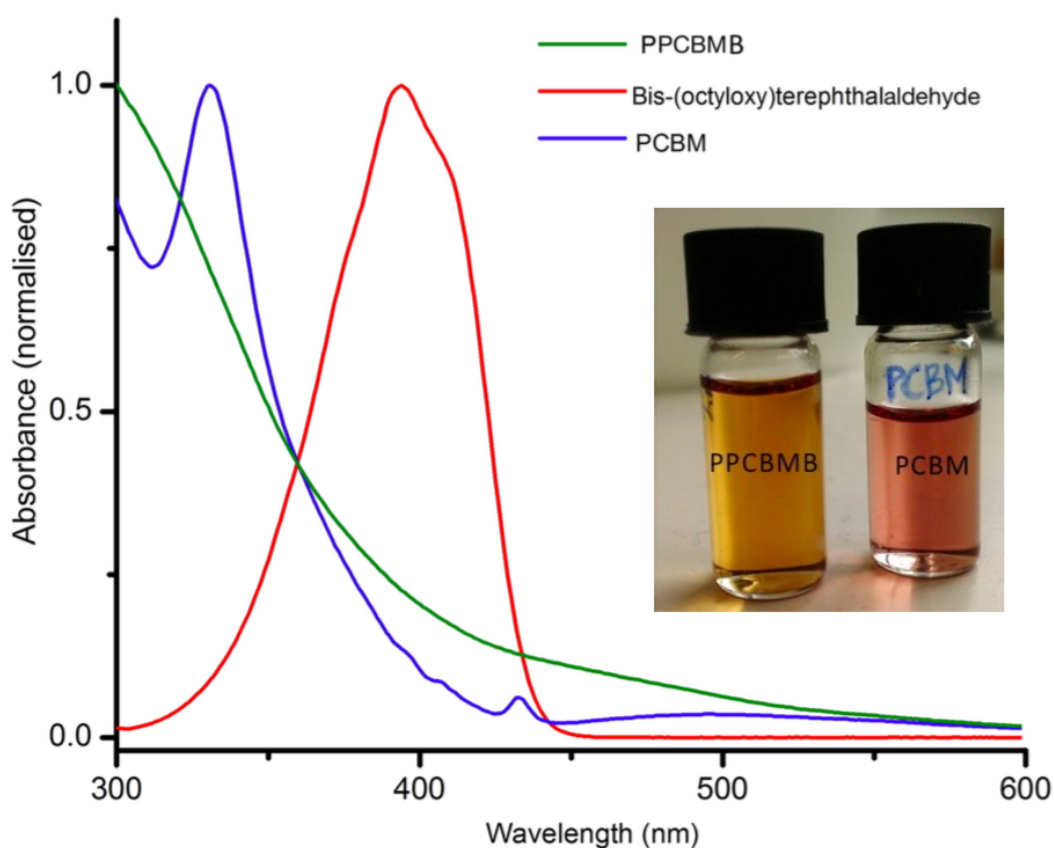


Figure 5.10. Normalised absorption of PCBM, 2,5-bis(octyloxy)terephthalaldehyde and PPCBMB in toluene. Inset shows an image of solutions of PPCBMB and PCBM in toluene.

The electronic states, that is, HOMO/LUMO levels of PPCBMB were investigated by using cyclic voltammetry (CV). The oxidation and reduction cyclic voltammogram of a solution of PPCBMB in ortho-

dichlorobenzene/acetonitrile (4:1 v/v) is shown in figure 5.11

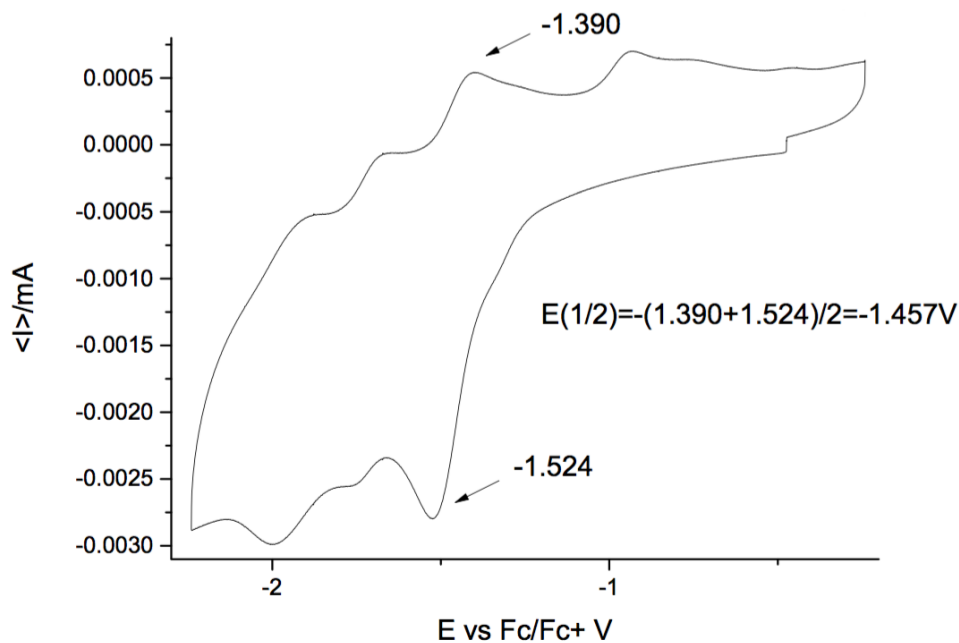


Figure 5.11 Cyclic voltammetry profile of PPCBMB.

Considering the energy level of ferrocene/ferrocenium is 4.8 eV below vacuum, the LUMO of PPCBMB is estimated using the equation

$$E_{\text{LUMO}} = - (E_{1/2} + 4.8) \text{ eV}$$

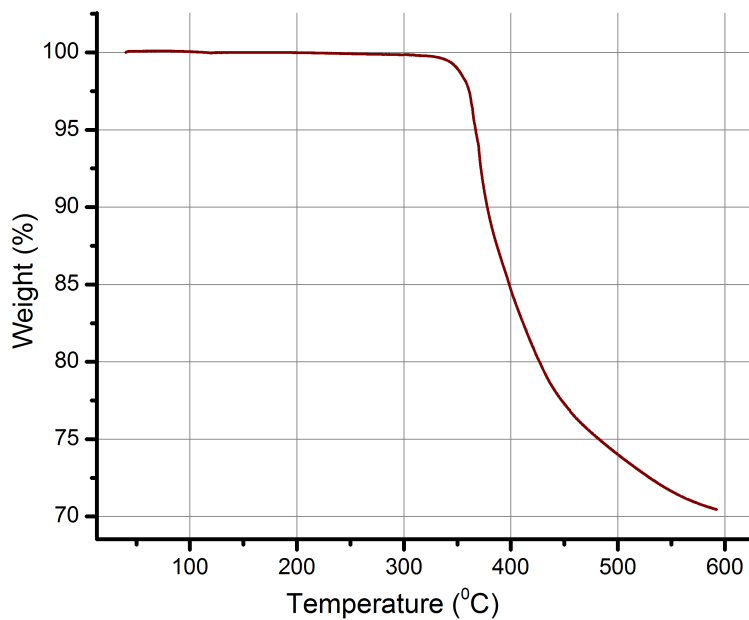
This yields a value of for $E_{\text{LUMO}} = -3.34$ eV for PPCBMB and $E_{\text{LUMO}} = -3.8$ eV for PCBM, under identical experimental conditions, conforming to values reported in literature for PCBM.^{199,200} This confirms the prediction of raising of LUMO levels by modeling studies previously discussed.

From Tauc's plot²⁰¹ (figure A2.10, appendix 2) $E_g \text{ opt.}$ of PPCBMB is estimated to be 2.26 eV, which gives $E_{\text{HOMO}} = -5.6$ eV.

Calorimetric characterisations were carried out to understand the thermal degradation profile and identify possible phase transitions. Figure 5.12 shows the thermogravimetric analysis (TGA) and differential scanning calorimetry (DSC) thermograms, respectively, of PPCBMB. The TGA demonstrates that the material is thermally stable to around 320 °C. PCBM is known to degrade at around 400

$^{\circ}\text{C}$.²⁰² The DSC curve, being smooth, indicates that the material is most likely amorphous, although further studies are required.

(a)



(b)

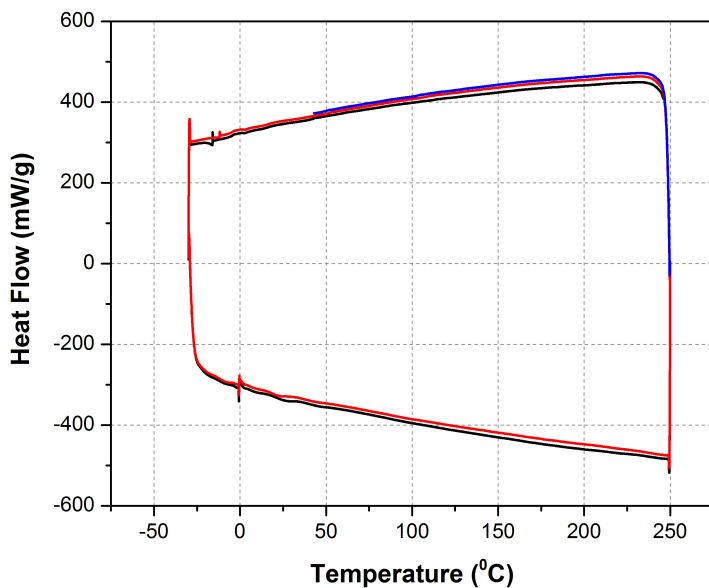
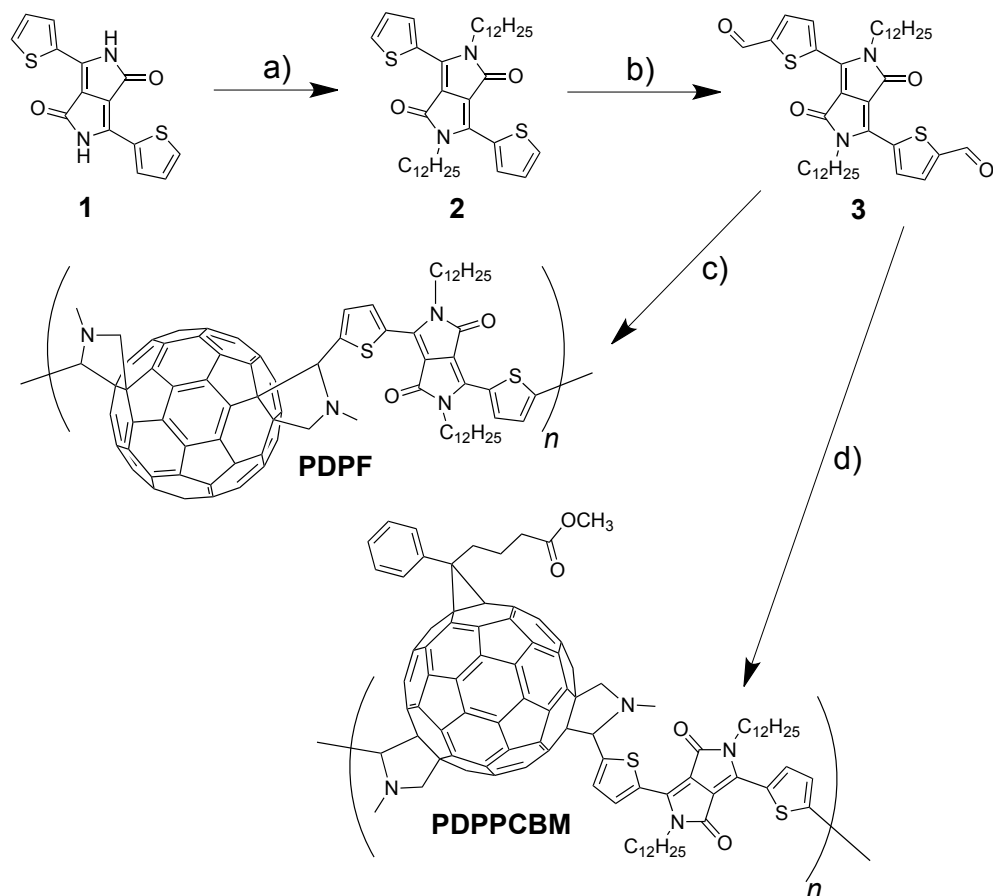


Figure 5.12. (a) TGA and (b) DSC thermograms of PPCBMB.

5.3 Synthesis & characterization of PDPF and PDPPCBM

A lot of work has gone into developing dyads and triads of fullerenes and dyes such as diketopyrrolopyrrole (DPP),^{203,204} phenothiazine,²⁰⁵ perylene,^{206,207} porphyrins,²⁰⁸ corroles,²⁰⁹ and phthalocyanines²¹⁰ for OPVs. It is understood that these materials will show improved light gathering due to the dye transferring excitation energy to the fullerene.²¹¹ DPP is of interest because of its high stability, industrialized production,²¹² its use as a chromophore in solar cells and good charge mobility,^{213,214} and its ability to raise the open-circuit voltage (V_{oc}) of an OPV cell.²¹⁵ Flanking the DPP core with thienyl units is known to boost the hole mobilities of these systems.²¹⁶ To our knowledge, alternating polymers of dyes and fullerenes have not been formed before. In the following section, the preparation and characterization of DPP-fullerene alternating main-chain polymers *via* SACAP in a facile one-pot reaction is detailed. It is expected that these materials would combine the opto-electronic properties of their smaller dyad and triad cousins, with the strengths of polymers.

The synthetic route to obtaining the two exemplar copolymers is detailed in Scheme 5.4. Alkylation of dithiophene-diketopyrrolopyrrole (**1**) was carried out using a literature procedure to give the well-defined products as indicated by ¹H and ¹³C NMR in Figure A1.2 of the appendix 1.²¹⁷ Lithiation of dodecyl-DPP (**2**) with LDA at -78 °C, followed by addition of *N*-formylpiperidine, afforded the corresponding dialdehyde **3**.²¹⁸ Apart from being sensitive to oxygen, temperature variations made during the reaction were found to have a strong impact on final yields. While many trials afforded a mixture of mono and di-aldehydes, a precise control of temperature yields pure dialdehyde, eliminating the need for tedious separation techniques.



Scheme 5.4. Reactions forming the alternating copolymers PDPF and PDPPCBM: a) 1-bromododecane, K_2CO_3 , 18-crown-6, DMF, 47%; b) lithium diisopropyl amide, *N*-formylpiperidine, **2**, THF, HCl, 46%; c) C_{60} , *N*-methylglycine, **3**, 1,2-dichlorobenzene, 67.1% for PDPF; d) PCBM, *N*-methylglycine, **3**, 1,2-dichlorobenzene, 72.2 % for PDPPCBM.

SACAP polymerisations were carried out in accordance with prior work, i.e., at 150 °C for 18 h in 1,2-dichlorobenzene with a ratio of 1:2:1, respectively, for C_{60} or PCBM : sarcosine : **3**. Considering the sensitivity of fullerene to oxygen and light, care was taken to maintain the reaction setup under nitrogen atmosphere, protected from UV-light. The brut product was Soxhlet washed for several days to remove unreacted reagents, with PDPF requiring significantly more time (i.e., six days with subsequent reprecipitation *versus* 16 h) than its PCBM counterpart, due to the difference in monomer solubilities. Figure A2.7 in *appendix 2* shows an overlay of GPC traces obtained for toluene fraction and

hexane fraction from Soxhlet wash of PDPF.



Figure 5.13. PDPPCBM during Soxhlet extraction with toluene (left) and reprecipitation from methanol (right).

Figure 5.14 shows the overlay of GPC curves for PDPF and PDPPCBM. Peak deconvolution indicated that PDPF retained *ca* 1wt% of C₆₀ even after several days of Soxhlet washing, and a negligible amount (0.2% relative mass) of PCBM in the purified PDPPCBM product. It is worth noting that the optical density of C₆₀ at the operating wavelength of 330 nm is thrice that of the copolymers, as discerned from absorption spectra of respective solutions with same concentration (*vide infra*). As mentioned before, the molecular weight estimations obtained from GPC against polystyrene standards do not justify fullerene-containing systems. PDPF is indicated to have an $M_n = 900 \text{ g mol}^{-1}$ for a dispersity ($D = M_w/M_n$) of 2.8, whereas PDPPCBM has an $M_n = 3300 \text{ g mol}^{-1}$ and $D = 1.9$; evidently these values are erroneous. Using chlorobenzene rather than THF as an eluent improves the elution of the materials slightly: PDPF is found to have $M_n = 2050 \text{ g mol}^{-1}$ and $D = 2.0$, whereas PDPPCBM has an $M_n = 3600 \text{ g mol}^{-1}$ and $D = 2.0$, and while more accurate, these values remain doubtful.

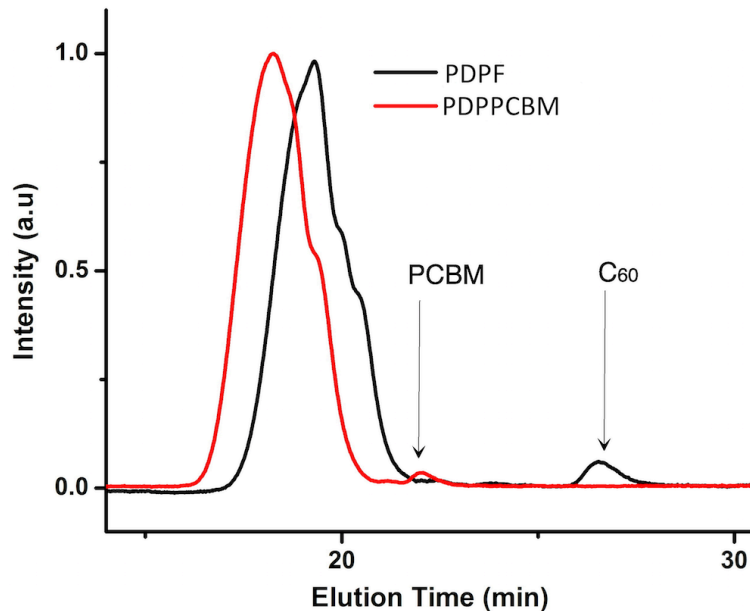


Figure 5.14. GPC profiles (THF, 30 °C, 330 nm) of PDPF and PDPPCBM

Prior work has shown the benefit of counting off consecutive peaks, assuming that each represents the growth of the chain by one repeating unit, thereby calculating a more realistic molecular weight.²¹⁹ While Gügel *et al.* demonstrated this for GPC data showing clearly distinct peaks, the same strategy could be applied for the apparent shoulders of the visibly more homogenous peaks we obtained. In the case of PDPF, discrete shoulders indicate the presence of oligomers with 1-3 repeating units before reaching a peak with 4 monomers, indicating that $M_p = 5650 \text{ g mol}^{-1}$. Visual inspection indicates that the oligomers reach a maximum of around 10 repeating units. However, in the case of PDPPCBM, much higher molecular weights are attained, with M_p reached with around 7 repeating units, i.e., $M_p \approx 11200 \text{ g mol}^{-1}$ and a maximum probably around 20 or so repeating units. It appears that the difference in solubilities and perhaps electronic properties of C₆₀ and PCBM influences their distinct retention times within the column, which is reflected in their respective elution times in figure 5.13. It can be assumed, however, that the values for dispersity are self-consistent and that they are around 2 would confirm the polyaddition nature of the

reaction.¹⁹⁴ Interestingly, that \bar{D} is higher for PDPF than PDPPCBM indicates that the former was arrested by precipitation from solution, whereas the latter was able to undergo a more ideal polyaddition. However, the values are several times lower than those for SACAP polymers made using C₆₀ or PCBM with a more soluble 2,5-bis(octyloxy)terephthalaldehyde comonomer, suggesting that their relatively poor solvation is hindering the reaction.²²⁰

The ¹H NMR of PDPF in Figure 5.15 was recorded in 1,4-dichlorobenzene at 80 °C due to its limited solubility in CHCl₃. This adds to the possibility of formation of aggregates in the solution, which is perhaps manifested in the nature of NMR peaks, affording several sharp shoulders in comparison to more homogeneously broadened peaks in case of PDPPCBM. The ¹³C NMR confirms the general structure and the polymeric nature by the breadth of the peaks.

The ¹H NMR of PDPPCBM in CDCl₃ shows broad signals centered at 5.04 ppm and 2.86 ppm, arising from the protons within pyrrolidine linkage and those of *N*-methyl group, respectively. The chain end aldehydes afford a small bump at 10.01 ppm. In the aromatic region, thiophene rings gives the broad signal centered at 8.91 ppm and the substituent phenyl rings gives rise to a broad signal centered at 7.36 ppm with several shoulders, which is not unexpected considering the multiplets observed in this region in bare PCBM. A broad signal centered around 4.05 ppm and rather sharp signal at 3.62 ppm correspond, respectively, to protons of dodecyl chain in the immediate vicinity of nitrogen and terminal methyl protons of ester group. The alkyl groups of the ester afford the broad signals centered at 2.71 ppm while the large signals centered at 1.21 ppm and 0.86 ppm correspond to alkyl groups of dodecyl chain.

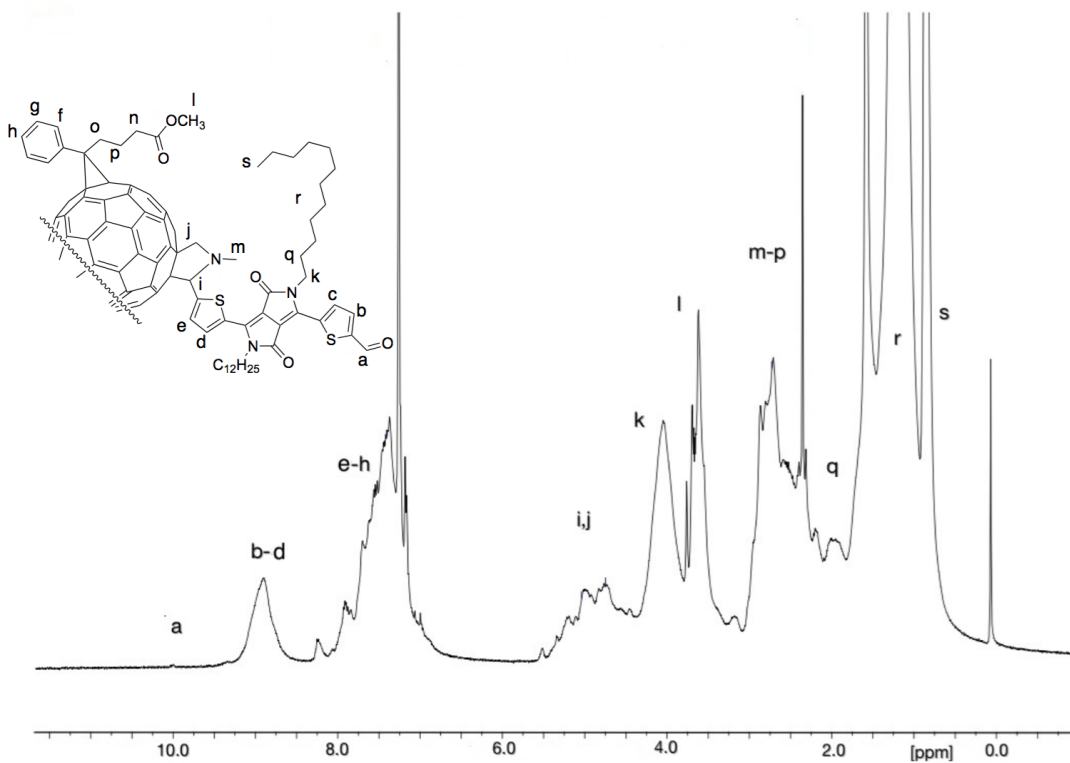
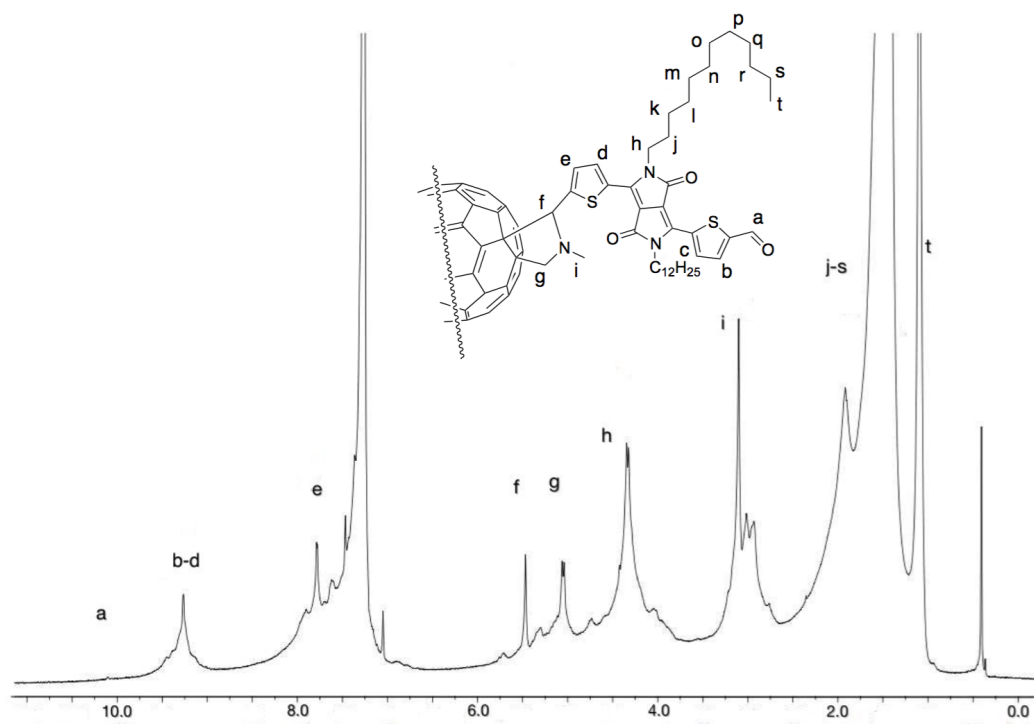


Figure 5.15. ^1H NMR of PDPF (1,4-dichlorobenzene, 80 °C), above; PDPPCBM (CDCl_3 , ambient temperature), below

An attempt at estimating molecular weights from NMR, using the integrals from aldehyde chain-ends and methyls from the comonomer dodecyl chains, found that for PDPPCBM, $M_n = 128600 \text{ g mol}^{-1}$, i.e., 38 times higher than that obtained from GPC, and for PDPF, $M_n = 635000 \text{ g mol}^{-1}$, 700 times higher! These calculations assume that relaxations are equivalent, and that the reactions underwent perfect polyadditions. However, a plausible discrepancy of relaxation times and presumable scenario of chain closing reactions delivers these calculations unreliable.

The ^{13}C NMR of PDPPCBM (Figure 5.16) shows broad peaks from *ca.* 135 to 155 ppm due to combined resonances of fullerene cage and quaternary carbons associated with thiophene, pyrrolopyrrole and substituent phenyl groups. With respect to PDPF, additional peaks are observed for PDPPCBM at *ca.* 128 ppm arising from aromatic phenyl carbons. Carbons associated with the pyrrolidine links resonate at 79 ppm (methine), 70 ppm (methylene) and 40 ppm (*N*-methyl). These results are further substantiated by the HSQC 2D NMR shown in Figure 5.17. Furthermore, the relative purity and monomodal nature of the molecular weight distribution of PDPPCBM was confirmed through the use of DOSY 2D NMR regime (Figure A1.4, *appendix 1*). The corresponding spectrum for PDPF could not be recorded due to its lower solubility.

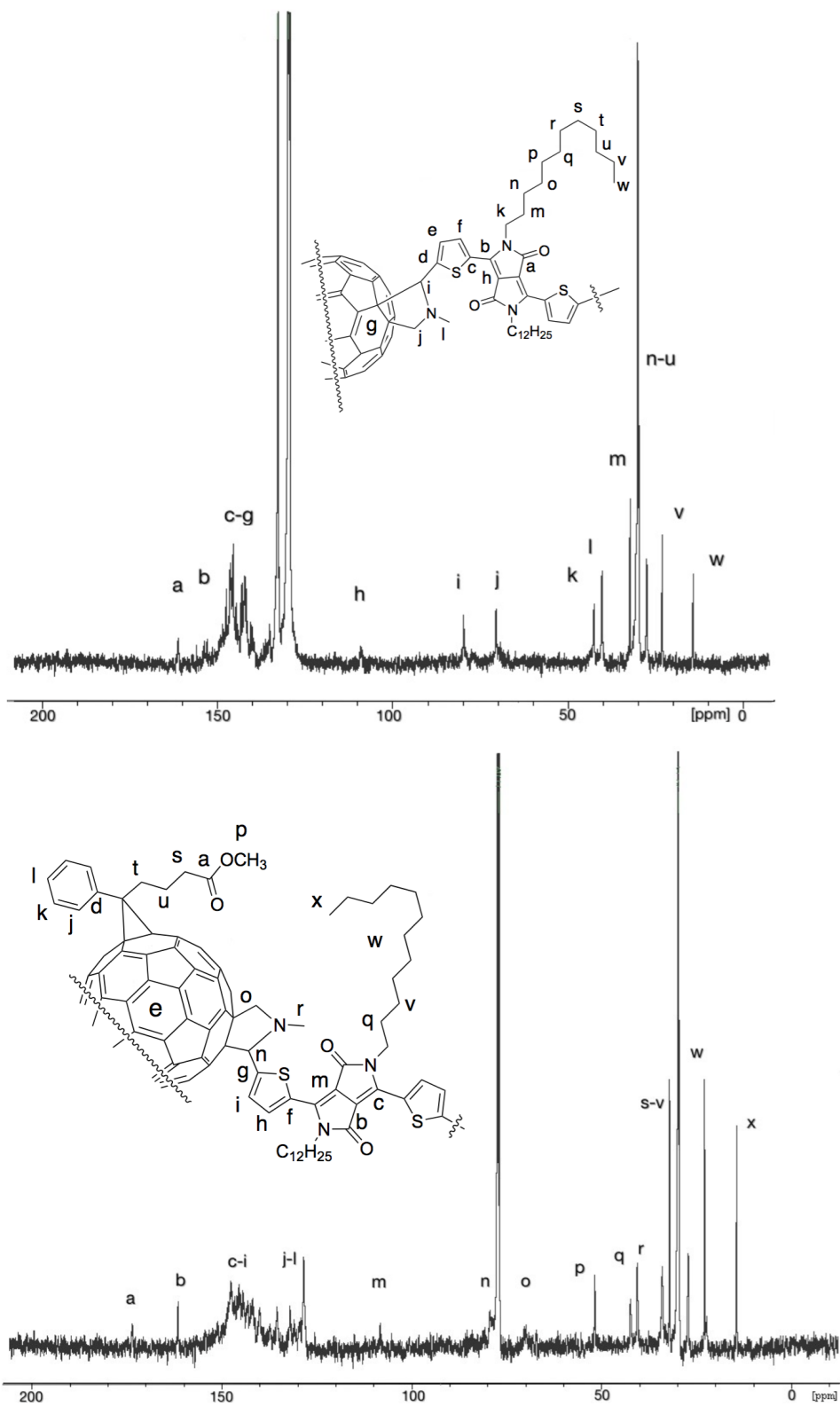


Figure 5.16. ^{13}C NMR of PDPF (1,4-dichlorobenzene, 80°C) above; PDPPCBM (CDCl_3 , ambient temperature), below

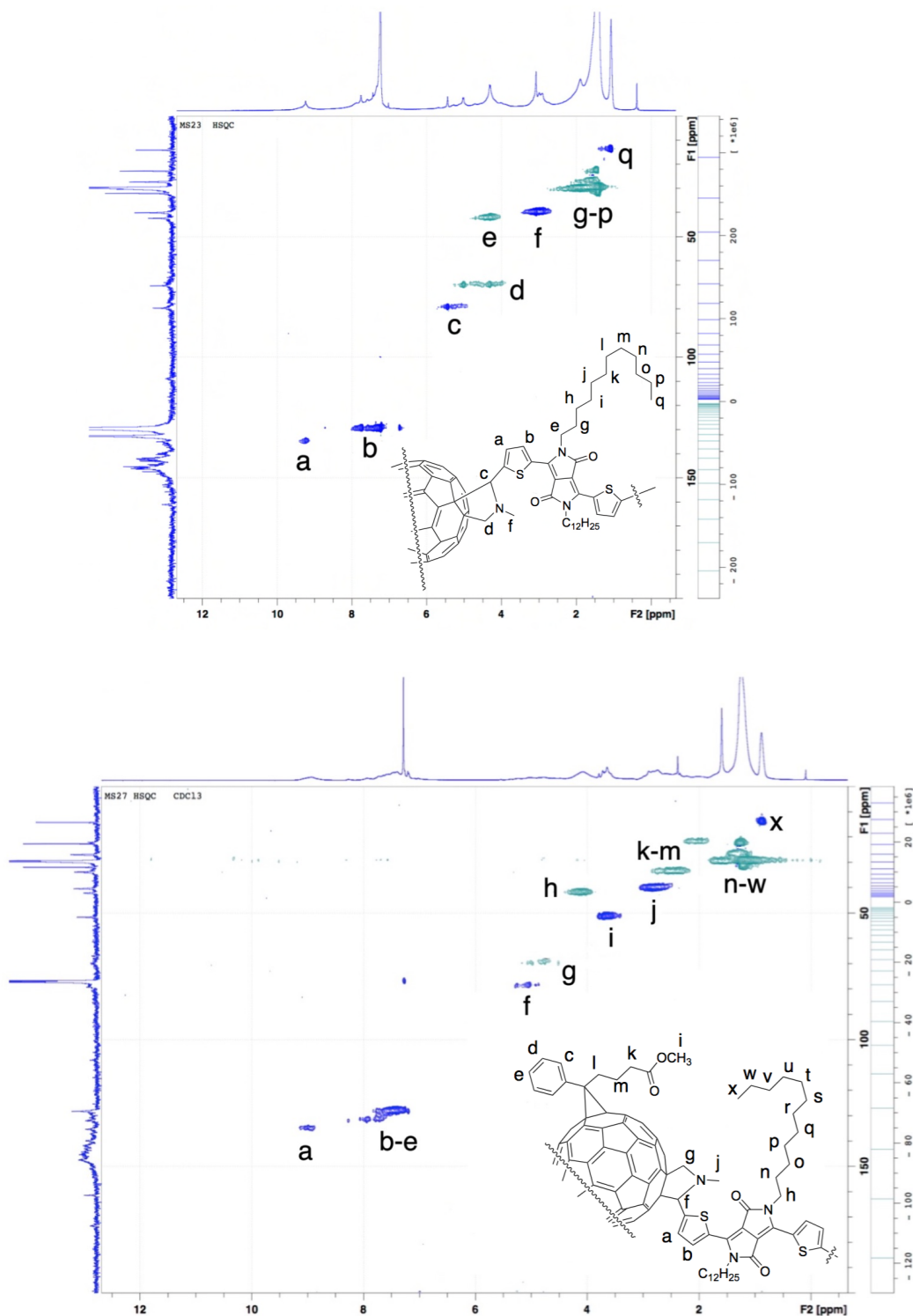


Figure 5.17. 2D HSQC NMR of PDPF (1,4-dichlorobenzene, 80 °C) above; PDPPCBM (CDCl₃, ambient temperature), below. Data points in blue correspond to methine and methyl groups while those in green indicate methylenes.

Modeling studies concentrated on PDPPCBM to identify the most probable structures, the localization of HOMO and LUMO frontier orbitals and their energy levels, their UV-visible absorption profiles, and explore possible transfer of excited electronic states between DPP and PCBM moieties. The geometries of the ground state of DPP, PCBM and PDPPCBM molecules were performed in Orca 3.0.3²²¹ and optimized with the B3LYP/6-31G** level of theory.²²² To best estimate the most likely PDPPCBM isomer, the two DPP groups were added to the PCBM in succession choosing the highest LUMO densities as the target point for cycloaddition giving rise to the pyrrolidine group. Reference 223 gives full details of this procedure for a model system employing analogous comonomers adding to PCBM. UV-visible electronic transitions were calculated using these geometries but in the CAM-B3LYP function²²⁴ with the 6-31G** base.²²⁵ We find that the addition of the DPP to the PCBM structure considerably increases the oscillator strengths (i.e., absorbances) particularly in the principal transition in the same band, i.e., at 437.1 nm, 425.6 nm, 424.0 nm and 422.8 nm (2.837, 2.913, 2.924 and 2.932 eV) (Figure A2.8). These values are by no means definitive; they may shift considerably depending on environmental parameters, which we have not taken into account. The frontier orbitals were calculated to have the following energies: for DPP, $\langle H|E|H\rangle = -5.9219$ eV and $\langle L|E|L\rangle = -1.3734$ eV; for PCBM, $\langle H|E|H\rangle = -6.7372$ eV, and $\langle L|E|L\rangle = -2.1036$ eV. As shown in Figure 5.18, these frontier orbitals (HOMO-1 and HOMO) are both localized on the DPP, however, while the LUMO is on the PCBM, the LUMO+1 is delocalized across PCBM and DPP. Furthermore, these results suggest that a charge transfer is possible from an excited DPP state to PCBM; indeed one would expect an increase in the short circuit current (J_{sc}) on placing these materials in a photovoltaic device.

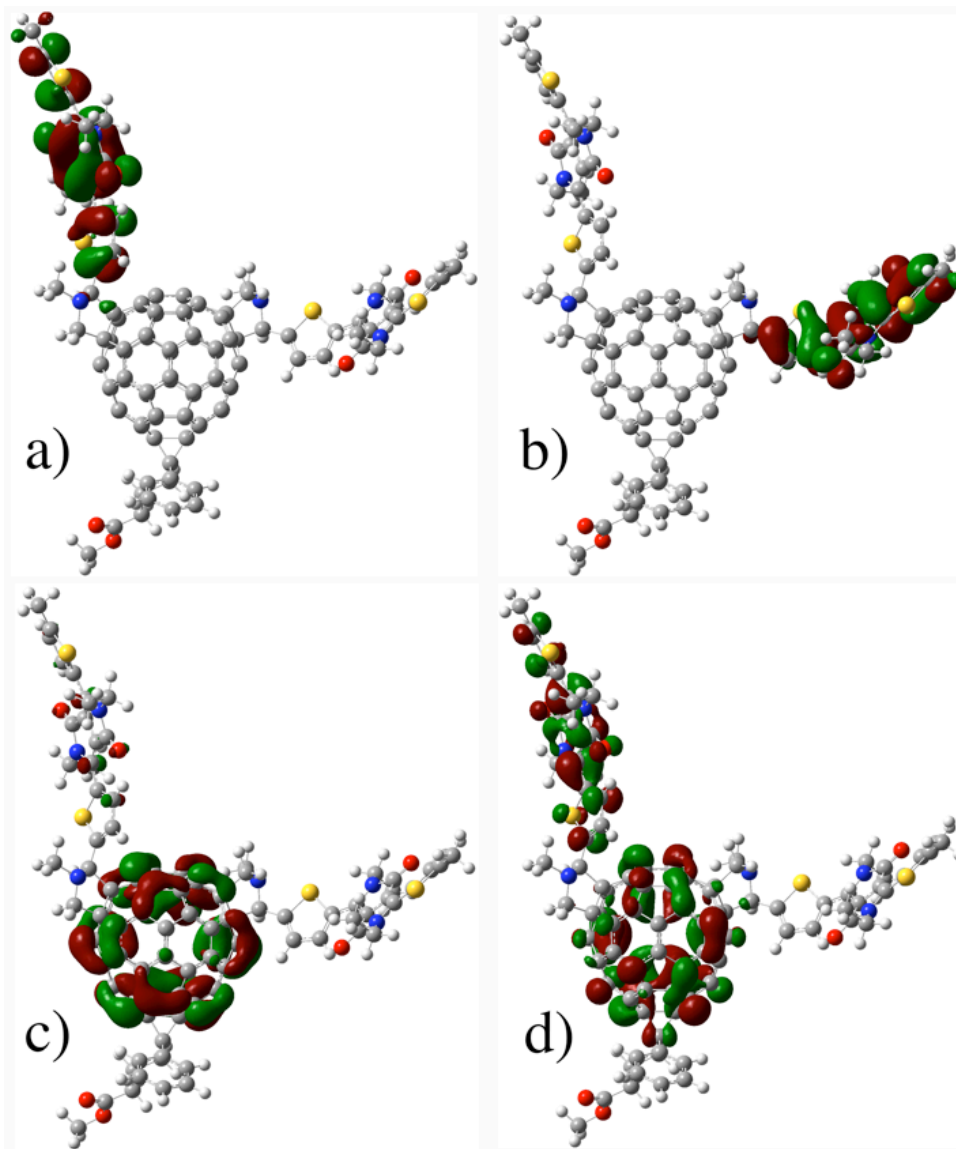


Figure 5.18. Most probable isomers formed by successive cycloadditions of DPP moieties to the PCBM fullerene sphere, showing the frontier orbitals for: a) HOMO-1; b) HOMO; c) LUMO; and d) LUMO+1.

The absorption spectra of solutions of same concentration for dodecyl-DPP (**2**), PDPF and PDPPCBM in toluene are shown in Figure 5.19. Extinction coefficients of the order of $10^4 \text{ M}^{-1}\text{cm}^{-1}$ (Figure A2.4) are observed for both macromolecules over a wide wavelength range of 300-650 nm. The spectra of the co-polymers clearly have contributions from absorptions of both comonomers. The strong absorption of C_{60} at 334 nm is reduced to a shoulder around same

wavelength in PDPF, while in PDPPCBM, no significant feature is observed in the region corresponding to PCBM's absorption at 330 nm. For both copolymers, a definite red shift of the order of 25 nm for PDPF and 22 nm for PDPPCBM in the absorption edge is observed, with respect to absorptions arising from the DPP (2) group. This suggests the presence of strong molecular orbital interactions between the fullerene and DPP moieties. That this possibility is occurring is also suggested by the emission studies shown in Figure 5.18. Here an efficient photoluminescence quenching of the DPP moiety by fullerene in both PDPF and PDPPCBM is found, indicative of energy or charge transfer from DPP to fullerene. An additional experiment was done by blending DPP (2) with C₆₀/PCBM in toluene solutions in 1:1 ratio. The total concentration of the solution was adjusted to have an absorbance of 0.1 O.D, similar to that in the aforementioned quenching experiment. Photo-luminescence measurements revealed no effective quenching of the emission of DPP moiety for the aforesaid concentration and loading of quencher (figure A2.5, appendix 2). This points out the benefit of covalently linking donor and acceptor moieties for facilitating energy/charge transfer.

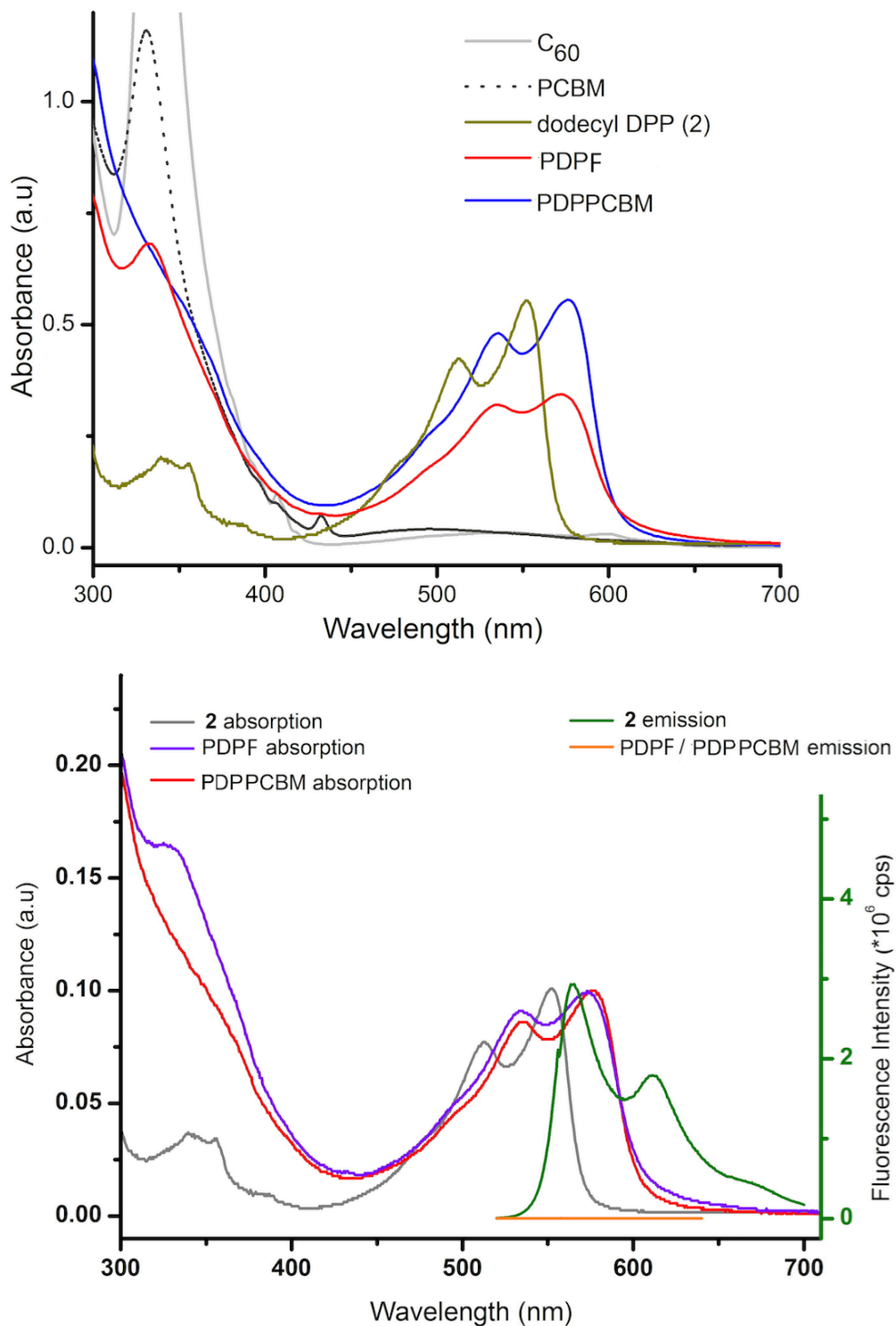


Figure 5.19 Absorption (above) and emission (below) spectra of PDPF, PDPPCBM, C_{60} , PCBM and **2** in toluene.

From Tauc's plot (figure A2.10, *appendix 2*), the optical band gap is calculated to be 1.90 eV for PDPF and 1.96 eV for PDPPCBM.

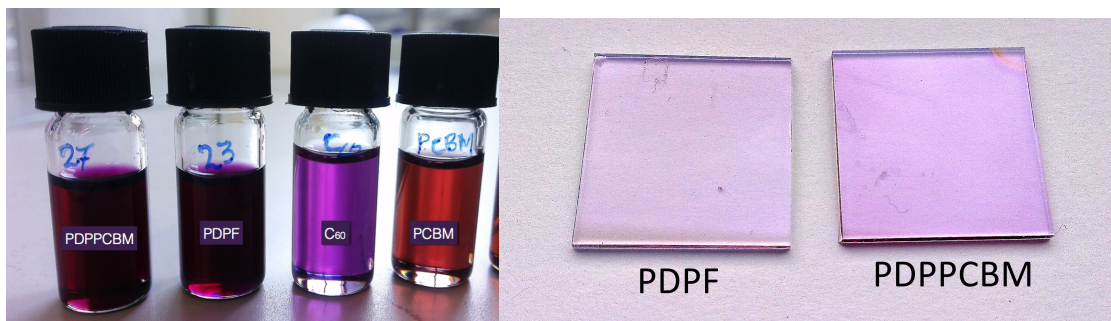


Figure 5.20 Solutions of PDPPCBM, PDPF, C₆₀ and PCBM in toluene; and thin films (~50 nm) of PDPF and PDPPCBM on ITO substrates.

Cyclic voltammetry measurements yielded values of $E_{\text{LUMO}} = -3.61$ eV for PDPF and $E_{\text{LUMO}} = -3.42$ eV for PDPPCBM. From Tauc's plots, the HOMO levels were then deduced as $E_{\text{HOMO}} = -5.51$ eV for PDPF and $E_{\text{HOMO}} = -5.38$ eV for PDPPCBM.

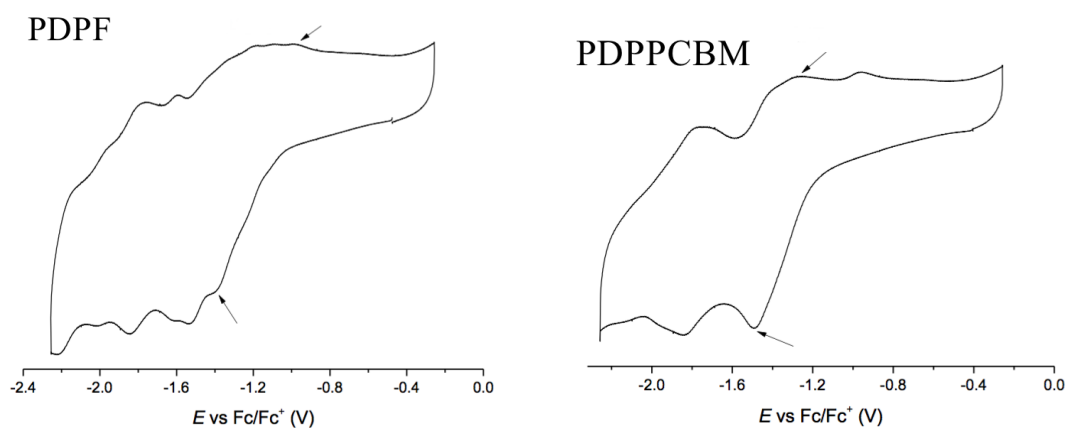


Figure 5.21 Cyclic Voltammogram of PDPF (left) and PDPPCBM.

Figure 5.22 shows a schematic of relative energy levels of the three different poly(pyrrolo-dino)fullerenes discussed in this chapter.

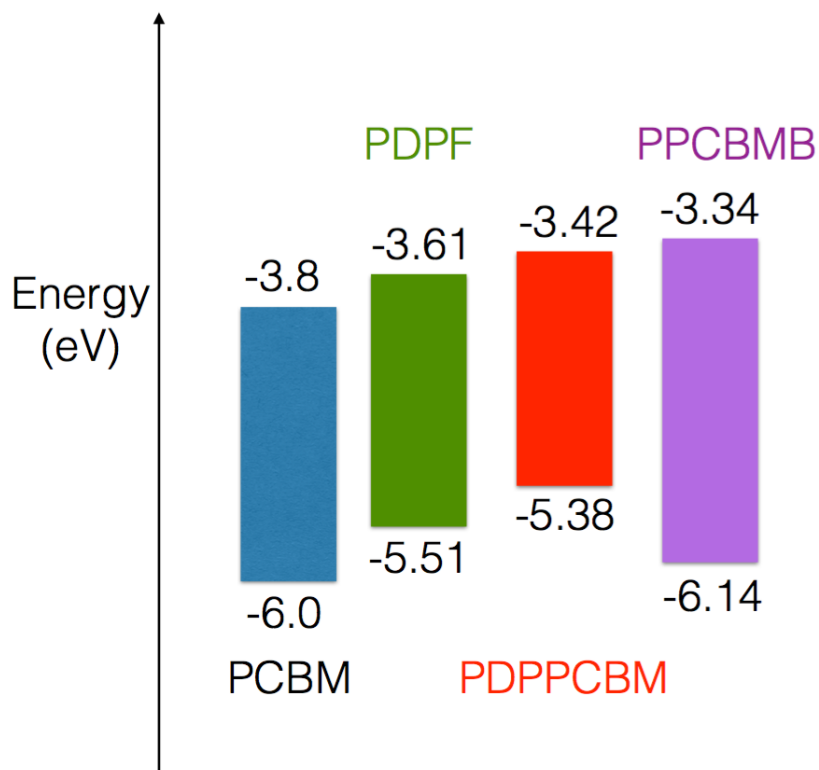


Figure 5.22 Energy levels of HOMO/LUMO for PDPF, PDPPCBM and PPCBMB relative to PCBM.

The nature of thermal decomposition of co-polymers were characterized by TGA (Figure 5.21). Both materials portray reasonable thermal stability up to 300 °C, the behavior being similar to the terephthalaldehyde-fullerene copolymer previously reported. A gradual weight loss accounting for up to 1% weight until 300 °C in PDPPCBM could be justified by residual solvent loss. The DSC thermograms of the copolymers in Figure A2.3, being smooth and featureless, would tend to indicate constrained structures given that one would expect T_g s arising from the side-chains. Further studies are required to elucidate the long-range structures of these materials.

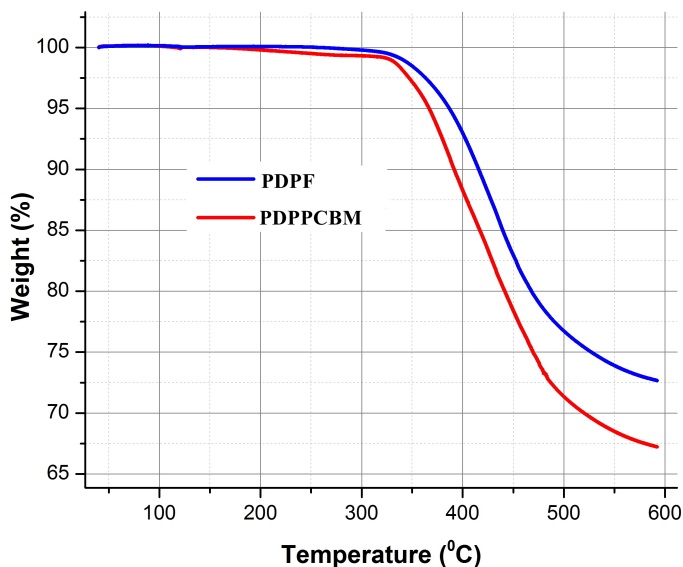


Figure 5.23. TGA thermograms of PDPF and PDPPCBM (N₂, 10 °C min⁻¹).

The photovoltaic properties of PPCBMB, PDPF and PDPPCBM are detailed in Chapter 6.

5.4 Conclusions

To sum, the wide scope of SACAP route in obtaining innovative main-chain poly(fullerene)s is demonstrated. The use of PCBM in place of C₆₀ leads to more soluble macromolecules in higher yields. The use of highly soluble co-monomers like terephthalaldehyde permits the formation of relatively pure high molecular weight poly(fullerene)s. The inclusion of large aromatic chromophores to yield alternating dye-fullerene oligomers and polymers is found to be feasible with the use of DPP as co-monomer in SACAP. The raised LUMO levels and high thermal stability of these novel materials make them promising for organic electronic applications.

Chapter 6

Photovoltaic properties and thermal stabilizing effects of poly(pyrrolidinofullerene)s

This chapter details the photovoltaic properties of organic solar cell devices incorporating poly(pyrrolidinofullerene)s discussed in chapter 5. Inverted solar cells devices were made with poly(pyrrolidinofullerene)s as acceptor and various donor polymers were explored to make up the active layer blends. The devices exhibited improved open circuit voltages, suggesting the raising of LUMO levels of poly(pyrrolidinofullerene)s with respect to PCBM. The best devices had PCEs of 0.9%, the reduction in short circuit currents being the main reason for the low efficiencies. When subjected to prolonged thermal stress, devices incorporating poly(pyrrolidinofullerene)s were found to be significantly more stable than control devices based on PCBM.

Device fabrication, photovoltaic characterization and PL quenching measurements described in this chapter have been carried out with Dr. Simon Dowland at Belectric OPV GmbH

The research leading to these results has received funding from the European Union Seventh Framework Program (FP7/2011) under grant agreement ESTABLIS no. 290022.

The three different poly-(pyrrolidinofullerene)s described in chapter 5 were tested for their potential use in photovoltaics by fabricating solar cell devices of inverted architecture and their power conversion efficiencies (PCE) were recorded under simulated sunlight (AM 1.5). Devices were fabricated in Belectric OPV GmbH, Nürnberg, during a short visit of four weeks. The fabrication procedure hence comprised of industrially relevant conditions. The active layer solutions were prepared in *o*-xylene and deposited via blade coating. All steps of fabrication were done in air, except the metal electrode, which was thermally evaporated in high vacuum (10^{-6} mbar) with a final active area of 25 mm². Even though these conditions are known to be non-optimal for best device performances, these were chosen inline with industrial requirements.²²⁶

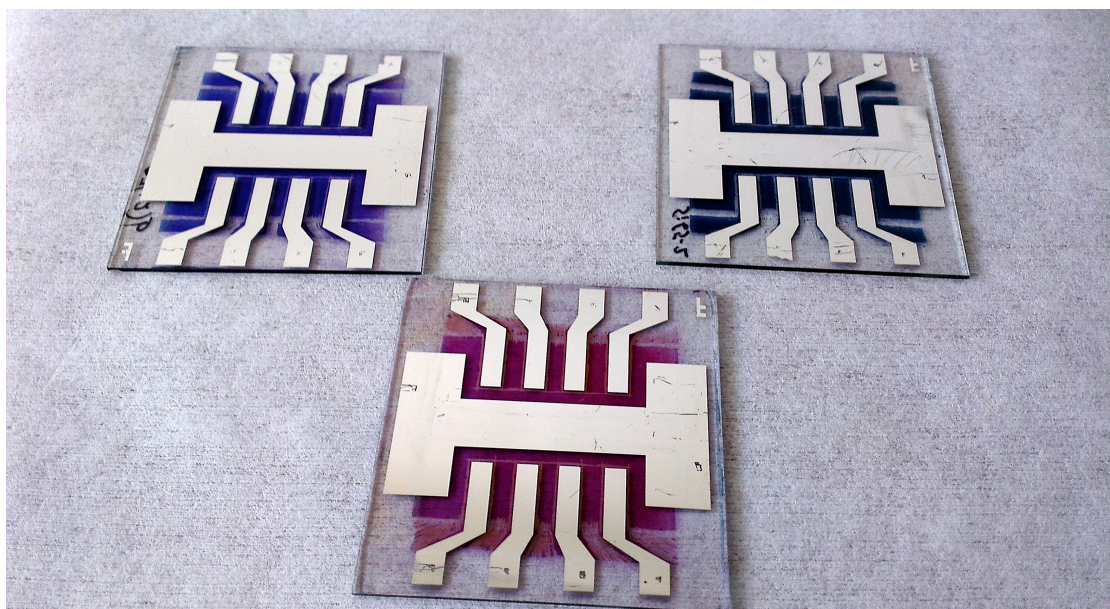


Figure 6.1. Image of fabricated devices incorporating poly-(pyrrolidinofullerene)s in active layer blends with KP115 (blue, far left) P3HT (red, centre) and Si-PCPDTBT (dark green, far right)

6.1 Device fabrication procedure

All devices discussed in this chapter were fabricated using the standard procedure give below:

ITO coated glass substrates were cleaned by sonication in acetone and isopropyl alcohol. ZnO was coated onto the clean substrates from a nanoparticle suspension (5 wt% in ethanol) and annealed at 140 °C in air. The initial solutions of donor and acceptor moieties in *o*-xylene were prepared by stirring at 80 °C overnight under air. The active layer was coated from a blend solution containing the required donor:acceptor ratio in *o*-xylene, followed by a layer of PEDOT:PSS (Heraeus) and subsequent annealing in nitrogen at 140 °C for 5 min. All aforementioned depositions were carried out with a doctor blade. The devices were completed by thermal evaporation of silver under high vacuum to produce cells with 27 mm² active area. The current voltage characteristics were measured under N₂ using a Keithley 2400 source meter and a Xenon arc lamp with an intensity of approximately 100 mWcm⁻².

6.2 P3HT:poly(fullerene) based devices

The poly(fullerene)s were first tested as acceptor in P3HT based solar cells. The active layer solutions were made up with a donor:acceptor ratio of 1:0.8, conforming with optimized conditions for P3HT:PCBM cells and stirred overnight at 85°C. Two sets of devices were made; one with addition of 1-methylnaphthalene (5% by volume) into the active layer and another without any additive.

As seen in Figure 6.2, the devices incorporating the additive were found to be slightly outperforming the ones without.

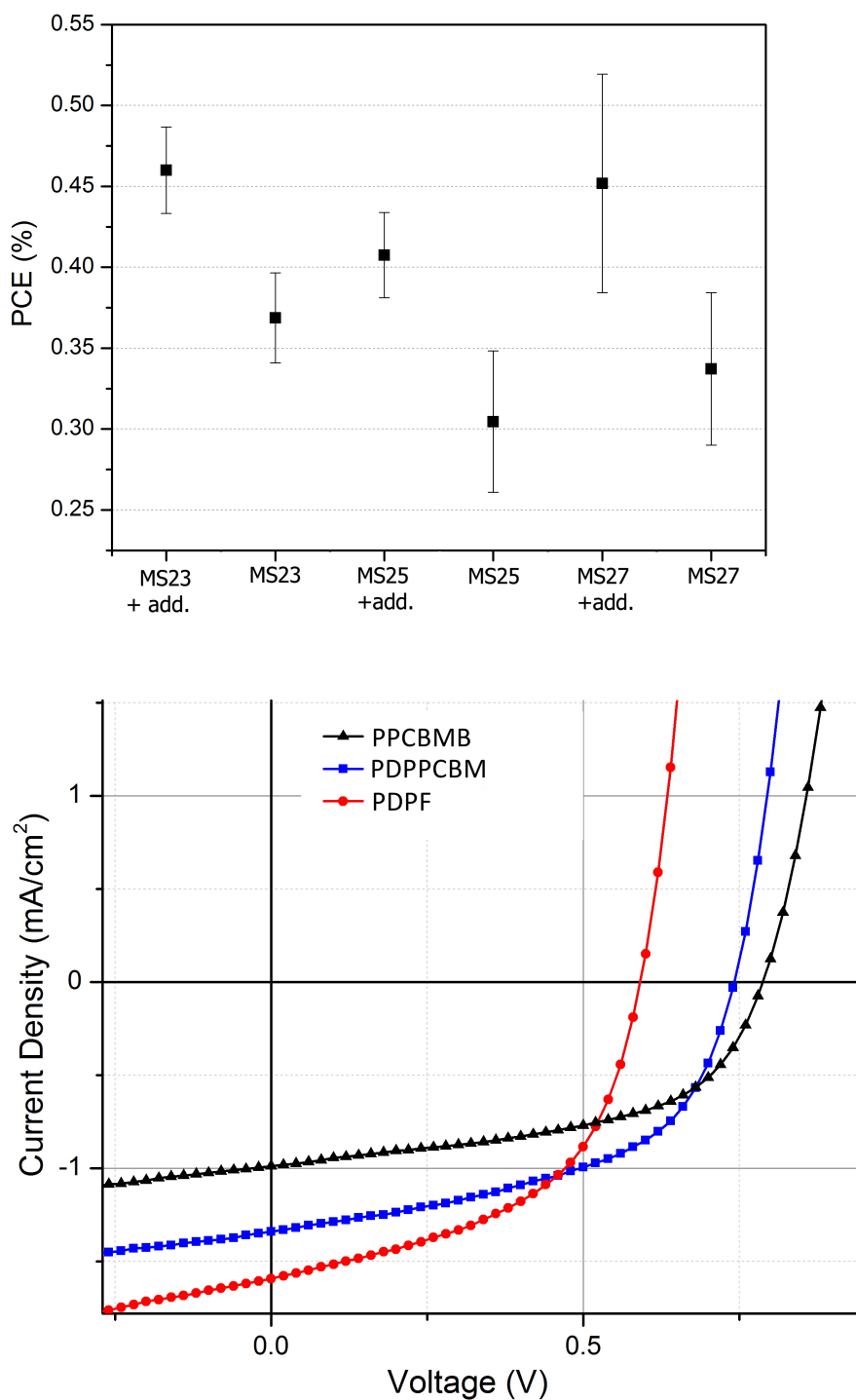


Figure 6.2. PCE of devices made with poly(fullerene)s as acceptors, (above) labeling: MS23-PDPF, MS25-PPCBMB, MS27-PDPPCBM; representative IV-characteristics of corresponding devices including methylnaphthalene as additive in the active layer in each case (below).

Table 2 summarizes the photovoltaic characteristics of devices incorporating poly(fullerene)s as acceptor and the control device made with PCBM, with 1-methylnaphthalene (5% by volume) added in the active layer in each case.

Table 2: Summary of photovoltaic characteristics of devices with additive.

	j_{sc} (mAcm ⁻²)	V_{oc} (V)	FF (%)	PCE (%)
PDPF	1.53 ± 0.055	0.62 ± 0.004	50 ± 2.8	0.46 ± 0.027
PDPPCBM	1.22 ± 0.086	0.77 ± 0.005	49 ± 4.2	0.45 ± 0.067
PPCBMB	0.98 ± 0.029	0.80 ± 0.003	51 ± 2.1	0.40 ± 0.026
PCBM (control)	9.22 ± 0.292	0.54 ± 0.002	63 ± 1.7	3.17 ± 0.030

A definite gain in V_{oc} is obtained with respect to PCBM for all three poly(fullerene)s studied, of the order of 80meV for PDPF and >200 meV for PDPPCBM and PPCBMB. It is notable that the gain in V_{oc} is higher for PCBM based polymers composed of tris-adducts, relative to the C₆₀ based polymer comprised of fullerene bis-adducts. These trends in V_{oc} arise as a result of raised LUMO levels with subsequent additions to the fullerene sphere, as evinced by cyclic voltammetry measurements detailed in Chapter 5. However, a decline in short circuit currents reduces the overall photovoltaic efficiency of devices incorporating these poly(fullerene)s as acceptor moieties, with the experimental conditions mentioned herein.

The occurrence of photo-induced charge transfer from P3HT to poly(fullerene)s is proved by the quenching of photoluminescence (PL) of P3HT. PL quenching was calculated relative to the emission of a pristine P3HT film and corrected for the absorption of the films (figure 6.3). The quenching efficiency increases with increase in loading of poly(fullerene)s and significant quenching is observed only at high loading of poly(fullerene)s in the film. This suggests that the interfacial area between P3HT and poly(fullerene)s in the blend films with acceptor ratios normally employed in photovoltaic devices is not optimal for

efficient exciton quenching, indicative of a non-percolative nature of the two components in the blend matrix.

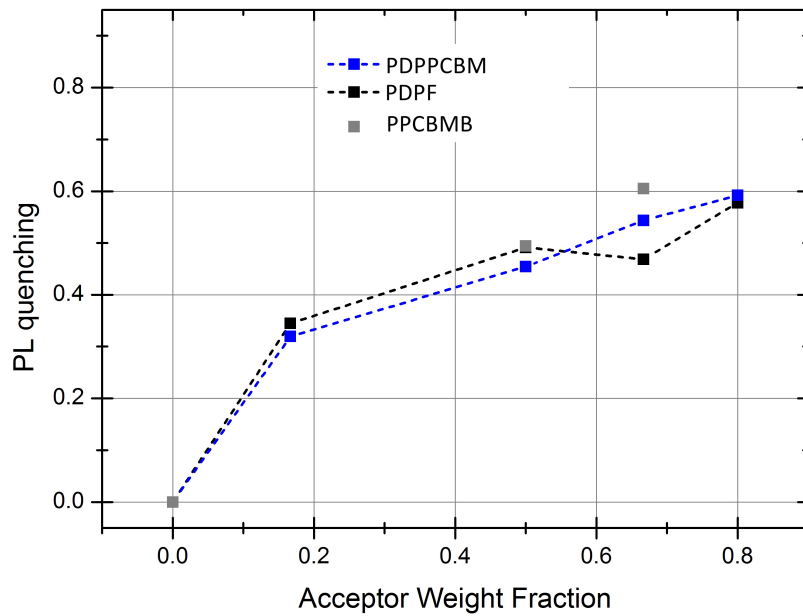


Figure 6.3. PL quenching of P3HT with increasing poly(fullerene) loading, at an excitation wavelength of 450 nm

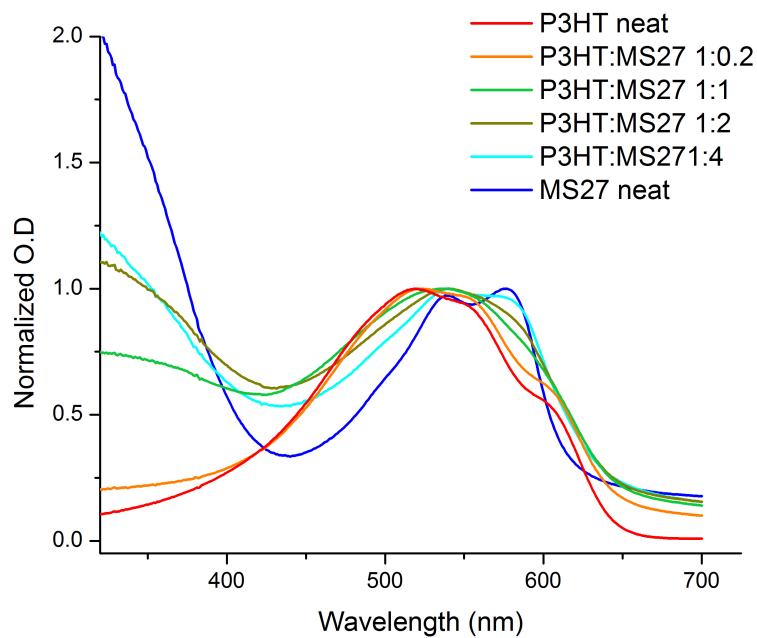


Figure 6.4. Normalised absorption profiles of P3HT:PDPPCBM blends ; labeling MS27 - PDPPCBM

Figure 6.4 shows the U.V-visible absorption spectra recorded for P3HT:PDPPCBM films with different weight ratios of the two components. The vibronic shoulder at 600 nm observed in neat P3HT almost completely disappears with a poly(fullerene) loading of 50% (ratio of 1:1). This characteristic feature of regio-regular P3HT's absorption is reported to be arising from inter-chain interactions and is highly sensitive of its crystallinity.²²⁷ The significant reduction of this feature in blends with relevant acceptor weight loading is indicative of a more amorphous nature of blend brought about by the addition of poly(fullerene).

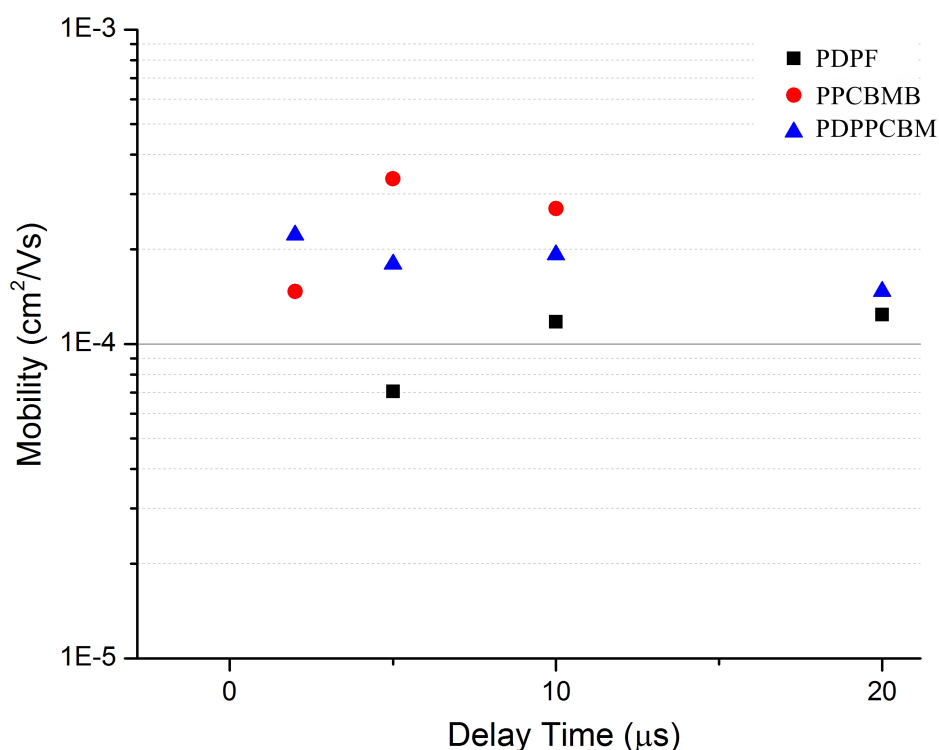


Figure 6.5. Photo-CELIV mobility of P3HT:poly(fullerene) (1:0.8) devices.

Photo-CELIV measurements on the aforementioned devices based on P3HT:poly(fullerene) with 1:0.8 ratio of donor:acceptor afforded mobilities of order of 1×10^{-4} cm²/Vs (figure 6.5), the values being comparable to those obtained from P3HT:PC₆₁BM systems fabricated in a similar manner, as presented in Chapter 3.

6.3 Exploring more donor systems

Further, more experiments were done with low-band gap donor polymers Si-PCPD₂TBT and KP-115, with structures shown in figure 6.6. Devices were made with PDPF as acceptor, varying the donor polymer. The blade temperature was also varied through different sets of devices to optimize the blade coating procedure.

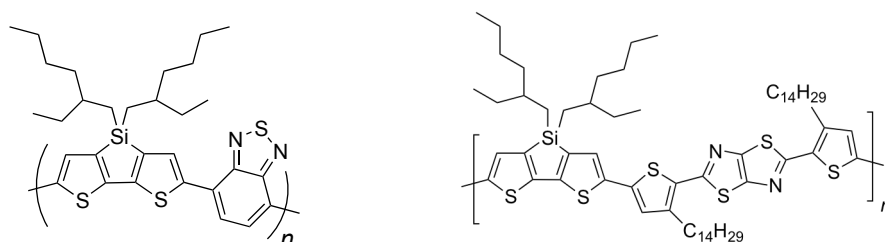


Figure 6.6. Structure of Si-PCPD₂TBT (left) and KP115 (right)

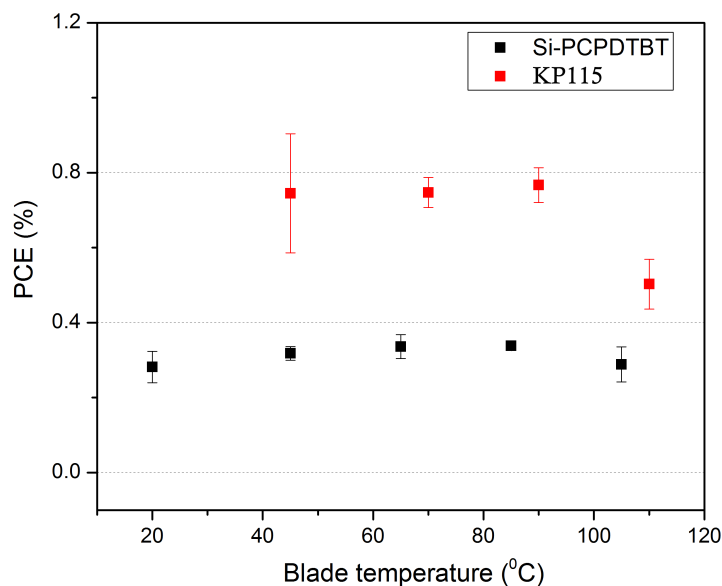


Figure 6.7. Variation of PCEs obtained for devices made with PDPF as acceptor in blends with KP115 and Si-PCPD₂TBT, the active layer being coated at different blade temperatures.

The donor: acceptor ratios were kept the same as optimized conditions with PCBM for each donor polymer, *i.e.*, (1:2) for both KP115 and Si-PCPDTBT with respect to PDPF. KP115 is particularly interesting for industrial applications owing to the relatively high thicknesses (>200 nm) of the active layer that can be used without detrimental effects on efficiency.²²⁸ The power conversion efficiencies are found to be highest for KP115 based devices, while using PDPF as an acceptor (figure 6.7). The improved PCEs mainly originate from increased short circuit currents obtained from KP115 based devices. During the device fabrication, the blend films made from KP115 appeared smoother to the naked eye, which was also reflected in the smoothness of Ag layer deposited. Hence the observed increase in extracted currents is likely to be linked to a more favorable morphology formed in thin films of KP115 blends with respect to other donor polymers explored.

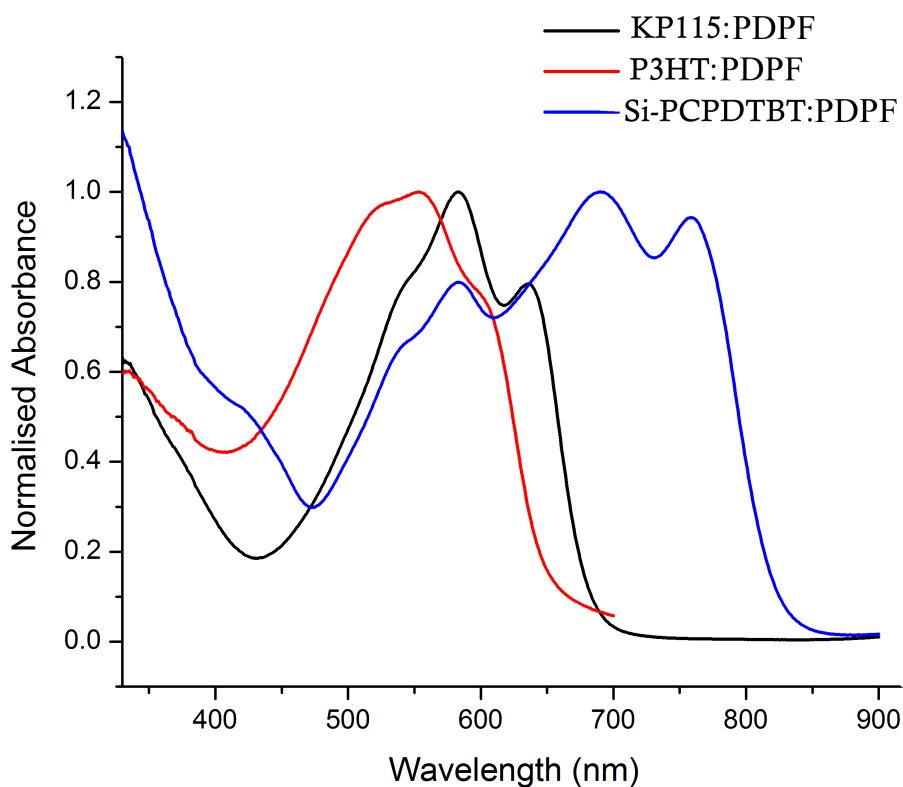


Figure 6.8. Absorbance of active layer films of devices incorporating KP115, P3HT and Si-PCPDTBT, respectively as donors, with PDPF as acceptor.

Owing to the relatively better performances of KP115 based devices, further experiments were done with blends comprised of KP115 as donor and PDPPCBM as acceptor. Figure 6.9 shows the representative current-voltage characteristics of KP115 based devices, with PDPF and PDPPCBM as acceptors, respectively. Both short circuit current and open circuit voltages obtained are higher for KP115:poly(fullerene) based devices, in comparison to P3HT:poly(fullerene) based ones, which is reflected in their PCEs. KP115 reportedly has lower lying HOMO levels with respect to P3HT, affording higher open circuit voltages.²²⁸

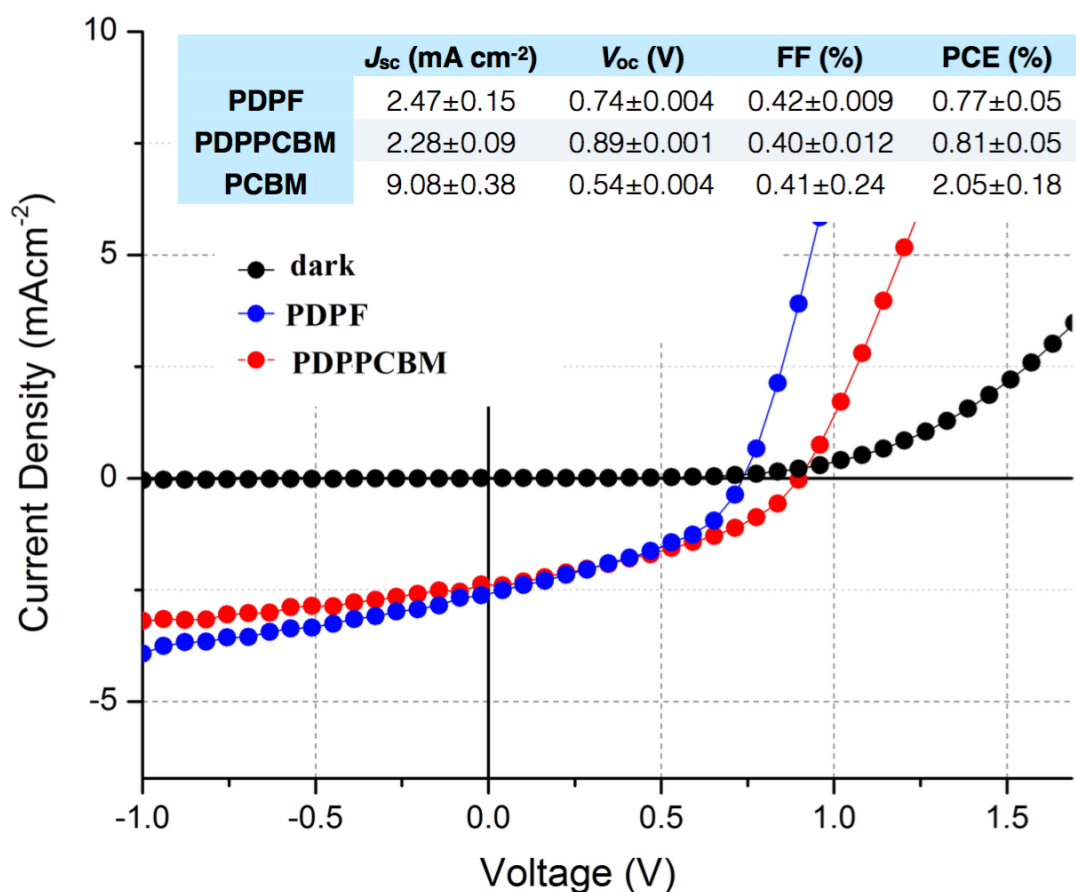


Figure 6.9 Representative current voltage characteristics of KP115:PDPPCBM (red) and KP115:PDPF (blue) devices, with a donor:acceptor ratio of 1:2, values being an average of 16 cells.

Keeping the optimized blade temperatures, the donor-acceptor ratio was then varied across different sets of devices with KP115:PDPPCBM active layer. Another set of devices were made with ternary blends of KP115, PDPPCBM and PCBM with varying PDPPCBM:PCBM ratio, keeping the overall donor:acceptor ratio constant, at 1:2. From figure 6.10, it can be seen that devices with 60% weight fraction of PDPPCBM is optimal for KP115:PDPPCBM based devices with an average PCE of 0.8%. For ternary devices consisting of KP115, PCBM and PDPPCBM, the PCEs are found to be decreasing with increasing content of PDPPCBM. The lowest content of PDPPCBM in the studied ternary blends was 20% (with respect to PCBM). The control devices (KP115:PCBM) yielded average PCEs of 2.0%.

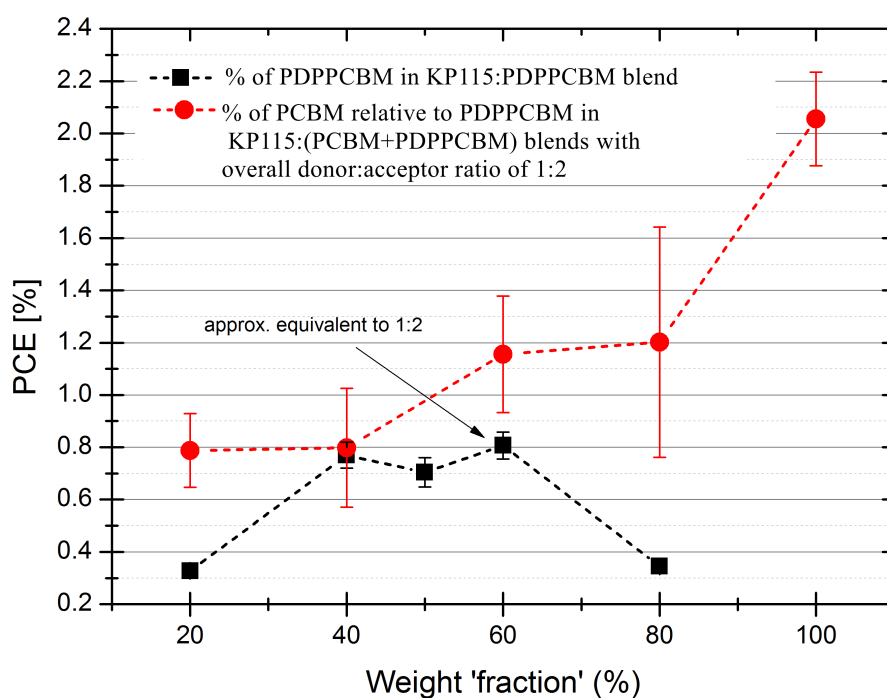


Figure 6.10. PCEs of devices with different weight ratios of donor and acceptor in KP115:PDPPCBM blends (black squares) and PCEs of devices based on KP115:(PCBM+PDPPCBM) blends, with varying weight ratio of PCBM and PDPPCBM (red circles), data being an average of 16 cells.

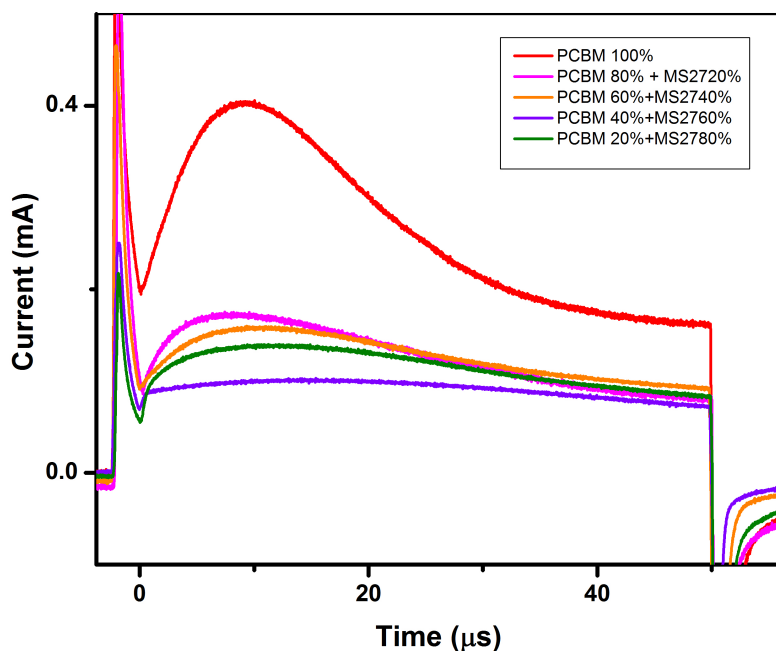
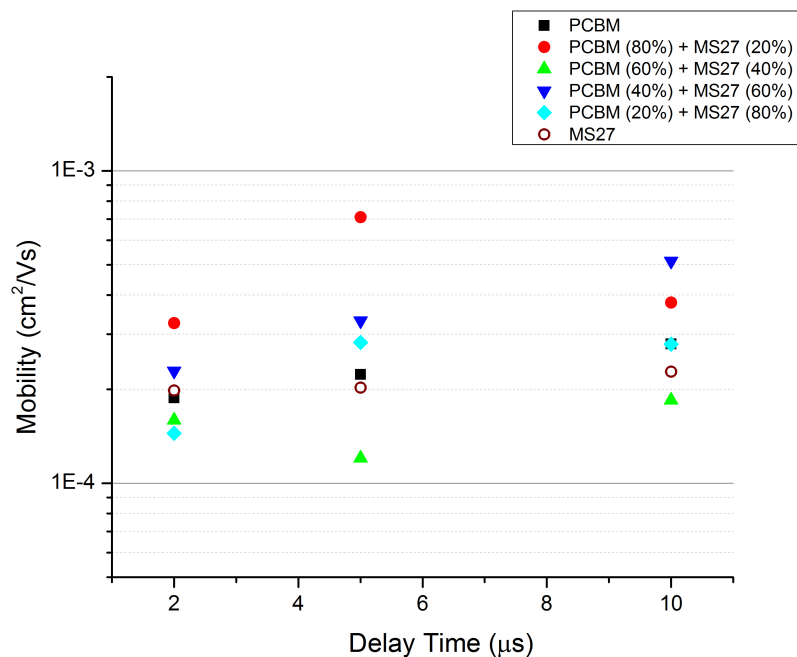


Figure 6.11. Photo-CELIV mobilities obtained for devices consisting of varying amounts of PDPPCBM loading with respect to PCBM, keeping a constant donor:acceptor ratio of 1:2 with respect to the donor polymer KP115 (above) ; photo-CELIV transients recorded for the corresponding devices at similar light intensities and delay time of 2 μs (below) ; labeling : MS27 = PDPPCBM

Photo-CELIV measurements on the aforementioned devices based on KP115: (PCBM+PDPPCBM) blends were carried out to comprehend possible effects on charge transport brought about by the addition of PDPPCBM into the blend matrix. As stated before, the composition of PDPPCBM was varied across samples while the overall donor:acceptor ratio was kept constant at 1:2 with respect to KP115. From figure 6.11, it is apparent that the average mobility of the blend is not significantly affected by increasing loading of PDPPCBM into the KP115:PCBM blend. A more evident change observed is perhaps in the conductivity current of the recorded transients for same input light intensities and delay times. Since the amplitude of the transient can be directly related to the extractable carrier density, this suggests the presence of a severe loss mechanism in place with as low as 20% by weight loading of PDPPCBM. Tracing the origin of the apparent reduction in extractable free charges demands extensive studies since it could be related to one or combination of several events from charge separation to extraction occurring at different timescales.

6.4 Thermal Stability Studies

The aforementioned devices were then subjected to thermal stress at 120°C up to 100 h. Data points were frequently collected during the initial times (15 minutes to start with), the intervals being increased at longer times, to record the so-called “burn-in” phase on exposure to thermal stress, where the cells degrade rapidly during the first few hours, followed by a more stable phase.²²⁹ Figure 6.12 shows the evolution of PCE for devices consisting of ternary blends of KP115, PDPPCBM and PCBM with varying weight percents of PDPPCBM loading.

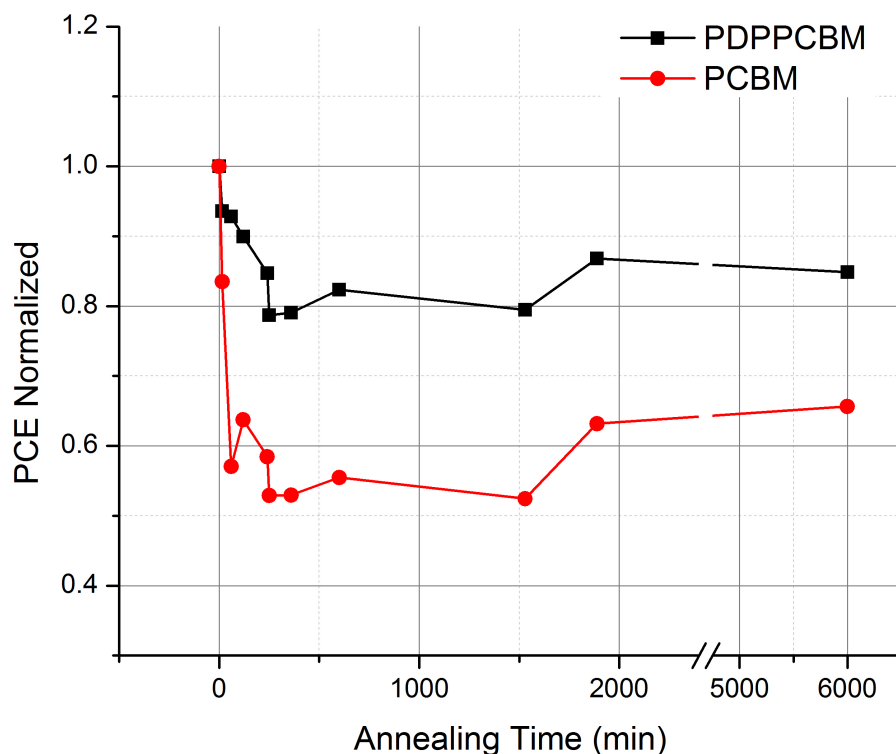
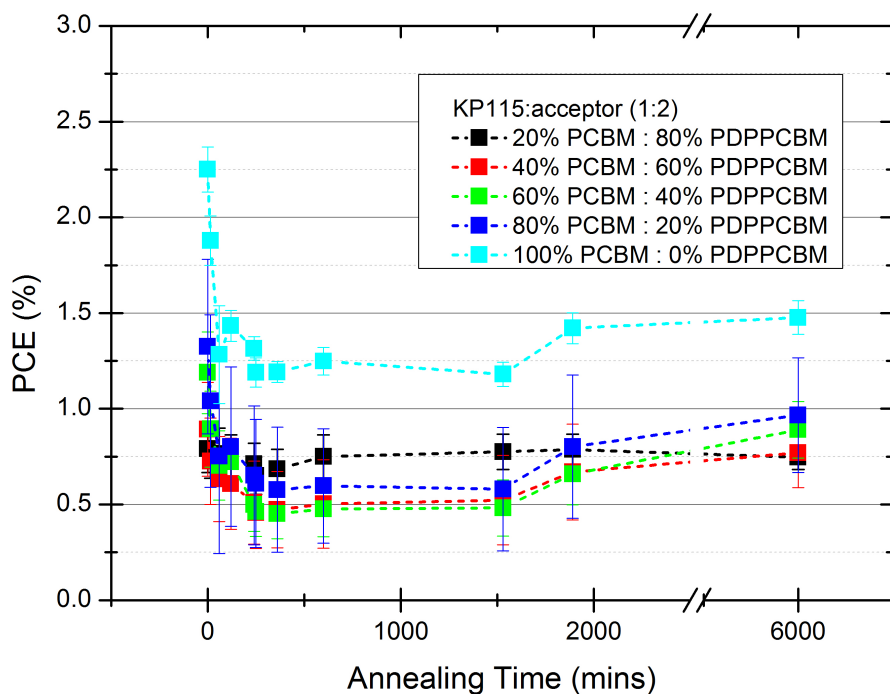


Figure 6.12. Evolution of PCE for devices consisting of PCBM+PDPPCBM as acceptor, with varying amounts of PDPPCBM loading, keeping KP115 as donor and a donor:acceptor ratio of 1:2, data being an average of eight cells. (above); Normalized PCEs of devices consisting of KP115 as donor and PDPPCBM and PCBM, respectively, as acceptor during thermal degradation (below).

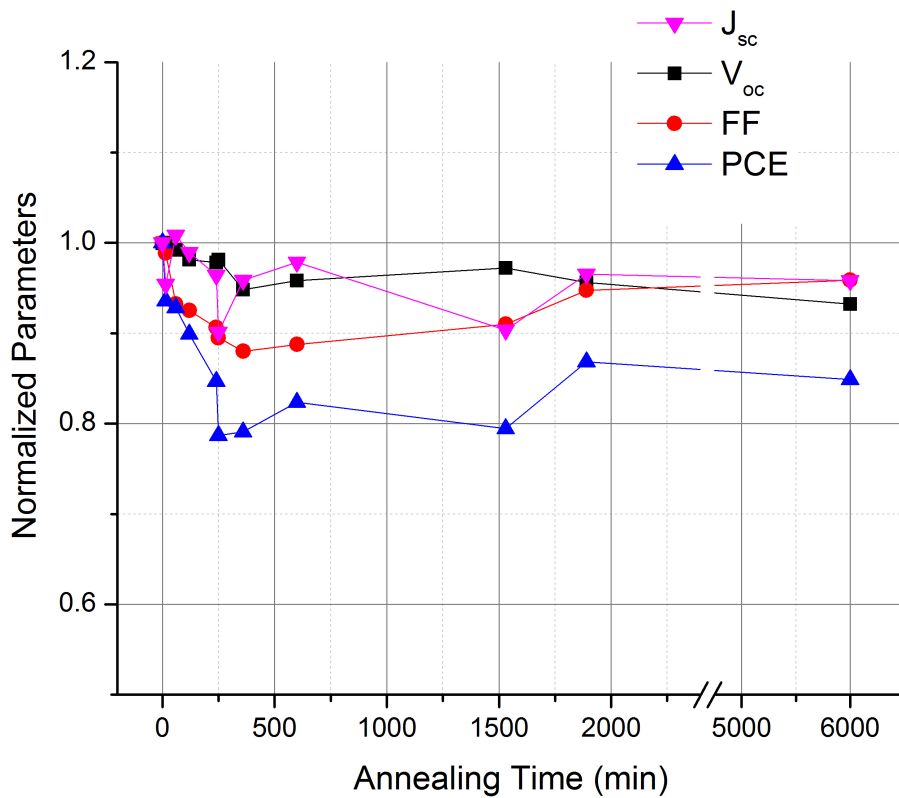
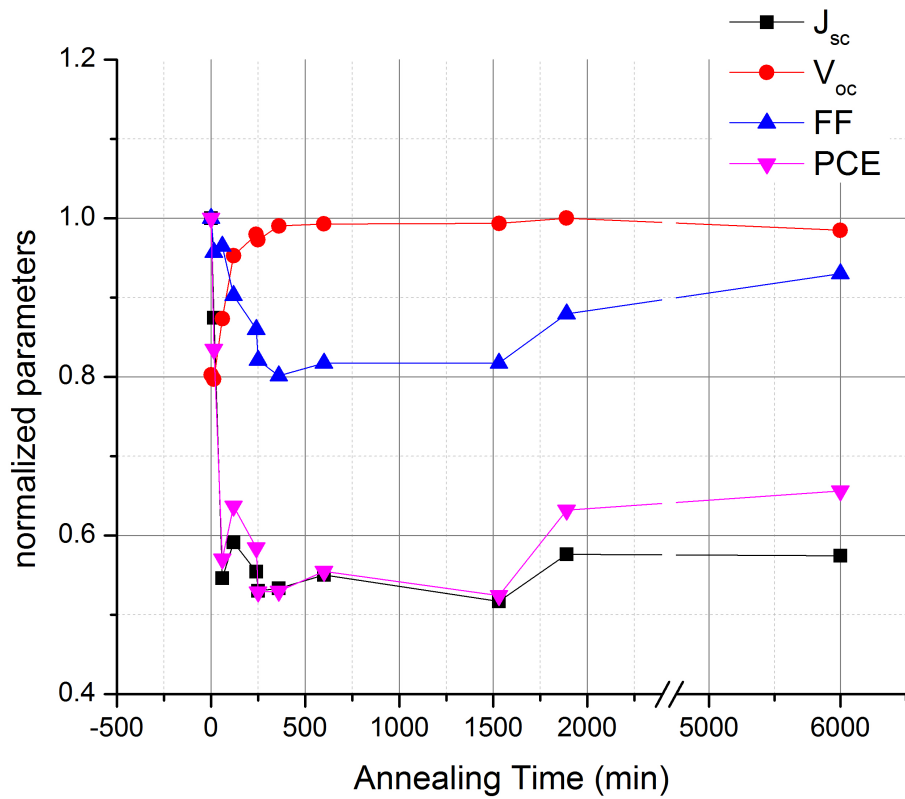


Figure 6.13. Evolution of photovoltaic characteristics of devices based on KP115:PCBM (above) and KP115:PDPPCBM (below), on exposure to thermal stress.

From figure 6.12, it is evident that devices containing a higher loading of PDPPCBM exhibit higher stability to thermal stress. Normalizing the PCEs allows us to have a clearer picture of the evolution of PCE, as shown in figure 6.13. Here the data points correspond to PCEs of devices consisting of KP115:PCBM (1:2) and KP115:PDPPCBM (1:1.5) as active layer, fabricated in similar conditions.

The decline of J_{sc} appears to be the main factor driving the degradation in control devices, which is slowed down in PDPPCBM containing systems affording their improved stabilities (figure 6.14). The potential use of PDPPCBM as a stabilizer in active layer of organic solar cells is evident from these experiments. Identifying an optimal blend of PCBM and PDPPCBM to achieve stable devices without sacrificing much on the efficiency is the key. This concept was not explored further during the time of this thesis due to time limitations, but stays prospective for future studies.

6.5 Conclusions

Three different poly(fullerene)s synthesized during this thesis were tested for their photovoltaic performance as acceptors in blends with three different conventional donor polymers P3HT, Si-PCPDTBT and KP115. The resulting devices afforded highest PCEs when blended with KP115 compared to other two systems. The intermixing of the donor and acceptor systems when a small molecule like PCBM is replaced with a polymer, is discerned to be non-optimal for charge transfer, from photo-luminescence quenching studies. The donor polymer : poly(fullerene) blends possessed reasonable charge carrier mobilities from photo-CELIV measurements. Thus the rather low efficiencies of devices incorporating poly(fullerene)s in the active layer is most likely related to large scale phase separation of donor-acceptor moieties, which is reported as a common problem with many polymer:polymer BHJs.²² However, more studies on controlling the morphology of these blends needs to be carried out to unlock their full potential. It is also noted that all the donor polymers tested herein are known to form

crystalline domains in their thin films. Employing rather amorphous donor polymers may result in a higher miscibility of the distinct donor and acceptor polymers and is a concept worth exploring. Although the use of poly(fullerene)s reduced the extracted current densities with respect to control devices made with PC₆₁BM, thermal degradation studies revealed potential stabilizing effects of poly(fullerene)s in the blend. Choosing an ideal weight ratio of PCBM:poly(fullerene), where the weight percent of poly(fullerene) fits the notion of an additive is expected to allow for formation of stable blends without compromising on efficiency.

Summary

This thesis dealt with documenting the charge transport features during degradation in organic solar cells in the former part and detailed the synthesis and characterization of novel poly(fullerene)s in the latter part.

Current transients were recorded and analyzed during the process of photo-degradation of functional solar cell devices using photo-CELIV and TOF techniques. Extraction current transients of the benchmark P3HT:PCBM revealed a slight reduction in average mobility of the blend and evidently an increased number of trapped carriers with progressive degradation. Integral TOF measurements at high light intensities evinced the increase in Langevin recombination factor (β / β_L) with degradation, indicating the enhanced possibility of recombination when the regime is strictly bimolecular. This hints at the disruption of ideal nanomorphology which is reported to be linked to the highly reduced Langevin recombination in pristine P3HT:PCBM blends.

Similar experiments were carried out on a series of benzodithiophene – diketopyrrolopyrrole polymers in an effort to understand the role of side-chain and molecular order on the photo-stability of finished devices. The evolution of charge transport properties of encapsulated devices on exposure to simulated sunlight was documented and analysed using photo-CELIV and TOF techniques. The results indicated the increase in deep-trapped carriers to be the most dominant factor determining charge transport properties of the blend on a macroscopic time scale. An understanding of the distinct effects of side-chain variation and subsequent morphological changes on charge transport properties was not possible solely from these measurements, which calls for complementary studies to quantify the density of trap states.

Furthermore, the Sterically controlled Azomethine ylide Cycloaddition Polymerization (SACAP) is explored to synthesize main-chain alternating

poly(fullerene)s in one-pot, metal-free conditions. The use of terephthalaldehyde and PCBM in SACAP permitted the formation of soluble poly(fullerene)s with probable molecular weights of $M_n \geq 24\,600 \text{ g mol}^{-1}$, as discerned from THF GPC and easy handling. Moreover, the first examples of polymers and oligomers consisting of alternating dye and fullerene units were demonstrated by the use of DPP as co-monomer in SACAP route. Use of PCBM in place of C_{60} permits higher solubilities and greater ease in handling and purification. Even though the *cis*-isomers are most likely to be excluded, the identification of regioisomers requires extensive studies using model molecules.

When used in photovoltaic devices, high V_{oc} s are found arising from the modification of the C_{60} sphere. However the reduced short circuit currents resulted in lower efficiencies of poly(fullerene) containing devices relative to PCBM. Photo-CELIV studies indicated the active layer blends to possess reasonable charge mobilities ($1 \times 10^{-4} \text{ cm}^2/\text{Vs}$) and thus the reduced short circuit currents are likely arising from morphological effects, as suggested by photo-luminescence quenching studies. The donor and acceptor polymers are probably forming large phase separated domains in the BHJ, which is undesirable for charge transfer and transport. Nevertheless considering these are only preliminary results, there is plenty of room for device optimization in terms of solvent, processing conditions etc. More importantly, the devices made with poly(fullerene)s demonstrated enhanced thermal stabilities relative to PCBM, with burn-in effects greatly reduced.

Future studies calls for probing charge transport and recombination, and understanding the evolution of nano and meso-morphologies of these new materials in bulk heterojunctions.

Appendix 1

Synthetic Routes

PPCBMB

2,5-Bis(octyloxy)terephthalaldehyde (0.21 g, 0.55 mmol), PC₆₀BM (0.50 g, 0.55 mmol) and *N*-methylglycine (0.10 g, 1.11 mmol) were dissolved in degassed 1,2-dichlorobenzene (20 mL) and stirred at 150 °C for 18 h, then poured into methanol (250 mL). The precipitate was recovered by filtration directly into a Soxhlet thimble, acetone washed for four days, and recovered as a shiny black powder. Yield: 75% (0.48 g). GPC: $M_w = 23000 \text{ g mol}^{-1}$; $M_n = 7500 \text{ g mol}^{-1}$; $D = 3.00$ (THF, 30 °C, 330 nm).

NMR: ¹H NMR (400.6 MHz, CDCl₃) $\delta = 10.46$ (broad, -COH), 8.26 – 6.84 (broad, *aromatics*), 5.41-4.62 (broad, -CH-N-, -CH₂-N-), 4.18 – 3.41 (broad, -OCH₂(CH₂)₆CH₃, -COOCH₃), 2.82-2.17 (broad, -CH₃-N-, -(CH₂)₃COOCH₃), 1.68-1.07 (broad, -OCH₂(CH₂)₆CH₃), 0.93 (broad, -OCH₂(CH₂)₆CH₃) ppm. ¹³C NMR (100.16 MHz, CDCl₃) $\delta = 173.52$ (s, -COOCH₃), 152.07-113.89 (m, *aromatics*), 69.19 (m, -CH₂-N-, O-CH₂(CH₂)₆CH₃), 51.58 (s, -COOCH₃) 40.14 (s, -CH₃-N-), 34.11-31.93 (m, -(CH₂)₃COOCH₃), 29.38-22.17 (m, -OCH₂(CH₂)₆CH₃), 14.22 (s, -OCH₂(CH₂)₆CH₃) ppm.

2D-HSQC NMR (CDCl₃), $d = \delta = 7.44, 128.03$ (*aromatics*); 5.41, 76.70 (-CH-N-); 4.81-3.87, 69.19 (-CH₂-N-, -OCH₂(CH₂)₆CH₃); 3.62, 51.58 (-COOCH₃); 2.80-2.61, 40.14 (-CH₃-N-); 2.63-2.28, 34.11-33.84 (-(CH₂)₃COOCH₃); 1.68-0.99, 31.90-22.17 (-OCH₂(CH₂)₆CH₃); 0.93, 14.22 (OCH₂(CH₂)₆CH₃) ppm.

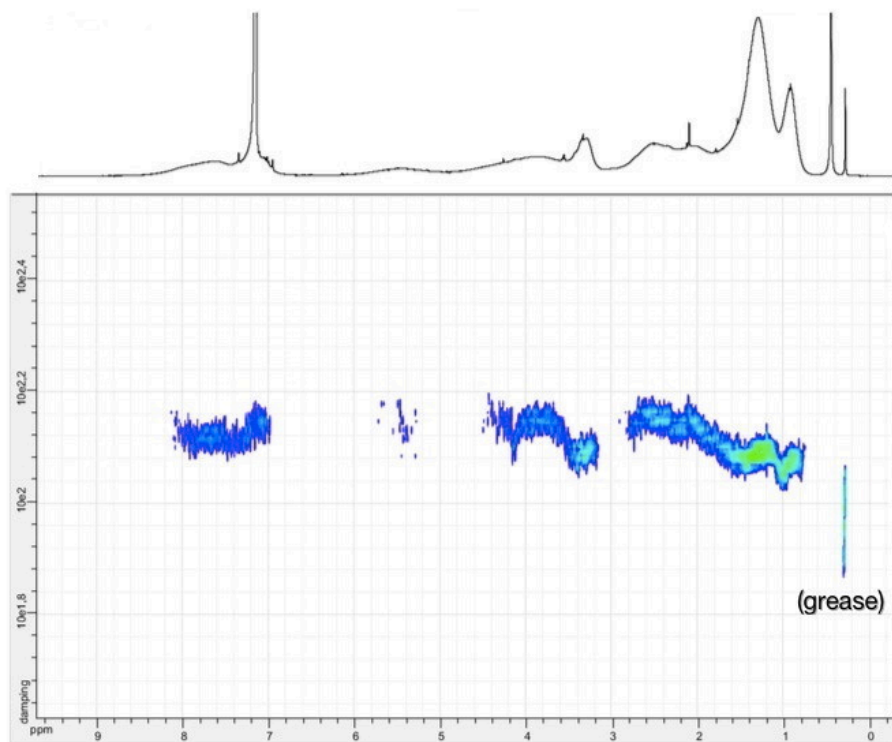
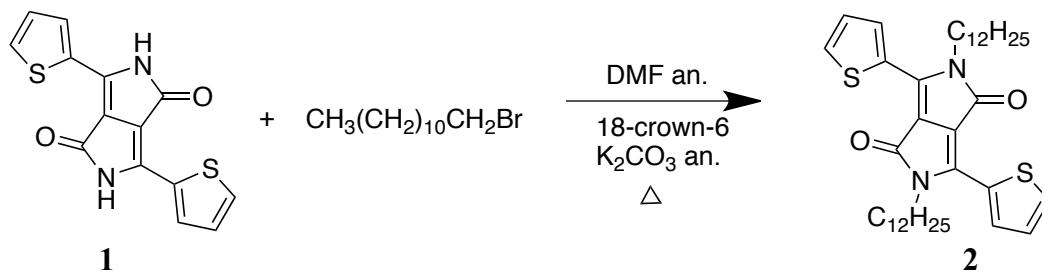


Figure A1.1. DOSY 2-D ^1H NMR (C_6D_6 , ambient temperature) of PPCBMB. Note the impurity due to grease at 0.1 ppm.

2,5-bis(dodecyl)-3,6-di(thiophen-2-yl)pyrrolo[3,4-*c*]pyrrole-1,4-dione (**2**)

3,6-Di(thiophen-2-yl)pyrrolo[3,4-*c*]pyrrole-1,4(2,5)-dione (**1**, 1.06 g, 3.53 mmol), 1-bromododecane (2.60 g, 10.50 mmol) and anhydrous K_2CO_3 (1.71 g, 12.25 mmol) were dissolved in anhydrous DMF (16 mL). Catalytic amount of 18-crown-6 was added and the mixture was stirred at 120 °C overnight. The reaction mixture was allowed to cool to room temperature, filtered on Buchner and washed several times with water and methanol. Yield: 1.03 g (47%).



Scheme A1.1 Synthetic route to **2**.

1H NMR (400 MHz, $CDCl_3$) δ = 8.92 (dd, J = 1.2 Hz, 2H, Ar-*H*), 7.64 (dd, J = 1.2 Hz, 2H, Ar-*H*), 7.28 (convoluted with solvent peak, 2H, Ar-*H*), 4.07 (t, J = 8 Hz, 2H, $-CH_2(CH_2)_{10}CH_3$), 1.73-1.25 (m, 10H, $-CH_2(CH_2)_{10}CH_3$), 0.88 (t, J = 7.2 Hz, 3H, $-CH_2(CH_2)_{10}CH_3$) ppm.

^{13}C NMR, (100 MHz, $CDCl_3$): δ = 161.71 (s, Ar-CO), 140.35 (s, Ar-C), 135.57 (s, Ar-C), 130.98-128.93 (s, Ar-C), 108.18 (s, Ar-C), 42.56 (s, $-CH_2(CH_2)_{10}CH_3$), 32.23-23.01 (s, $-CH_2(CH_2)_{10}CH_3$), 14.44 (s, $-CH_2(CH_2)_{10}CH_3$) ppm.

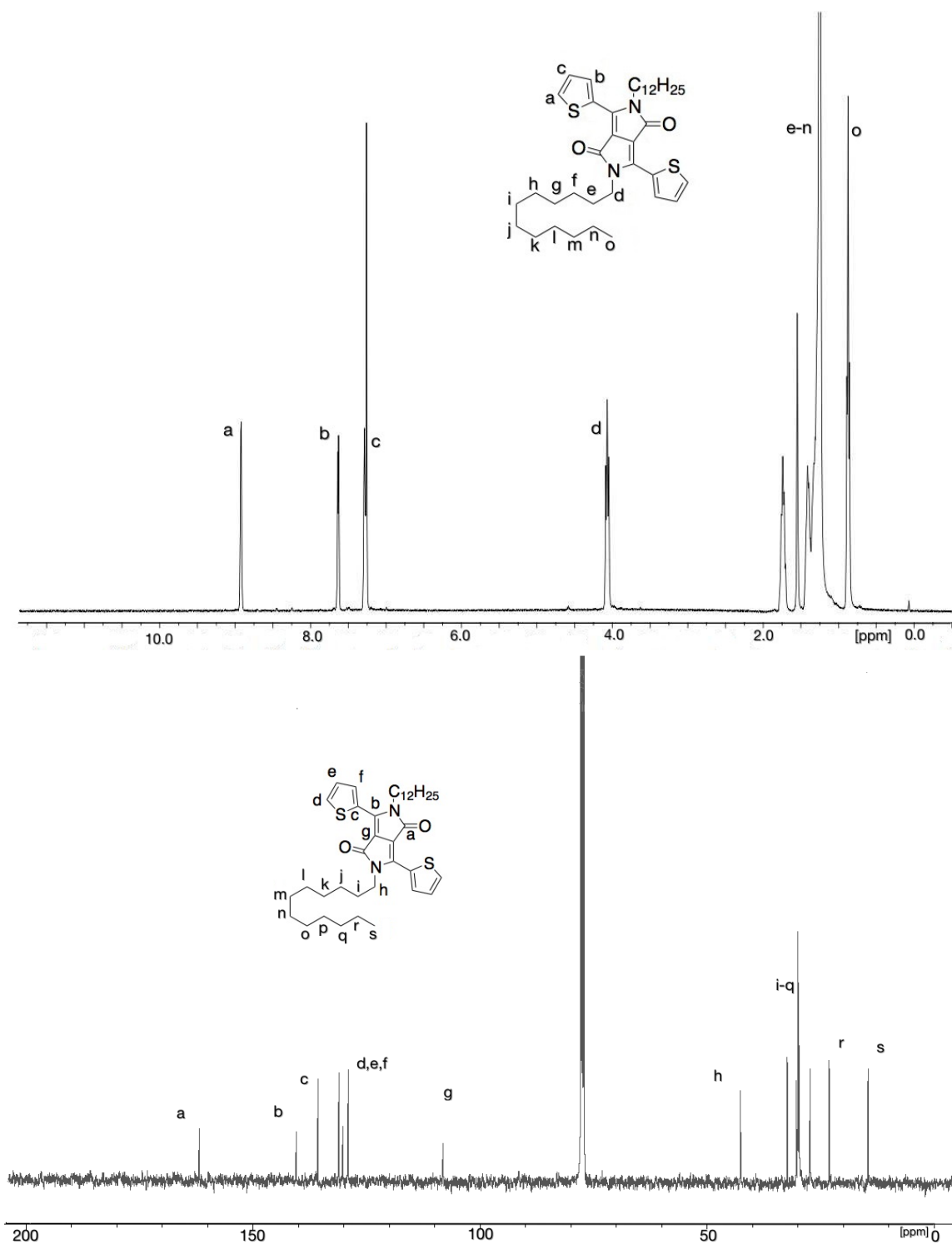
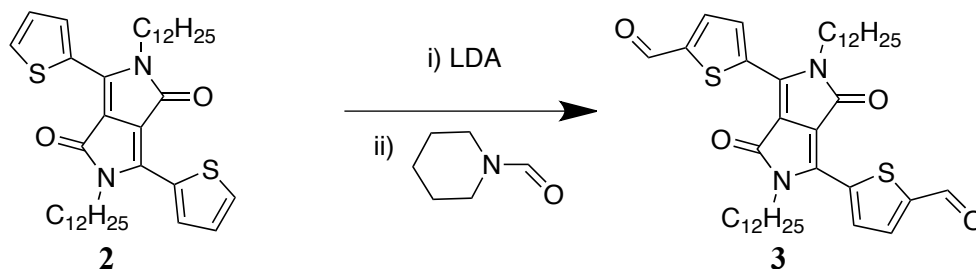


Figure A1.2 ¹H NMR and ¹³C NMR of **2** (CDCl₃, ambient temperature).

5,5'-(2,5-bis(2-dodecyl)-3,6-dioxo-2,3,5,6-tetrahydropyrrolo[3,4-*c*]pyrrole-1,4-diyl)bis(thiophene-2-carbaldehyde) (3)

3,6-Bis(thiophen-2-yl)-2,5-bis(dodecyl)pyrrolo[3,4-*c*]pyrrole-1,4-dione (**2**, 0.50 g, 0.79 mmol) was dissolved in anhydrous THF (15 mL) and cooled to -78 °C. Lithium diisopropyl amide (1.6 mL of 2 M solution in THF, 3.2 mmol) was added dropwise and temperature was raised to 0 °C over an hour. *N*-Formylpiperidine (0.36 mL, 3.20 mmol) was added dropwise and the mixture was stirred under nitrogen for 2 h. 10 mL of 1 M HCl was then added and the mixture was extracted with dichloromethane, dried over MgSO₄ and reprecipitated from methanol. Yield: 46% (0.251 g)



Scheme A1.2 Synthetic route to **3**.

¹H NMR (400 MHz, CDCl₃) δ = 10.04 (s, 2H -COH), 9.09 (d, J = 4 Hz, 2H, Ar-*H*), 7.89 (d, J = 4 Hz, 2H, Ar-*H*), 4.11 (t, J = 8 Hz, 2H, -CH₂(CH₂)₁₀ CH₃), 1.73-1.25 (m, 10H, -CH₂(CH₂)₁₀ CH₃), 0.87 (t, J = 8 Hz, 3H, -CH₂(CH₂)₁₀ CH₃) ppm.

¹³C NMR, (101 MHz, CDCl₃): δ = 182.81 (s, -COH), 161.05 (s, Ar-CO), 146.60 (s, Ar-C), 140.15-136.16 (s, Ar-C), 42.47 (s, -CH₂(CH₂)₁₀ CH₃), 31.91-22.69 (s, -CH₂(CH₂)₁₀ CH₃), 14.12 (s, -CH₂(CH₂)₁₀ CH₃) ppm.

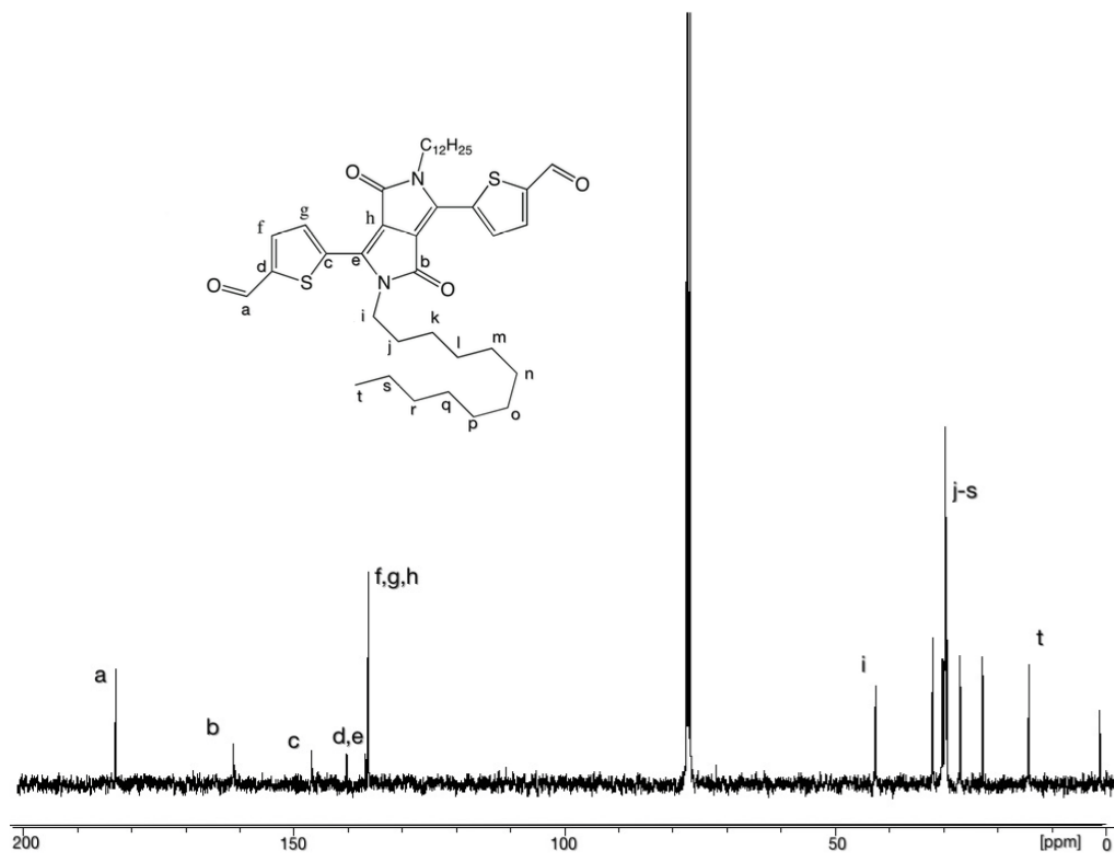
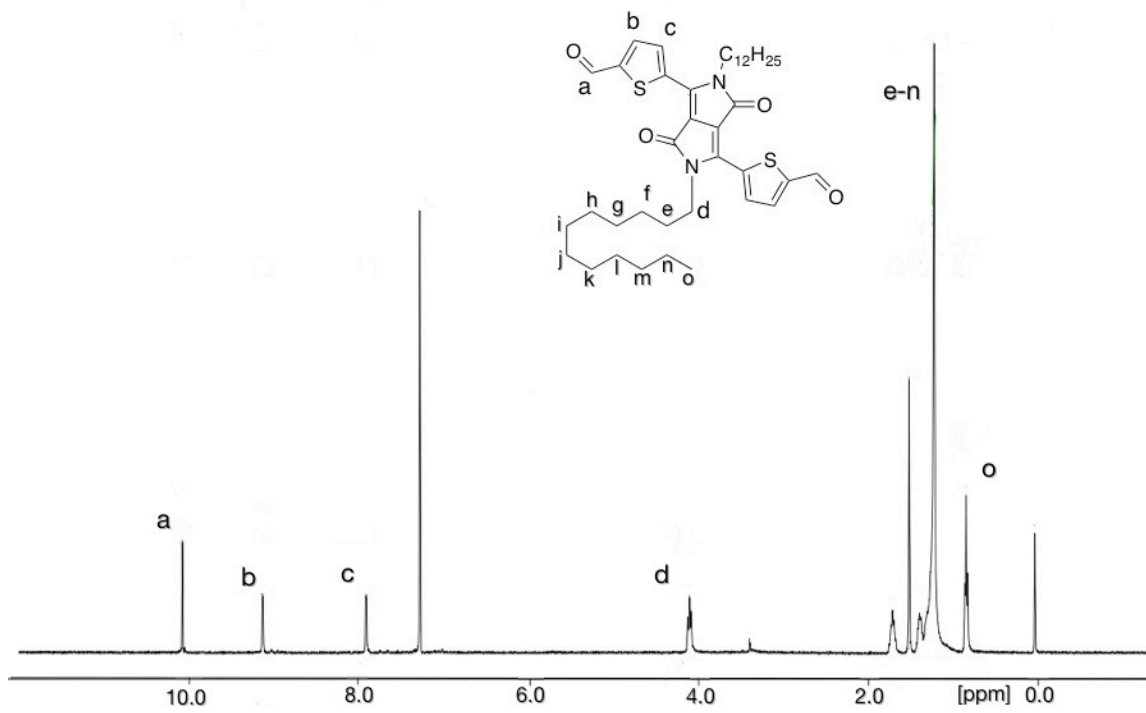


Figure A1.3 ^1H NMR and ^{13}C NMR of **3** (CDCl₃, ambient temperature).

PDPPF

N-methylglycine (0.06 g, 0.62 mmol), **3** (0.20 g, 0.31 mmol) and C₆₀ (0.23 g, 0.31 mmol) were dissolved in 1,2-dichlorobenzene (45 mL). After degassing the solution under reduced pressure, the mixture was stirred at 150 °C for 18 h and dropped into methanol. The precipitate was recovered by filtration onto a Soxhlet thimble. After washing in hexane for three days, the product was reprecipitated from methanol and hexane washed for another three days. The product was dried under reduced pressure. Yield: 67.1% (0.296 g).

¹H NMR (400.6 MHz, 1,4-dichlorobenzene) δ = 10.10 (s, -COH), 9.27 (broad, *aromatics*), 8.03-6.92 (broad, *aromatics*), 5.47 (s, -CH-N-), 5.16-4.97 (d, -CH₂-N-), 4.62 – 3.94 (broad, -CH₂(CH₂)₁₀CH₃), 3.25-2.74 (broad, -CH₃-N-), 2.27-1.29 (broad, -CH₂(CH₂)₁₀CH₃), 1.09 (broad, -CH₂(CH₂)₁₀CH₃) ppm. ¹³C NMR (100.16 MHz, 1,4-dichlorobenzene) δ = 161.10 (s, *aromatics*), 150.06-139.48 (m, *aromatics*), 108.80 (s, *aromatics*), 79.46 (-CH-N-), 70.23 (s, -CH₂-N-), 42.39 (-CH₂(CH₂)₁₀CH₃), 40.13 (s, -CH₃-N-), 32.10-22.84 (m, -CH₂(CH₂)₁₀CH₃), 14.11 (s, -CH₂(CH₂)₁₀CH₃) ppm.

2D-HSQC NMR (1,4-dichlorobenzene), d = δ = 9.50-9.14, 134.97 (*aromatics*); 8.14-6.75, 131.19-126.45 (solvent, *aromatics*) ; 5.62-4.73, 79.46 (-CH-N-) ; 5.11-4.02, 70.23 (-CH₂-N-) ; 4.53-4.08, 42.39 (-CH₂(CH₂)₁₀CH₃) ; 3.27-2.76, 40.13 (-CH₃-N-) ; 2.17-1.27, 32.10-22.84 (-CH₂(CH₂)₁₀CH₃) ; 1.09, 14.11 (-CH₂(CH₂)₁₀CH₃) ppm.

PDPPCBM

N-methylglycine (0.031 g, 0.35 mmol), **3** (0.122 g, 0.18 mmol) and PCBM (0.16 g, 0.18 mmol) were dissolved in 1,2-dichlorobenzene (8 mL). The degassed solution was stirred at 150 °C for 18 h and dropped into methanol. The precipitate was Soxhlet washed in acetone for 16 h and the product recovered from toluene as a shiny, maroon powder. Yield: 72.2% (0.203 g).

¹H NMR (400.6 MHz, CDCl₃) δ = 10.01 (s, -COH), 8.91 (broad, *aromatics*), 8.27-6.95 (broad, *aromatics*), 5.58-4.40 (broad, -CH-N-, -CH₂-N-), 4.34 – 3.82 (broad, -CH₂(CH₂)₁₀CH₃), 3.81-3.48 (-COOCH₃), 3.02-2.13 (broad, -CH₃-N-, -(CH₂)₃COOCH₃), 1.80-0.93 (broad, -CH₂(CH₂)₁₀CH₃), 0.86 (broad, -CH₂(CH₂)₁₀CH₃) ppm.

^{13}C NMR (100.16 MHz, CDCl_3) δ = 173.77 (s, $-\text{COOCH}_3$), 161.34 (s, *aromatics*), 149.91-128.23 (m, *aromatics*), 107.95 (s, *aromatics*), 78.81 ($-\text{CH}-\text{N}-$), 69.70 (s, $-\text{CH}_2-\text{N}-$), 51.78 (s, $-\text{COOCH}_3$), 42.14 ($-\text{CH}_2(\text{CH}_2)_{10}\text{CH}_3$), 40.35 (s, $-\text{CH}_3-\text{N}-$), 34.12-22.72 (m, $(\text{CH}_2)_3\text{COOCH}_3$, $-\text{CH}_2(\text{CH}_2)_{10}\text{CH}_3$), 14.19 (s, $-\text{CH}_2(\text{CH}_2)_{10}\text{CH}_3$) ppm.

2D-HSQC NMR (CDCl_3), $d = \delta =$ 9.18-8.77, 135.26 (*aromatics*); 8.30-6.9, 133.48-127.29 (*aromatics*) ; 5.12-4.78, 78.81 ($-\text{CH}-\text{N}-$) ; 5.10-4.78, 69.70 ($-\text{CH}_2-\text{N}-$) ; 4.33-3.84, 42.14 ($-\text{CH}_2(\text{CH}_2)_{10}\text{CH}_3$) ; 3.81-3.46, 51.78 (COOCH_3) ; 3.12-2.60, 40.35 ($-\text{CH}_3-\text{N}-$) ; 2.96-2.12, 35.27-31.22 ($-(\text{CH}_2)_3\text{COOCH}_3$) ; 2.13-0.63, 30.90-20.31 ($-\text{CH}_2(\text{CH}_2)_{10}\text{CH}_3$) ; 0.86, 14.19 ($-\text{CH}_2(\text{CH}_2)_{10}\text{CH}_3$) ppm

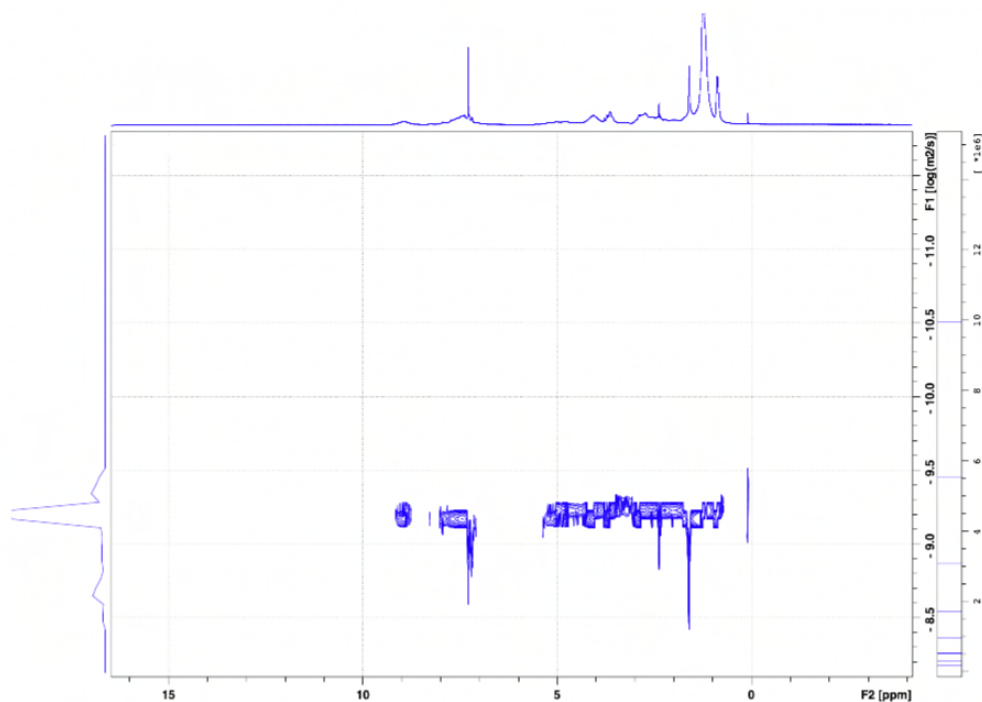


Figure A1.4. DOSY (2-D) NMR (C_6D_6 , ambient temperature) of PDPPCBM.

Appendix 2

Experimental Details and Equipment

Chemicals

All starting materials, except for PCBM (PV-A600) from Merck KGaA (Germany), were purchased from Sigma-Aldrich (France) in their analytical grades and used as received. Toluene and THF were distilled from their respective drying agents, i.e., sodium or sodium and benzophenone, under dry nitrogen. 1,2-Dichlorobenzene (DCB) was degassed under reduced pressure and nitrogen-flushed prior to use.

Equipment and Software

Photo-CELIV measurements were carried out by illuminating the sample using a 0.1 mJ laser pulsed at 3-5 ns (EKSPLA-NT 340). Triangular pulses with a rise speed of $2 \times 10^4 \text{ V s}^{-1}$ were applied using a function generator (Tektronix AFG 3011) and current transients were recorded using an oscilloscope (Tektronix DPO 4054B) with 50Ω input impedance. Variable delay times (t_{del}) were controlled by the function generator.

^1H (400.6 MHz), ^{13}C (100.16 MHz), and 2-D NMRs were recorded on a Bruker® Avance 400 spectrometer at ambient temperature using solvents as indicated. Characterisations using size exclusion chromatography (SEC) were performed at 30 °C with THF as eluent at a flow rate of 1 mL min^{-1} , a toluene flow marker, a bank of 4 columns (Shodex KF801, 802.5, 804, and 806) each of length 300 mm

and diameter 8, the whole controlled by Malvern pump (Viskotek, VE1122) connected to Malvern VE3580 refractive index and VE3210 UV-visible detectors. Calibration was against polystyrene standards and samples (0.5 to 4 mg mL^{-1}) were pre-filtered. UV-visible spectra were recorded on a Shimadzu UV-2450PC spectrophotometer. Steady-state emission and excitation spectra were recorded at 1 nm resolution using a photon counting Edinburgh FLS920 fluorescence spectrometer with a xenon lamp.

Cyclic voltammetry studies were carried out using a three-electrode assembly cell from Bio-Logic SAS and a micro-AUTOLAB Type III potentiostat-galvanostat. Measurements were performed using a glassy carbon electrode in 1,2-dichlorobenzene/acetonitrile ($4:1 \text{ v/v}$) solutions containing 0.1 M tetrabutylammonium hexafluorophosphate as electrolyte, Ag/AgNO_3 as the reference electrode, and a platinum-wire counter electrode at a scan rate 50 mVs^{-1} . The final results were calibrated with the ferrocene/ferrocenium (Fc/Fc^+) couple.

Modelling Studies

All calculations employed the RIJCOSX approximation run in Orca 3.0.3 software.²³⁰

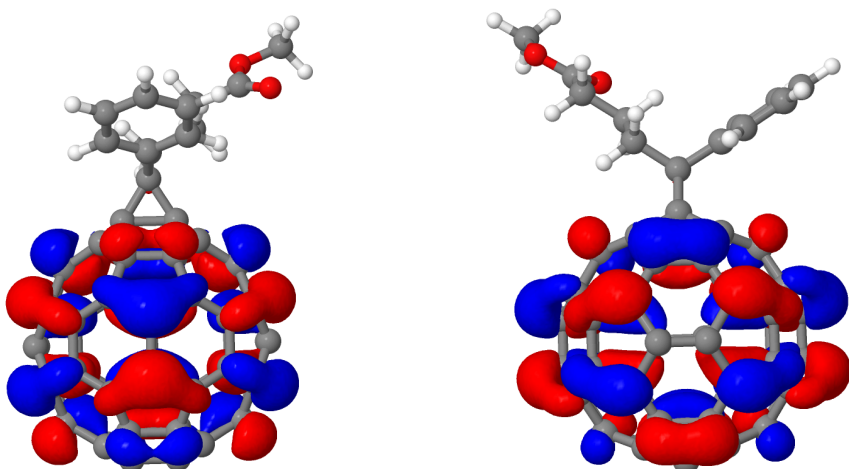


Figure A2.1. LUMO frontier orbitals for PCBM optimized using B3LYP/6-31G** level of theory. Note: The eight known attack positions for bis-adduct formation were studied by Time Dependent Density Functional Theory (TDDFT).

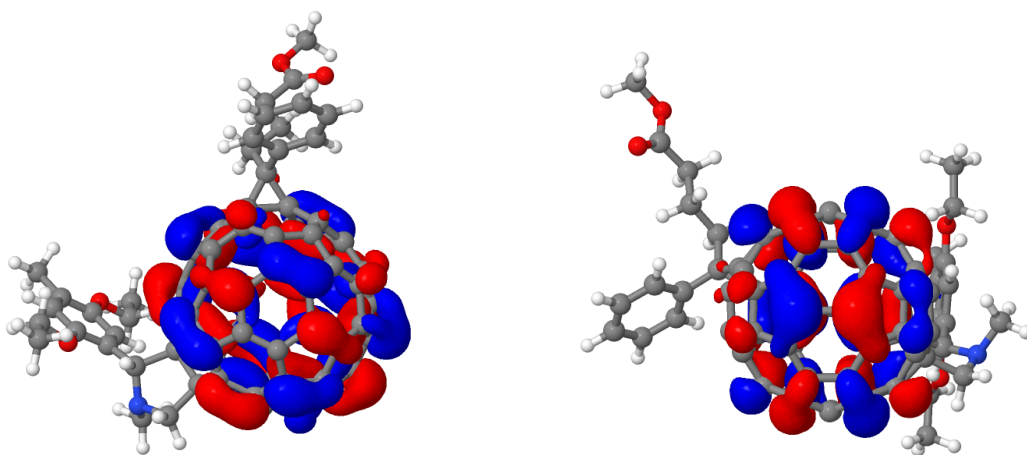


Figure A2.2. LUMO frontier orbitals for PCBM-1 optimized using B3LYP/6-31G** level of theory.

The vertical electron affinity (EA_V), adiabatic electron affinity (AE_{AD}), the chemical potential (μ), hardness (η), electrophilicity (ω), and the reorganization energies (λ) for subsequent gain and loss of an electron were similarly derived at the B3LYP/6-31G** level of theory using Orca 3.0.3 software and the results of the calculations are presented in Tables S1 and S2. The vertical electron affinity

was calculated by removing one electron from the neutral molecule and not permitting geometrical relaxation, whereas for the adiabatic electron affinity, relaxation was allowed. The difference between the ground state total energy of the neutral molecule and the total energy of the reduced state gives the value of the electron affinity. Within the vertical scenario, one can note that whichever attack happens to the fullerene sphere causes a decrease in the electron affinity.

The electrophilicity (ω) can be thought of as ‘electrophilic power’. It can be used to describe the resistance of the system to exchanging an electron with the surrounding environment, and is related to μ and η by:^{S5}

$$\omega = \frac{\mu^2}{2\eta}$$

In this case it was found that modifications reduced the electrophilicity, as expected, but also that the type of modification of the sphere and the presence of comonomer arms can impact negatively on ω .

Reorganization energies were calculated using an unrestricted open-shell wave function scheme for the Kohn-Sham orbitals. Although spin contamination is not systematic in DFT calculations, we monitored the mean value of $\langle S^2 \rangle$ in order to confine deviations within a maximum 10% of the expected value for a $\frac{1}{2}$ spin system. The ground state, however, was calculated in a restricted open-shell scheme, not allowing any spin polarization. It was found that the reorganization energies on electron transfer increase with successive modifications of the sphere, which may suggest a reduction in electron mobility at the molecular level.

Table A2.1. Energetic values calculated for C_{60} , PCBM, and the most probable structures PCBM-1 and PCBM-2.

	EA_V (EV)	EA_{AD} (EV)	μ (EV)	η (EV)	ω (EV)	LUMO (EV)
C_{60}	0	0	0	0	0	0
PCBM	-0.07	-0.06	0.24	-0.34	-0.08	0.13
PCBM-1	-0.23	-0.21	0.54	-0.61	-0.24	0.36
PCBM-2	-0.59	-0.55	0.88	-0.58	-0.53	0.80

Table A2.2. Calculated reorganization energies (λ) with respect to the reference, C_{60} .

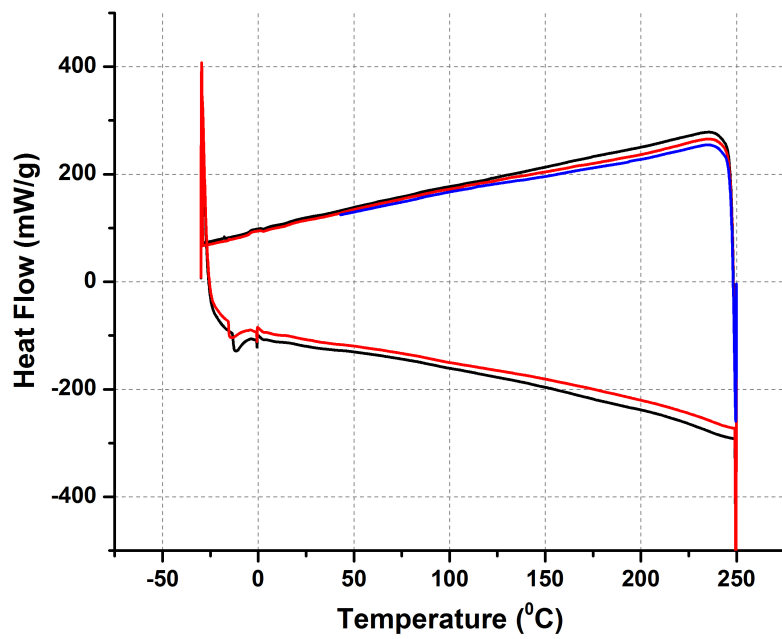
	λ_1 (MEV)	λ_2 (MEV)	λ_T (MEV)
C_{60}	0	0	0
PCBM	0.80	8.45	9.25
PCBM-1	6.98	25.96	32.93
PCBM-2	20.62	49.75	70.35

To sum, it should be noted that the values given in Tables S1 and S2 indicate general trends only at a molecular level;^{S6,S7} morphological effects are not taken into account, and they may result in a reversal of the observed results.

Calorimetry

Thermogravimetric analyses (TGA) were performed on a TA Instruments TGA Q50 at a heating rate of 10 °C min⁻¹ under nitrogen. Differential scanning calorimetry was performed on a Perkin Elmer DSC8000 with solid samples in aluminium crucibles at a heating/cooling rate of 10 °C min⁻¹ under a flux of N₂ maintained at 20 mL min⁻¹. Data treatment was performed with a Pyris™ series DSC8000 software.

(a)



(b)

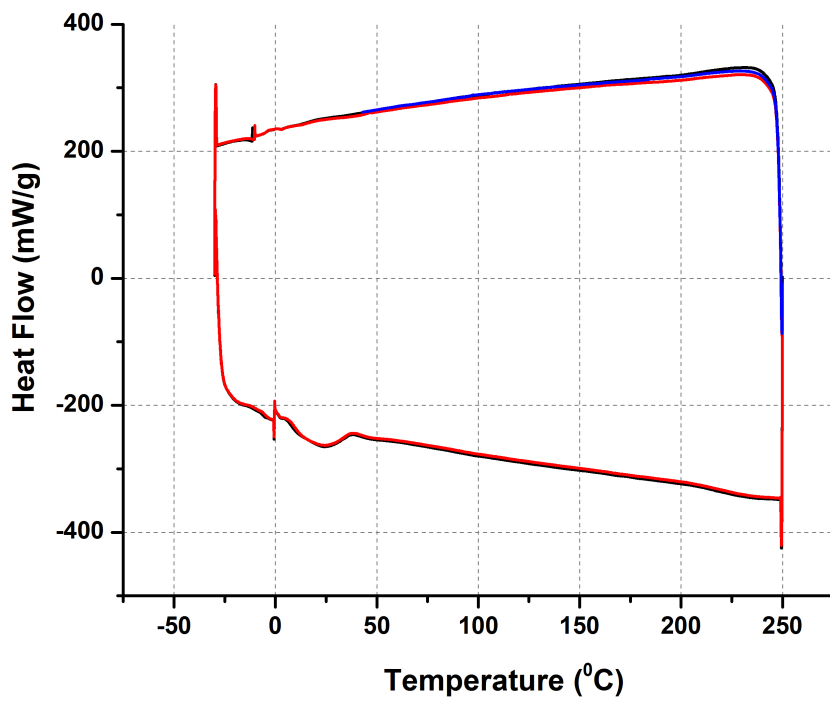


Figure A2.3 DSC Thermograms of (a) PDPF ; (b) PDPPCBM.

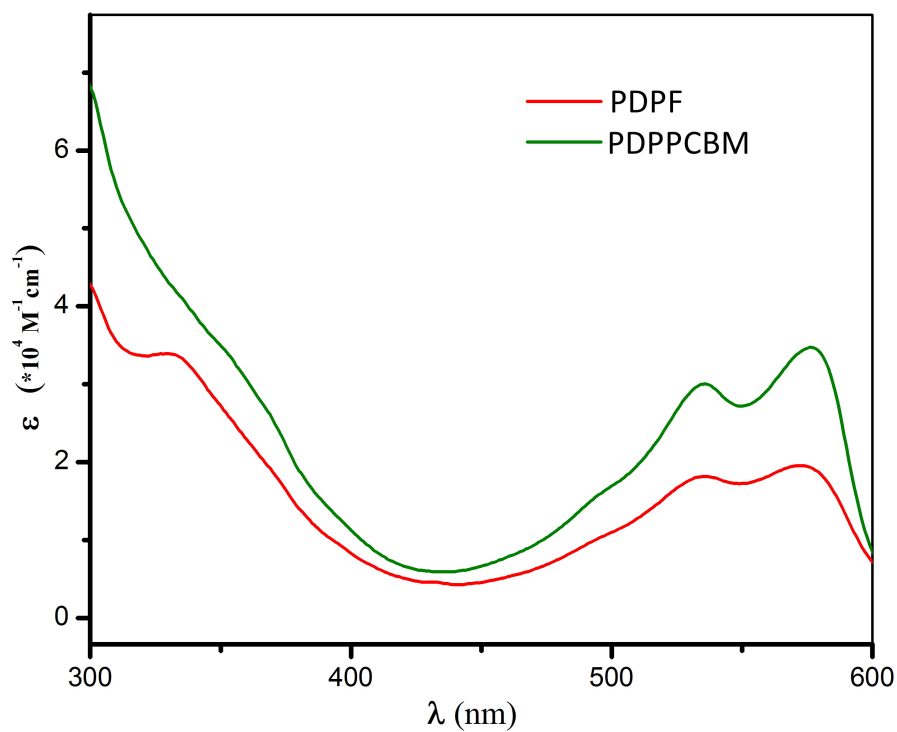


Figure A2.4 Molar extinction coefficients of PDPF and PDPPCBM

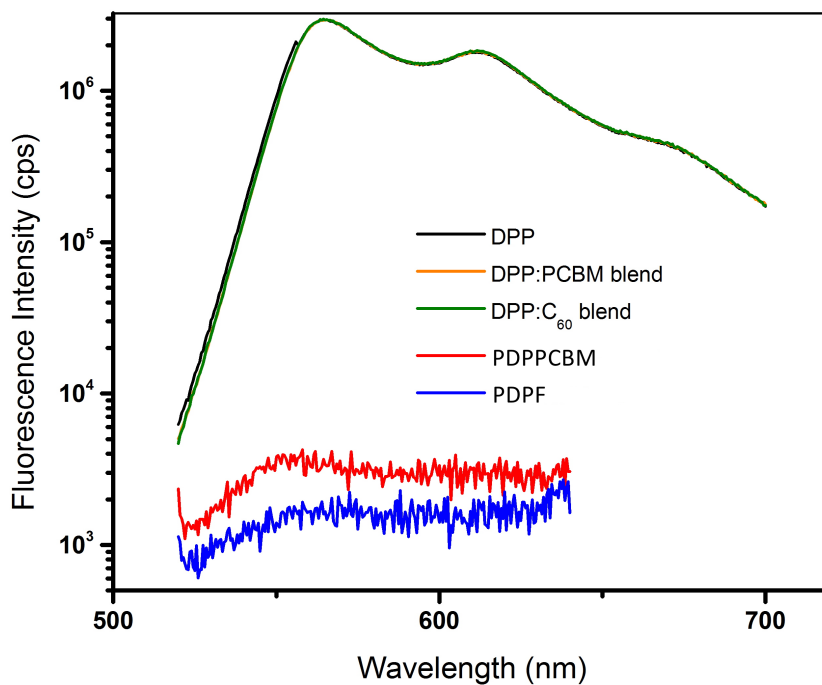


Figure A2.5 Fluorescence emission of physical blends of DPP and fullerene, PDPF and PDPPCBM.

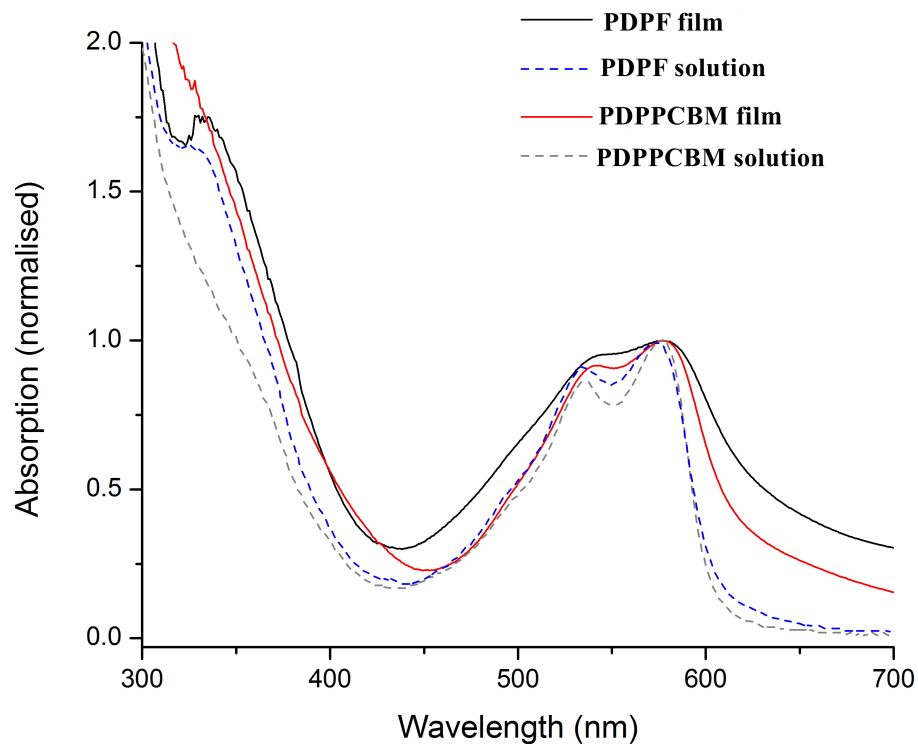


Figure A2.6 Solid-state absorption spectra for PDPF and PDPPCBM.

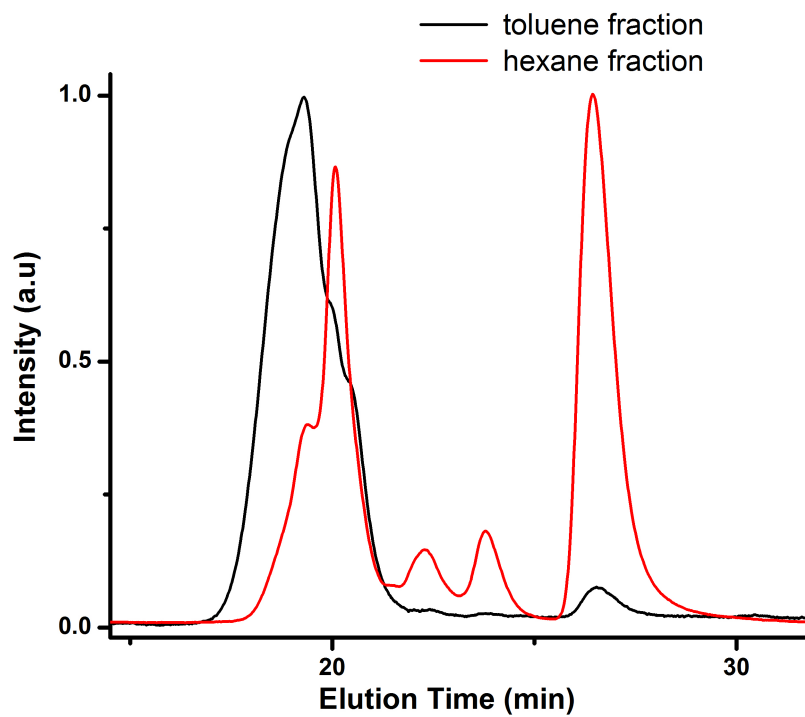


Figure A2.7 GPC overlay of toluene fraction and hexane fraction from Soxhlet wash of PDPF

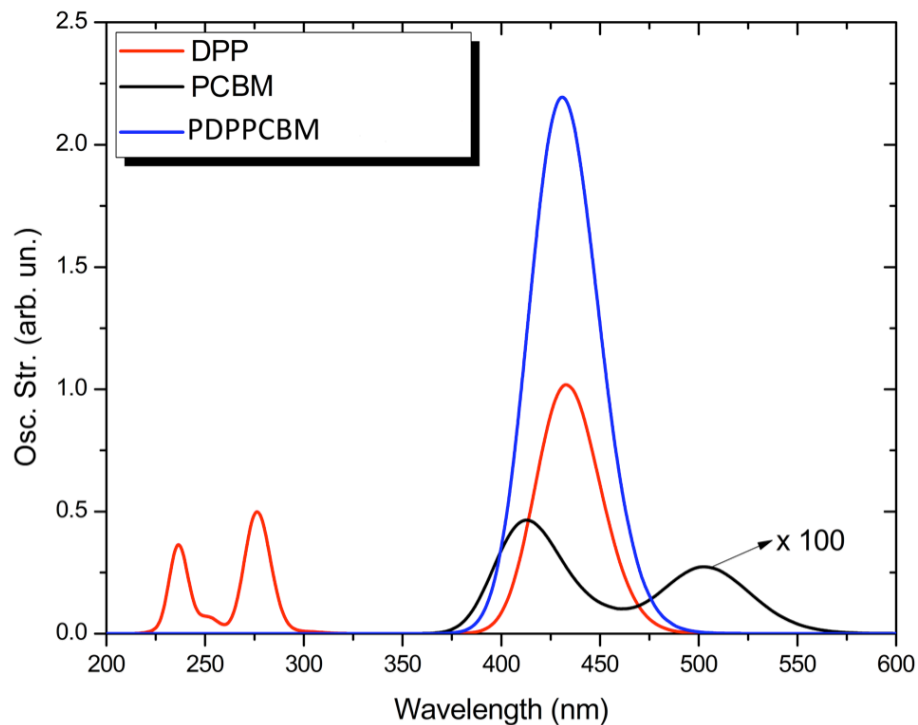


Figure A2.8 Calculated UV-visible spectra for DPP, PCBM and PDPPCBM using CAM-B3LYP and the 6-31G** base.²³¹ A total of 30 transitions were calculated and then placed within an energy envelope using the Gaussian function with 0.125 eV FWHM.

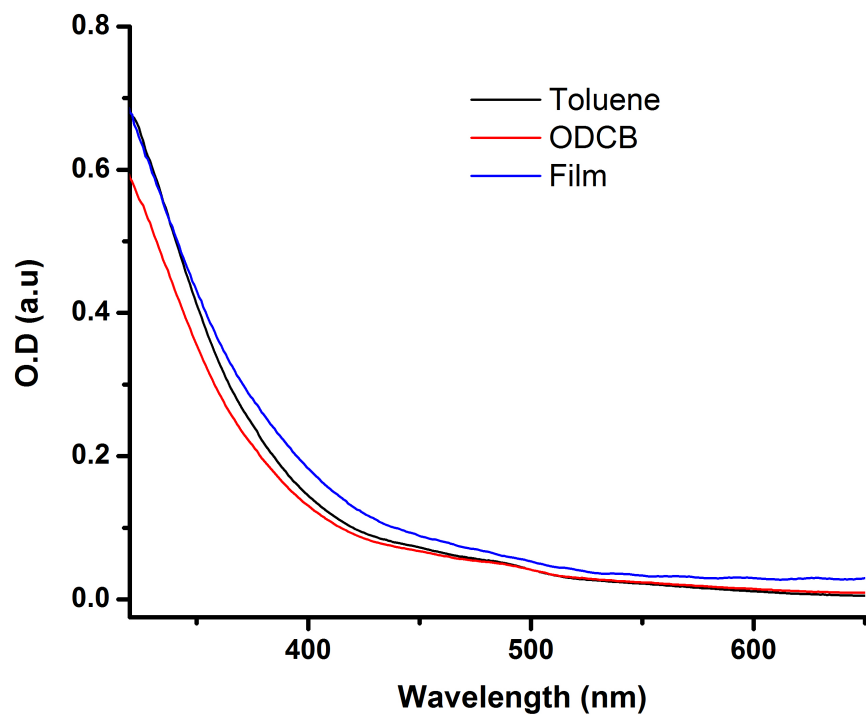


Figure A2.9 UV-Vis absorption of PPCBMB in solutions of toluene, ortho-dichlorobenzene and solid state.

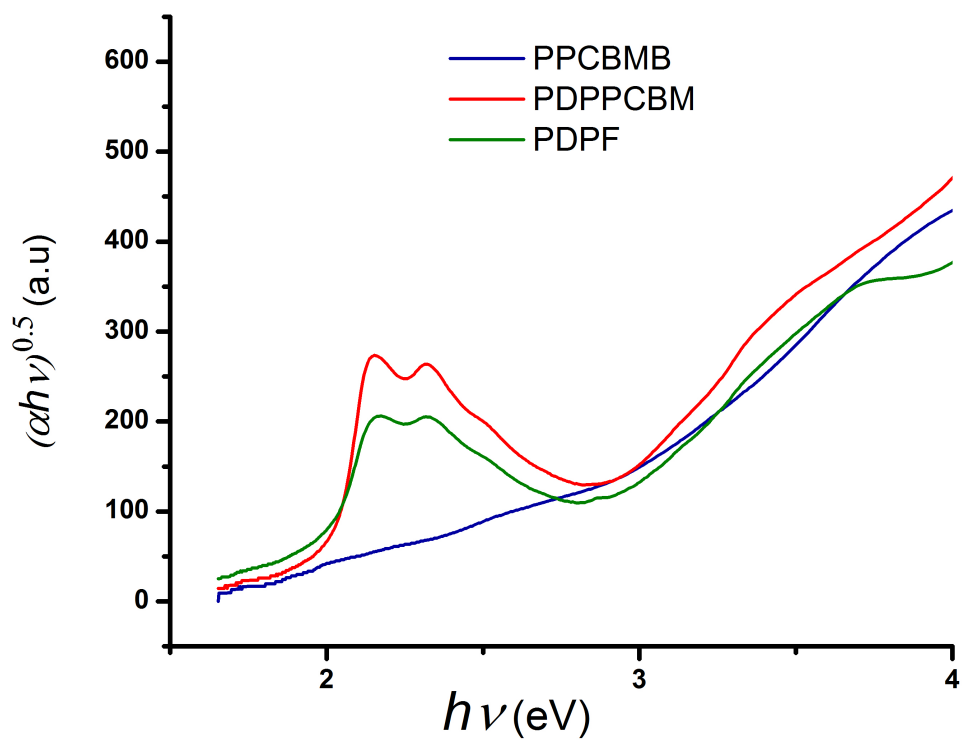


Figure A2.10. Tauc's plots for PPCBMB, PDPF and PDPPCBM.

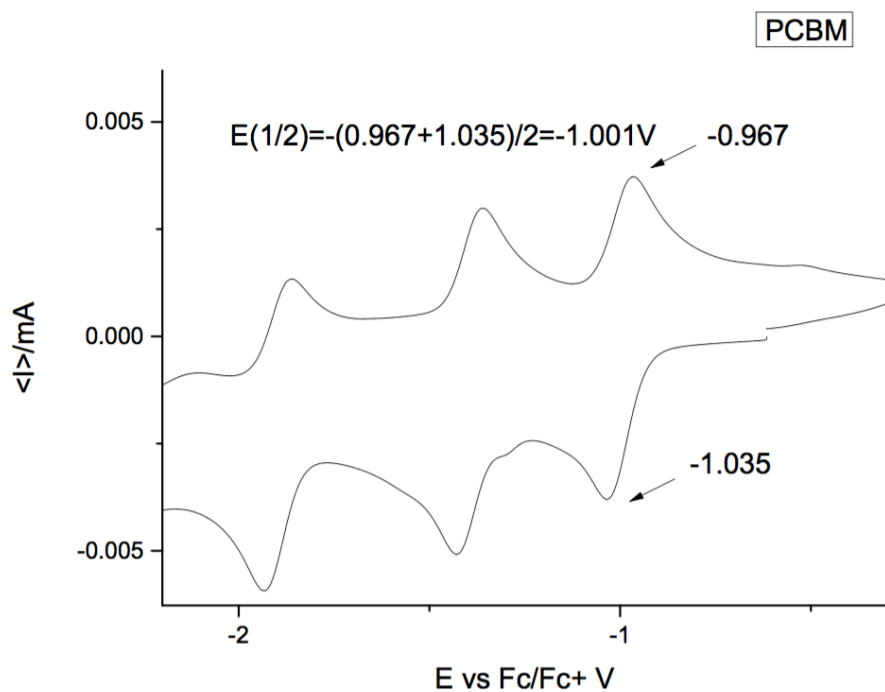


Figure A2.11 Cyclic voltammogram of PCBM.

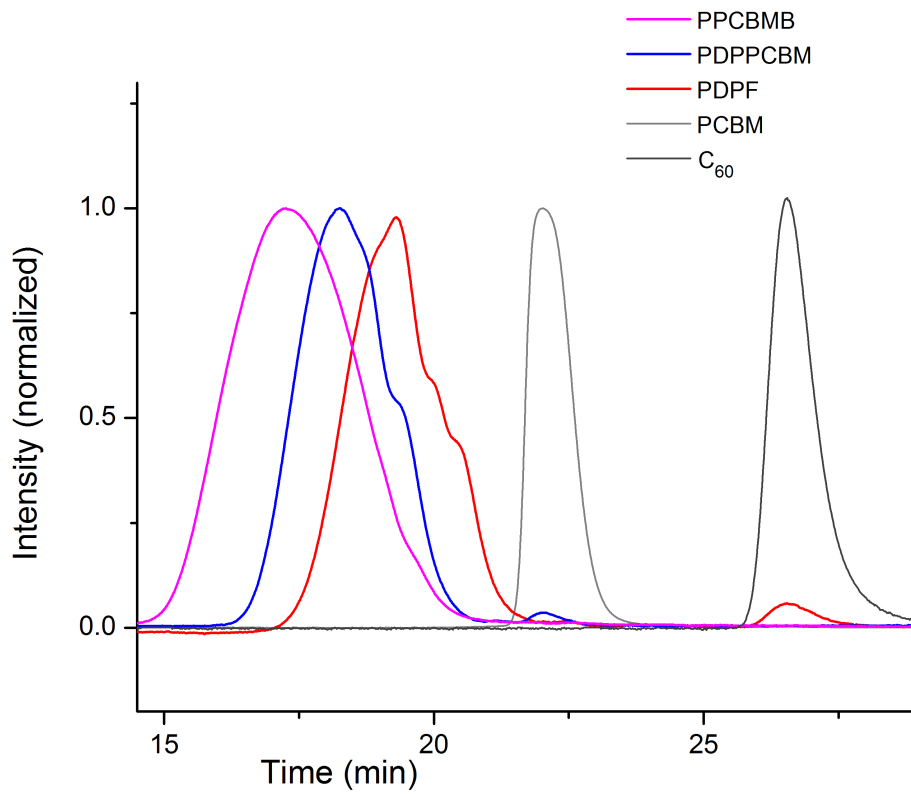


Figure A2.12 Overlay of GPC traces for PPCBMB, PDPPCBM, PDPF, PCBM and C₆₀ (THF, 30⁰ C, 330 nm)

References

- 1 Statistical Review of World Energy, **2013**.
- 2 World Energy Assessment , **2000**.
- 3 International Energy Outlook, **2013**.
- 4 World watch Institute, *Energy Report* **2014**.
- 5 U.S Space Systems Development Department. <http://www.nrl.navy.mil>
- 6 Frederik Christian Krebs, *Polymer photovoltaics - a practical approach*: ISBN: 9780819467812, SPIE Press, **2008**.
- 7 National Renewable Energy Laboratory. (2016, Feb.) <http://www.nrel.gov/pv/>
- 8 Peter Fairley, *MIT Technology Review* **2002**.
- 9 Gang Li, Rui Zhu, Yang Yang, *Nature photonics* **2012**, 6, 153.
- 10 C. K. Chiang, C. R. Fincher, Jr., Y. W. Park, A. J. Heeger, H. Shirakawa, E. J. Louis, S. C. Gau, Alan G. MacDiarmid, *Phys. Rev. Lett.* **1977**, 39, 1098.
- 11 Martin Pope, Charles E. Swenberg, *Electronic Processes in Organic Crystals and Polymers second edition*, Oxford Univ. Press, **1999**.
- 12 Harald Hoppe Niyazi Serdar Sariciftci, *J. Mater. Res.* **2004**, 19, 1924.
- 13 C.W. Tang, *Appl. Phys. Lett.* **1986**, 48, 183.
- 14 N. S. Sariciftci, L. Smilowitz, A. J. Heeger, F. Wudl, F., *Science* **1992**, 258, 1474.
- 15 L. Smilowitz, N. S. Sariciftci, R. Wu, C. Gettinger, A. J. Heeger, F. Wudl, *Phys. Rev. B* **1993**, 47, 13835.
- 16 N.S. Sariciftci, D. Braun, C. Zhang, V.I. Srdanov, A.J. Heeger, G. Stucky, F. Wudl, *Appl. Phys. Lett.* **1993**, 62, 585.
- 17 G. Yu, J. Gao, J. C. Hummelen, F. Wudl, A. J. Heeger, *Science* **1995**, 270, 1789.
- 18 Jan C. Hummelen, Brian W. Knight, F. LePeq, Fred Wudl, Jie Yao, Charles L. Wilkins, *The Journal of Organic Chemistry* **1995**, 60, 532.

-
- 19 Jingbo Zhao, Yunke Li, Guofang Yang, Kui Jiang, Haoran Lin, Harald Ade, Wei Ma, He Yan, *Nature Energy* **2016**, *1*, 15027
- 20 Wenchao Zhao, Deping Qian, Shaoqing Zhang, Sunsun Li, Olle Inganäs, Feng Gao, Jianhui Hou, *Adv. Mater.* **2016**, DOI: 10.1002/adma.201600281
- 21 Q. Zhang, B. Kan, F. Liu, G. Long, X. Wan, X. Chen, Y. Zuo, W. Ni, H. Zhang, M. Li, Z. Hu, F. Huang, Y. Cao, Z. Liang, M. Zhang, T. P. Russell, Y. Chen, *Nature Photonics* **2015**, *9*, 35
- 22 Hiroaki Benten, Daisuke Mori, Hideo Ohkita, Shinzaburo Ito, *J. Mater. Chem. A* **2016**, *4*, 5340
- 23 Liang Gao, Zhi-Guo Zhang, Lingwei Xue, Jie Min, Jianqi Zhang, Zhixiang Wei, Yongfang Li, *Adv. Mater.* **2016**, *28*, 1884
- 24 Christoph Brabec, Ullrich Scherf, Vladimir Dyakonov, *Organic Photovoltaics: Materials, Device Physics and Manufacturing Technologies*, ISBN: 978-3-527-62320-4, John Wiley & Sons **2011**.
- 25 Askat E. Jailaubekov, Adam P. Willard, John R. Tritsch, Wai-Lun Chan, Na Sai, Raluca Gearba, Loren G. Kaake, Kenrick J. Williams, Kevin Leung, Peter J. Rossky, X-Y. Zhu, *Nature Materials* **2013**, *12*, 66.
- 26 Koen Vandewal, Steve Albrecht, Eric T. Hoke, Kenneth R. Graham, Johannes Widmer, Jessica D. Douglas, Marcel Schubert, William R. Mateker, Jason T. Bloking, George F. Burkhard, Alan Sellinger, Jean M. J. Fréchet, Aram Amassian, Moritz K. Riede, Michael D. McGehee, Dieter Neher, Alberto Salleo, *Nature Materials* **2014**, *13*, 63.
- 27 Alessio Petrone, David B. Lingerfelt, Nadia Rega, Xiaosong Li, *Phys. Chem. Chem. Phys.* **2014**, *16*, 24457.
- 28 Tracey M. Clarke, James R. Durrant, *Chem. Rev.* **2010**, *110*, 6736.
- 29 Jeff Sabburg, Michael G. Kimlin Alfio V. Parisi, *Scattered and Filtered Solar UV Measurements.:* Springer Science & Business Media, **2004**.
<http://www.pveducation.org/pvcdrom/properties-of-sunlight>

-
- 30 S.Karuthedath, *Tracing Degradation Effects in Organic Solar Cells*, IMDEA Nanociencia Madrid, PhD Thesis **2015**.
- 31 Carsten Deibel, Vladimir Dyakonov, *Rep. Prog. Phys.* **2010**, *73*, 096401
- 32 N. S. Sariciftci, L. Smilowitz, A. J. Heeger, F. Wudl, *Science* **1992**, *258*, 1474
- 33 Hideo Ohkita, Steffan Cook, Yeni Astuti, Warren Duffy, Steve Tierney, Weimin Zhang, Martin Heeney, Iain McCulloch, Jenny Nelson, Donal D. C. Bradley, James R. Durrant, *J. Am. Chem. Soc.* **2008**, *130*, 3030.
- 34 Dirk Veldman, Stefan C. J. Meskers, René A. J. Janssen, *Adv. Funct. Mater.* **2009**, *19*, 1939.
- 35 Charles L. Braun, *J. Chem. Phys.* **1984**, *80*, 4157.
- 36 Wolfgang Brütting, *Physics of Organic Semiconductors*, ISBN: 978-3-527-40550-3, Wiley © **2005**.
- 37 Heinz Bässler, Anna Köhler, *Topics in Current Chemistry* **2012**, *312*, 1-65.
- 38 Manu Jaiswal, Reghu Menon, *Polym Int.* **2006**, *55*, 1371.
- 39 S. Dowland, *Optoelectronic and spectroscopic characterisation of polymer-cadmium sulfide nanocomposite solar cells*, PhD Thesis, Imperial College London, **2013**.
- 40 S. D. Baranovskii, *Phys. Stat. Sol. B* **2014**, *251*, 487.
- 41 H. Bässler, *Phys. Stat. Sol. B* **1993**, *175*, 15
- 42 K. Genevičius, *Charge carrier transport in π -conjugated polymers*, PhD Thesis, Vilnius University **2003**.
- 43 Don Monroe, *Phys. Rev. Lett.* **1985**, *54*, 146
- 44 Ling Li, Gregor Meller, Hans Kosina, *Applied Physics Letters* **2008**, *92*, 013307
- 45 S. D. Baranovskii, T. Faber, F. Hensel, P. Thomas, *J. Phys.: Condens. Matter* **1997**, *9*, 2699
- 46 C. Tanase, E. J. Meijer, P. W. M. Blom, D. M. de Leeuw, *Phys. Rev. Lett.* **2003**, *91*, 216601.

-
- 47 W. F. Pasveer, J. Cottaar, C. Tanase, R. Coehoorn, P. A. Bobbert, P. W. M. Blom, D. M. de Leeuw, M. A. J. Michels, *Phys. Rev. Lett.* **2005**, *94*, 206601.
- 48 Martin Pope, Charles E. Swenberg, *Electronic Processes in Organic Crystals and Polymers 2nd edition*, Oxford University Press 1999
- 49 A. Pivrikas, G. Juška, A. J. Mozer, M. Scharber, K. Arlauskas, N. S. Sariciftci, H. Stubb, R. Österbacka, *Phys. Rev. Lett.* **2005**, *94*, 176806
- 50 C. Deibel, A. Baumann, V. Dyakonov, *Appl. Phys. Lett.* **2008**, *93*, 163303
- 51 Gytis Juška, Kristijonas Genevičius, Nerijus Nekrašas, Gytis Sliaužys, Ronald Österbacka, *Appl. Phys. Lett.* **2009**, *95*, 013303
- 52 Jing-De Chen, Chaohua Cui, Yan-Qing Li, Lei Zhou, Qing-Dong Ou, Chi Li, Yongfang Li, Jian-Xin Tang, *Advanced Materials* **2014**, *27*, 1035
- 53 Yuhang Liu, Jingbo Zhao, Zhengke Li, Cheng Mu, Wei Ma, Huawei Hu, Kui Jiang, Haoran Lin, Harald Ade, He Yan, *Nature Communications* **2014**, *5*, 5293
- 54 Mikkel Jørgensen, Kion Norrman, Frederik C. Krebs, *Solar Energy Materials & Solar Cells* **2008**, *92*, 686.
- 55 Mikkel Jørgensen, Kion Norrman, Suren A. Gevorgyan, Thomas Tromholt, Birgitta Andreasen, and Frederik C. Krebs, *Advanced Materials* **2012**, *24*, 580.
- 56 Nadia Grossiord, Jan M. Kroon, Ronn Andriessen, Paul W.M. Blom, *Organic Electronics* **2012**, *13*, 432.
- 57 J.A. Hauch, P. Schilinsky, S.A. Choulis, R. Childers, M. Biele, C.J. Brabec, *Solar Energy Materials and Solar Cells* **2008**, *92*, 727.
- 58 J. Kong, S. Song, M. Yoo, G.Y. Lee, O. Kwon, J.K. Park, H. Back, G. Kim, S.H. Lee, H. Suh, K. Lee, *Nature Communications* **2014**, *5*, 5688.
- 59 S. Karuthedath, T. Sauermann, H-J. Egelhaaf, R. Wannemacher, C. J. Brabec, L. Lüer, *J. Mater. Chem. A* **2015**, *3*, 3399.
- 60 K. Norrman, M. V. Madsen, S. A. Gevorgyan, F. C. Krebs, *J. Am. Chem. Soc.* **2010**, *132*, 16883.

-
- 61 K. Kawano, R. Pacios, D. Poplavskyy, J. Nelson, D. D. C. Bradley, J. R. Durrant, *Solar Energy Materials and Solar Cells* **2006**, *90*, 3520.
- 62 K. Norrman, S. A. Gevorgyan, F. C. Krebs, *ACS Applied Materials & Interfaces* **2009**, *1*, 102.
- 63 M. Hermenau, M. Riede, K. Leo, S. A. Gevorgyan, F. C. Krebs, K. Norrman, *Solar Energy Materials and Solar Cells* **2011**, *95*, 1268.
- 64 T. S. Glen, N. W. Scarratt, H. Yi, A. Iraqi, T. Wang, J. Kingsley, A. R. Buckley, D. G. Lidzey, A. M. Donald, *Journal of Polymer Science, Part B: Polymer Physics* **2016**, *54*, 216.
- 65 A. Rivaton, S. Chambon, M. Manceau, J-L. Gardette, N. Lemaître, S. Guillerez, *Polymer Degradation and Stability* **2010**, *95*, 278.
- 66 E. Voroshazi, I. Cardinaletti, T. Conard, B. P. Rand, *Advanced Energy Materials* **2014**, *4*, 1400848.
- 67 E. Sengupta, A. L. Domanski, S. A. L. Weber, M. B. Untch, H-J. Butt, T. Sauermann, H-J. Egelhaaf, R. Berger, *J. Phys. Chem. C* **2011**, *40*, 19994.
- 68 W. Bagienski, M. C. Gupta, *Solar Energy Materials and Solar Cells* **2011**, *95*, 933.
- 69 E. A. Katz, D. Faiman, S. M. Tuladhar, J. M. Kroon, M. M. Wienk, T. Fromherz, F. Padinger, C. J. Brabec, N. S. Sariciftci, *Journal of Applied Physics* **2001**, *90*, 5343.
- 70 Sabine Bertho, Griet Janssen, Thomas J. Cleij, Bert Conings, Wouter Moons, Abay Gadisa, Jan D'Haen, Etienne Goovaerts, Laurence Lutsen, Jean Manca, Dirk Vanderzande, *Solar Energy Materials And Solar Cells* **2008**, *92*, 753.
- 71 S. Savagatrup, A.D. Printz, T.F. O'Connor, A.V. Zaretski, D. Rodriguez, E.J. Sawyer, K.M. Rajan, R.I. Acosta, S.E. Root, D.J. Lipomi, *Energy Environ. Sci.* **2015**, *8*, 55.
- 72 K. Norrman, M. V. Madsen, S. A. Gevorgyan, F. C. Krebs, *J. Am. Chem. Soc* **2010**, *132*, 16883.

-
- 73 Donggeon Han, Seunghyup Yoo, *Solar Energy Materials and Solar Cells* **2014**, *128*, 41.
- 74 S. Kundu, S. R. Gollu, R. Sharma , Srinivas G, A. Ashok, A. R. Kulkarni, D. Gupta, *Organic Electronics* **2013**, *14*, 3083.
- 75 W. Wang, C. J. Schaffer, L. Song, V. Körstgens, S. Pröller, E. D. Indari, T. Wang, A. Abdelsamie, S. Bernstorff, P. M.-Buschbaum, *J. Mater. Chem. A* **2015**, *3*, 8324.
- 76 Z. He, C. Zhong, S. Su, M. Xu, H. Wu, Y. Cao, *Nature Photonics* **2012**, *6*, 591.
- 77 Xu Z., Chen L.-M., Yang G., Huang C.-H., Hou J., Wu Y., Li G., Hsu C.-S., Yang Y., *Adv. Funct. Mater.* **2009**, *19*, 1227
- 78 S. K. Hau, H.-L. Yip, H. Ma, A. K.-Y. Jen, *Appl. Phys. Lett.* **2008**, *93*, 233304.
- 79 Naveen Kumar Elumalai, Amitaksha Saha, Chellappan Vijila, Rajan Jose, Zhang Jieb, Seeram Ramakrishna, *Phys. Chem. Chem. Phys.* **2013**, *15*, 6831.
- 80 Chambon S, Manceau M, Firon M, Cros S, Rivaton A, Gardette J.-L., *Polymer* **2008**, *49*, 3288
- 81 S. Chambon, A. Rivaton, J. -L. Gardette, M. Firon, L. Lutsen, *Journal of Polymer Science: Part A: Polymer Chemistry* **2007**, *45*, 317
- 82 H. Santos Silva, A. Tournebize, D. Bégué, H. Peisert, T. Chassé, J.-L. Gardette, S. Therias, A. Rivaton, R. C. Hiorns, *RSC Adv.* **2014**, *4*, 54919
- 83 S. Chambon, A. Rivaton, J. -L. Gardette, M. Firon, *Solar Energy Materials and Solar Cells* **2007**, *91*, 394
- 84 Matthieu Manceau, Sylvain Chambon, Agnès Rivaton, Jean-Luc Gardette, Stephane Guillerez, Noëlla Lemaître, *Solar Energy Materials and Solar Cells* **2010**, *94*, 1572.
- 85 M. Manceau, A. Rivaton, J.-L. Gardette, S. Guillerez, N. Lemaître, *Polymer degradation and stability* **2009**, *94*, 898
- 86 C. J. Brabec, G. Zerza, G. Cerullo, S. De Silvestri, S. Luzzati, J. C. Hummelen, S. Sariciftci, *Chem. Phys. Lett.* **2001**, *340*, 232

-
- 87 M. O. Reese, A. M. Nardes, B. L. Rupert, R. E. Larsen, D. C. Olson, M. T. Lloyd, S. E. Shaheen, D. S. Ginley, G. Rumbles, N. Kopidakis, *Adv. Funct. Mater.* **2010**, *20*, 3476
- 88 A. Aguirre, S. C. J. Meskers, R. A. J. Janssen, H.-J. Egelhaaf, *Organic Electronics* **2011**, *12*, 1657.
- 89 Andrea Seemann, Tobias Sauermann, Christoph Lungenschmied, Oskar Armbruster, Siegfried Bauer, H.-J. Egelhaaf, Jens Hauch, *Solar Energy* **2011**, *85*, 1238.
- 90 Matthieu Manceau, Eva Bundgaard, Jon E. Carle, Ole Hagemann, Martin Helgesen, Roar Søndergaard, Mikkel Jørgensen, Frederik C. Krebs, *Journal of Materials Chemistry* **2011**, *21*, 4132.
- 91 Umut Aygul, Hans-Joachim Egelhaaf, Peter Nagel, Michael Merz, Stefan Schuppler, Klaus Eichele, Heiko Peisert, Thomas Chasse, *Chem. Phys. Chem* **2015**, *16*, 428.
- 92 Jenny Nelson, Joe J. Kwiatkowski, James Kirkpatrick, Jarvist M. Frost, *Acc. Chem. Res.*, **2009**, *42*, 1768
- 93 Sophie Barrau, Viktor Andersson, Fengling Zhang, Sergej Masich, Johan Bijleveld, Mats R. Andersson, Olle Inganäs, *Macromolecules* **2009**, *42*, 4646
- 94 Hao Xin, Obadiah G. Reid, Guoqiang Ren, Felix Sunjoo Kim, David S. Ginger, Samson A. Jenekhe, *ACS Nano* **2010**, *4*, 1861
- 95 Sung Heum Park, Anshuman Roy, Serge Beaupré, Shinuk Cho, Nelson Coates, Ji Sun Moon, Daniel Moses, Mario Leclerc, Kwanghee Lee, Alan J. Heeger, *Nature Photonics* **2009**, *3*, 297
- 96 G. Yu, J. Gao, J. C. Hummelen, F. Wudl, A. J. Heeger, *Science* **1995**, *270*, 1789
- 97 Soo Won Heo, Seung Hee Kim, Eui Jin Lee, Doo Kyung Moon, *Solar Energy Materials and Solar Cells* **2013**, *111*, 16

-
- 98 Kristin Schmidt, Christopher J. Tassone, Jeremy R. Niskala, Alan T. Yiu, Olivia P. Lee, Thomas M. Weiss, Cheng Wang, Jean M. J. Fréchet, Pierre M. Beaujuge, Michael F. Toney, *Advanced Materials* **2014**, *26*, 300
- 99 G. Li, Y. Yao, H. Yang, V. Shrotriya, G. Yang, Y. Yang, *Advanced Functional Materials* **2007**, *17*, 1636
- 100 N. Camaioni, G. Ridolfi, G. Casalbore-Miceli, G. Possamai, M. Maggini, *Adv. Mater.* **2002**, *14*, 1735
- 101 G. Li, V. Shrotriya, J. S. Huang, Y. Yao, T. Moriarty, K. Emery, Y. Yang, *Nat. Mater.* **2005**, *4*, 864.
- 102 Christian Kästner, Daniel A. M. Egbe, Harald Hoppe, *J. Mater. Chem. A* **2015**, *3*, 395
- 103 Jonathon W. Kiel, Aaron P. R. Eberle, Michael E. Mackay, *Phys. Rev. Lett.* **2010**, *105*, 168701
- 104 Mariano Campoy-Quiles, Toby Ferenczi, Tiziano Agostinelli, Pablo G. Etchegoin, Youngkyoo Kim, Thomas D. Anthopoulos, Paul N. Stavrinou, Donald C. Bradley, Jenny Nelson, *Nature Materials* **2008**, *7*, 158.
- 105 D Chirvase, J Parisi, J C Hummelen, V Dyakonov, *Nanotechnology* **2004**, *15*, 1317
- 106 Bert Conings, Sabine Bertho, Koen Vandewal, Alessia Senes, Jan D'Haen, Jean Manca, René A. J. Janssen, *Applied Physics Letters* **2010**, *96*, 163301.
- 107 R. Boistelle, J. P. Astier, *J. Cryst. Growth* **1988**, *90*, 14.
- 108 K. Maturová, S. S. van Bavel, M. M. Wienk, R. A. J. Janssen, M. Kemerink, *Nano Lett.* **2009**, *9*, 3032.
- 109 J. Knol, J. C. Hummelen, *J. Am. Chem. Soc.* **2000**, *122*, 3226.
- 110 A. Dzwilewski, T. Wågberg, L. Edman, *J. Am. Chem. Soc.* **2009**, *131*, 4006
- 111 A. Dzwilewski, P. Matyba, L. Edman, *J. Phys. Chem. B* **2009**, *114*, 135
- 112 Fortunato Piersimoni et al., *Journal of Polymer Science Part B: Polymer Physics* **2013**, *51*, 1209.

-
- 113 Gary B. Adams, John B. Page, Otto F. Sankey, Michael O’Keeffe, *Phys. Rev. B* **1994**, *50*, 17471
- 114 Ping Zhou, Zheng-Hong Dong, A.M. Rao, P.C Eklund, *Chemical Physics Letters* **1993**, *211*, 337.
- 115 P. C. Eklund, A. M. Rao, P. Zhou, Y. Wang, J. M. Holden, *Thin Solid Films* **1995**, *257*, 185
- 116 A. M. Rao, K.-A.Wang, J. M. Holden, Y. Wang, P. Zhou, P. C. Eklund, C. C. Eloi, J. D. Robertson, *J. Mater. Res.* **1993**, *8*, 2277
- 117 Andreas Distler, Tobias Sauermann, Hans-Joachim Egelhaaf, Sheila Rodman, Dave Waller, Kap-Soo Cheon, Mike Lee, Dirk M. Guldi, *Adv. Energy Mater.* **2014**, *4*, 1300693
- 118 (a) Yen-Ju Cheng, Chao-Hsiang Hsieh, Pei-Jung Li, Chain-Shu Hsu, *Advanced Functional Materials* **2011**, *21*, 1723; (b) Shoji Miyanishi, Keisuke Tajima, Kazuhito Hashimoto, *Macromolecules* **2009**, *42*, 1610
- 119 (a) Z. Li, H. C. Wong, Z. Huang, H. Zhong, C. H. Tan, W. C. Tsoi, J. S. Kim, J. R. Durrant, J. T. Cabral, *Nature Communications* **2013**, *4*, 2227; (b) H. C. Wong, Z. Li, C. H. Tan, H. Zhong, Z. Huang, H. Bronstein, I. McCulloch, J. T. Cabral, J. R. Durrant, *ACS Nano* **2014**, *8*, 1297
- 120 B. C. Schroeder, Z. Li, M. A. Brady, G. C. Faria, R. S. Ashraf, C. J Takacs, J. S. Cowart, D. T. Duong, K. H. Chiu, C.-H. Tan, J. T. Cabral, A. Salleo, M. L. Chabiny, J. R. Durrant, I. McCulloch, *Angew Chem Int Ed.* **2014**, *53*, 12870
- 121 Jia Wang, Jenny Enevold, Ludvig Edman, *Advanced Functional Materials* **2013**, *23*, 3220
- 122 G. Juška, K. Arlauskas, M. Viliūnas, J. Kočka, *Physical Review Letters* **2000**, *84*, 4946
- 123 G. Juška, K. Arlauskas, M. Viliūnas, K. Genevičius, R. Österbacka, H. Stubb, *Physical Review B* **2000**, *62*, R16235

-
- 124 Juška G, Arlauskas K, Nekrašas N, Stuchlik J, Niquille X and Wyrsh N, *Journal of Non-Crystalline Solids* **299**: 375 (2002)
- 125 (a) Spear WE, *Proc. Phys. Soc. B* **70**:1139 (1957); (b) Le Blanc OH, *J. Chem. Phys.* **33**: 626 (1960); (c) Kepler RG, *Phys. Rev.* **119**: 1226 (1960)
- 126 A. Pivrikas, N. S. Sariciftci, G. Juška, R. Österbacka, *Prog. Photovolt: Res. Appl.* **2007**, *15*,677
- 127 J.A. Hauch, P. Schilinsky, S.A. Choulis, S. Rajoelson, C.J. Brabec, *Appl. Phys. Lett.* **2008**, *93*, 103306
- 128 M. O. Reese, A. J. Morfa, M. S. White, N. Kopidakis, S. E. Shaheen, G. Rumbles, D. S. Ginley, *Sol. Energy Mater. Sol. Cells* **2008**, *92*, 746
- 129 Andrea Seemann, H.-J. Egelhaaf, Christoph J. Brabec, Jens A. Hauch, *Organic Electronics* **2009**, *10*, 1424
- 130 Andrea Seemann, Tobias Sauermann, Christoph Lungenschmied, Oskar Armbruster, Siegfried Bauer, H.-J. Egelhaaf, Jens Hauch, *Solar Energy* **2011**, *85*, 1238
- 131 Julia Schafferhans, Andreas Baumann, Alexander Wagenpohl, Carsten Deibel, Vladimir Dyakonov, *Organic Electronics* **2010**, *11*, 1693
- 132 R. Alex Marsh, Justin M. Hodgkiss, Sebastian Albert-Seifried, Richard H. Friend *Nano Lett.*, **2010**, *10*, 923
- 133 Felix Deschler, Antonietta De Sio, Elizabeth von Hauff, Peter Kutka, Tobias Sauermann, Hans-J. Egelhaaf, Jens Hauch, Enrico Da Como, *Adv. Funct. Mater.* **2012**, *22*, 1461
- 134 H.-H. Liao, Ch.-M. Yang, Ch.-Ch. Liu, S.-F. Horng, S.-F. Meng, J.-T. Shy, *J. Appl. Phys.* **2008**, *103*, 1045061
- 135 H. Hintz, H. Peisert, H.-J. Egelhaaf, T. Chasse, *J. Phys. Chem. C* **2011**, *115*,13373
- 136 J. Schafferhans, A. Baumann, C. Deibel, V. Dyakonov, *Appl. Phys. Lett.* **2008**, *93*, 093303

-
- 137 Safakath Karuthedath, Tobias Sauermann, Hans-Joachim Egelhaaf, Reinhold Wannemacher, Christoph J. Brabec, Larry Lüer, *J. Mater. Chem. A* **2015**, *3*, 3399
- 138 Ankit Kumar, Hua-Hsien Liao, Yang Yang, *Organic Electronics* **2009**, *10*, 1615
- 139 Gytis Juška, Kristijonas Genevičius, Nerijus Nekrašas, Gytis Sliaužys, Ronald Österbacka, *Appl. Phys. Lett.* **2009**, *95*, 013303
- 140 S. Beaupré, P.-L. T. Boudreault, M. Leclerc, *Adv. Mater.* **2010**, *22*, E6.
- 141 M. Helgesen, R. Søndergaard, F. C. Krebs, *J. Mater. Chem.* **2010**, *20*, 36
- 142 Hsiang-Yu Chen, Jianhui Hou, Shaoqing Zhang, Yongye Liang, Guanwen Yang, Yang Yang, Luping Yu, Yue Wu, Gang Li, *Nature Photonics* **2009**, *3*, 649
- 143 Lan S.C., Chang C.K., Wang Y.C., Wei K.H., *Chemphyschem.* **2015**, *16*, 1268
- 144 Isabel Fraga Domínguez, Paul D.Topham, Pierre-Olivier Bussière, Didier Bégué, Agnès Rivaton, *J. Phys. Chem. C* **2015**, *119*, 2166
- 145 Martin H. Petersen, Suren A. Gevorgyan, Frederik C. Krebs, *Macromolecules* **2008**, *41*, 8986
- 146 Abay Gadisa, Wibren D. Oosterbaan, Koen Vandewal, Jean-Christophe Bolsée, Sabine Bertho, Jan D'Haen, Laurence Lutsen, Dirk Vanderzande, Jean V. Manca, *Adv. Funct. Mater.* **2009**, *19*, 3300
- 147 Yangjun Xia, Junfeng Tong, Bin Li, Chenglong Wang, Hongzhong Liu, *J. Polym. Sci. A Polym. Chem.* **2011**, *49*, 2969
- 148 Jurgen Kesters, Pieter Verstappen, Jorne Raymakers, Wouter Vanormelingen, Jeroen Drijkoningen, Jan D'Haen, Jean Manca, Laurence Lutsen, Dirk Vanderzande, Wouter Mae, *Chem. Mater.* **2015**, *27*, 1332
- 149 Graham E. Morse, Aurélien Tournebize, Agnès Rivaton, Thomas Chassé, Christine Taviot-Gueho, Nicolas Blouin, Owen R. Lozman, Steven Tierney, *Phys. Chem. Chem. Phys.* **2015**, *17*, 11884

-
- 150 William R. Mateker, Thomas Heumueller, Rongrong Cheacharoen, I. T. Sachs-Quintana, Michael D. McGehee, *Chem. Mater.* **2015**, *27*, 6345
- 151 Soon Ok Jeon, Jun Yeob Lee, *Solar Energy Materials and Solar Cells* **2012**, *101*, 160
- 152 Li-Min Chen, Zheng Xu, Ziruo Hong, Yang Yang, *J. Mater. Chem.* **2010**, *20*, 2575
- 153 Ankit Kumar, Hua-Hsien Liao, Yang Yang, *Organic Electronics* **2009**, *10*, 1615
- 154 Tracey M. Clarke, Christoph Lungenschmied, Jeff Peet, Nicolas Drolet, Kenji Sunahara, Akihiro Furube, Attila J. Mozer, *Adv. Energy Mater.* **2013**, *3*, 1473
- 155 H. H. Ramanitra, S. A. Dowland, B. A. Bregadiolli, M. Salvador, H. S. Silva, D. Bégué, C. F. O. Graeff, H. Peisert, T. Chassé, S. Rajoelson, A. Osvet, C. J. Brabec, H.-J. Egelhaaf, G. Morse, A. Distler, R. C. Hiorns; *It's ATRAP! OligoPCBM for the stabilisation of polymer:PCBM bulk heterojunctions*, submitted.
- 156 H. W. Kroto, J. R. Heath, S. C. O'Brien, R. F. Curl, R. E. Smalley, *Nature* **1985**, *318*, 162.
- 157 (a) Martín, N.; Sanchez, L.; Illescas, B.; Pérez, I. C. *Chem. Rev.* **1998**, *98*, 2527; (b) Li, C.-Z.; Yip, H. L.; Jen, A. K.-Y. *J. Mater. Chem.* **2012**, *22*, 4161.
- 158 (a) M. Lucafò, M. Gerdol, A. Pallavicini, S. Pacor, S. Zorzet, T. Da Ros, M. Prato, M.; G. Sava, *Toxicology* **2013**, *314*, 183; (b) M. A. Orlova, T. P. Trofimova, A. P. Orlov, O. A. Shatalov, *Br. J. Med. Med. Res.* **2013**, *3*, 1731; (c) M. Lucafò, C. Pelillo, M. Carini, T. Da Ros, M. Prato, G. Sava, *Nano-Micro Lett.* **2014**, *6*, 163.
- 159 Mateo-Alonso, A.; Guldi, D. M.; Paolucci, F.; Prato, M. *Chem., Int. Ed.* **2007**, *46*, 8120.
- 160 Doctoral thesis of A. Distler, 2015, Nürnberg

-
- 161 F. Diederich, R. Ettl, Y. Rubin, R. L. Whetten, R. Beck, M. Alvarez, S. Anz, D. Sensharma, F. Wudl, K. C. Khemani, A. Koch, *Science* **1991**, 252, 548
- 162 C. K. Lee, W. K. Li, *J. Mol. Struct.* **1977**, 38, 253
- 163 M. S. Dresselhaus, G. Dresselhaus, P. C. Eklund, *Science of Fullerenes and Carbon Nanotubes*, Academic Press, **1996**
- 164 C. S. Yannoni, P. P. Bernier, D. S. Bethune, G. Meijer, J. R. Salem, *Journal of the American Chemical Society* **1991**, 113, 3190
- 165 Wanda Śliwa, *Fullerene Science and Technology*, **1995**, 3, 243
- 166 Andreas Hirsch, Michael Brettreich, *Fullerenes: Chemistry and Reactions*, ISBN 3-527-30820-2, © 2005 Wiley-VCH
- 167 C. A. Reed, R. D. Bolskar, *Chem. Rev.* **2000**, 100, 1075
- 168 O. A. Gudaev, V. K. Malinovsky, A. V. Okotrub, Y. V. Shevtsov, *Fullerene Sci. Technol.* **1998**, 6, 433
- 169 E. Frankevich, Y. Maruyama, H. Ogata, *Chem. Phys. Lett.* **1993**, 214, 39
- 170 N. S. Sariciftci, L. Smilowitz, A. J. Heeger, F. Wudl, *Science*, **1992**, 258, 1474.
- 171 L. Smilowitz, N. S. Sariciftci, R. Wu, C. Gettinger, A. J. Heeger, F. Wudl, *Phys. Rev. B*, **1993**, 47, 13835.
- 172 D. Chen, A. Nakahara, D. Wei, D. Nordlund, T. P. Russell, *Nano Lett.* **2011**, 11, 561.
- 173 M. Campoy-Quiles, T. Ferenczi, T. Agostinelli, P.G. Etchegoin, Y. Kim, T.D. Anthopoulos, P. N. Stavrinou, D. D. C. Bradley, J. Nelson, *Nat Mater.* **2008**, 7, 158.
- 174 a) S. Bertho *et al.*, *Solar Energy Materials and Solar Cells* **2008**, 92, 753; b) Li-Min Chen, Ziruo Hong, Gang Li, Yang Yang, *Adv. Mater.* **2009**, 21, 1434
- 175 M. Campoy-Quiles, T. Ferenczi, T. Agostinelli, P. G. Etchegoin, Y. Kim, T. D. Anthopoulos, P. N. Stavrinou, D. C. Bradley, J. Nelson, *Nature Materials* **2008**, 7, 158

-
- 176 Y.-J. Cheng, C.-H. Hsieh, P.-J. Li, C.-S. Hsu, *Adv. Funct. Mater.* **2011**, *21*, 1723; b) J. W. Jung, J. Woong Jo, W. H. Jo, *Adv. Mat.* **2011**, *23*, 1782 c) C.-H. Hsieh, Y.-J. Cheng, P.-Jung Li, C.-H. Chen, M. Dubosc, R.-M. Liang, C.-S. Hsu, *J. Am. Chem. Soc.* **2010**, *132*, 4887
- 177 Marleen H. van der Veen, Bert de Boer, Ulf Stalmach, Karin I. van de Wetering, Georges Hadziioannou, *Macromolecules* **2004**, *37*, 3673
- 178 S. Barrau, T. Heiser, F. Richard, C. Brochon, C. Ngov, K. van de Wetering, G. Hadziioannou, D. V. Anokhin and D. A. Ivanov, *Macromolecules* **2008**, *41*, 2701
- 179 B. Gholamkhash, T. J. Peckham, S. Holdcroft, *Polym. Chem.* **2010**, *1*, 708.
- 180 Z. Tan, J. Hou, Y. He, E. Zhou, C. Yang and Y. Li, *Macromolecules* **2007**, *40*, 1868
- 181 A. Cravino, N. S. Sariciftci, *Nat. Mater.* **2003**, *2*, 360
- 182 F. Giacalone, N. Martín, *Chem. Rev.* **2006**, *106*, 5136
- 183 a) R. C. Hiorns, E. Cloutet, E. Ibarboure, L. Vignau, N. Lemaître, S. Guillerez, C. Absalon, H. Cramail, *Macromolecules*, **2009**, *42*, 3549; b) R. C. Hiorns, E. Cloutet, E. Ibarboure, A. Khoukh, H. Bejbouji, L. Vignau, H. Cramail, *Macromolecules*, **2010**, *43*, 6033.
- 184 a) M. Urien, G. Wantz, E. Cloutet, L. Hirsch, P. Tardy, L. Vignau, H. Cramail, J.-P. Parneix, *Organic Electronics* **2007**, *8*, 727; b) A. Dupuis, P. Wong-Wah-Chung, A. Rivaton, J.-L. Gardette, *Polymer Degradation and Stability* **2012**, *97*, 366
- 185 Hasina H. Ramanitra, Hugo Santos Silva, Bruna A. Bregadiolli, Abdel Khoukh, Craig M. S. Combe, Simon A. Dowland, Didier Bégué, Carlos F. O. Graeff, Christine Dagrón-Lartigau, Andreas Distler, Graham Morse, Roger C. Hiorns, *Macromolecules* **2016**, DOI: 10.1021/acs.macromol.5b02793
- 186 M. Maggini, G. Scorrano, M. Prato, *J. Am. Chem. Soc.* **1993**, *115*, 9798
- 187 Maurizio Prato, Michele Maggini, *Acc. Chem. Res.*, **1998**, *31*, 519

-
- 188 K. Kordatos, S. Bosi, T. Da Ros, A. Zambon, V. Lucchini, M. Prato, *J. Org. Chem.* **2001**, *66*, 2802
- 189 a) A. M. Rao, P. Zhou, K. A. Wang, G. T. Hager, J. M. Holden, Y. Wang, W. T. Lee, X.-X. Bi, P. C. Ecklund, D. S. Cornett, *Science* **1993**, *259*, 955; b) P. Eklund, A. M. Rao, P. Zhou, Y. Wang, J. M. Holden, *Thin Solid Films* **1995**, *257*, 185
- 190 S. G. Penn, D. A. Costa, A. L. Balch, C. B Lebrilla, *International Journal of Mass Spectrometry and Ion Processes*, **1997**, *169/170*, 371
- 191 a) R. F. T. Stepto, R. G. Gilbert, M. Hess, A. D. Jenkins, R. G. Jones, P. Kratochvíl, *Pure Appl. Chem.* **2009**, *81*, 351; b) R. C. Hiorns, R. J. Boucher, R. Duhlev, K. H. Hellwich, P. Hodge, A. D. Jenkins, R. G. Jones, J. Kahovec, G. Moad, C. K. Ober, D. W. Smith, R. F. T. Stepto, J.-P. Vairon, J. Vohlídal, *Pure Appl. Chem.* **2012**, *84*, 2167
- 192 B. Nie, V. M. Rotello, *Macromolecules* **1997**, *30*, 3949
- 193 A. Kraus, K. Müllen, *Macromolecules* **1999**, *32*, 4214
- 194 P. J. Flory, *Principles of Polymer Chemistry*, Cornell University Press, Ithaca, New York, 1953, ch. 8.
- 195 Silvia Marchesan, Tatiana Da Ros, Maurizio Prato, *J. Org. Chem.* **2005**, *70*, 4706
- 196 A. Hirsch, I. Lamparth, H. R. Karfunkel, *Angew. Chem., Int. Ed. Engl.* **1994**, *33*, 437
- 197 a) F. Neese, F. Wennmohs, A. Hansen, U. Becker, *Chemical Physics* **2009**, *356*, 98; b) C. Huber, T. Klamroth, *J. Chem. Phys.* **2011**, *134*, 054113; c) F. Neese, *Wiley Interdisciplinary Reviews: Computational Molecular Science*, **2012**, *2*, 73
- 198 (a) H.W. Kroto, R. Taylor J.P. Hare, *Chemical Physics Letters* **1991**, *177*, 394; (b) S. Leach, M. Vervloet, A. Despres, E. Breheret, J.P. Hare, T.J. Dennis, H. W. Kroto, R. Taylor, D. R. M. Walton, *Chemical Physics* **1992**, *160*, 451.

-
- 199 Y. Matsuo, *Pure Appl. Chem.* 2012, **84**, 945
- 200 S. Huang, G. Zhang, N. S. Knutson, M. T. Fontana, R. C. Huber, A. S. Ferreira, S.H. Tolbert, B. J. Schwartz and Yves Rubin, *J. Mater. Chem. A* 2016, **4**, 416
- 201 M. E. S.-Vergara 1, J. C. A.-Huitron, A. R.-Gómez, Jerry N. R.-Burstin, *Molecules* **2012**, *17*, 10000
- 202 T. T. Ngo, D. N. Nguyen, V. T. Nguyen, *Adv. Nat. Sci.: Nanosci. Nanotechnol.* **2012**, *3*, 045001.
- 203 S. Izawa, K. Hashimoto, K. Tajima, *Chem. Commun.* **2011**, *47*, 6365; b) A. Lafleur-Lambert, S. Rondeau-Gagné, A. Soldera, J.-F. Morin, *Tetrahedron Letters* **2011**, *52*, 5008
- 204 a) J. C. Bijleveld, A. P. Zoombelt, S. G. J. Mathijssen, M. M. Wienk, M. Turbiez, D. M. de Leeuw, R. A. J. Janssen, *J. Am. Chem. Soc.*, **2009**, *131*, 16616; b) J. D. Yuen, J. Fan, J. Seifert, B. Lim, R. Hufschmid, A. J. Heeger, F. Wudl, *J. Am. Chem. Soc.*, **2011**, *133*, 20799; c) J. C. Bijleveld, V. S. Gevaerts, D. Di Nuzzo, M. Turbiez, S. G. J. Mathijssen, D. M. de Leeuw, M. M. Wienk, R. A. J. Janssen, *Adv. Mater.* **2010**, *22*, E242
- 205 Blanco, G. D.; Hiltunen, A. J. Lim, G. N.; KC, C. B.; Kaunisto, K. M.; Vuorinen, T. K.; Nesterov, V. N.; Lemmetyinen, H. J.; D'Souza, F. *ACS Appl. Mater. Interfaces*, DOI: 10.1021/acsami.6b00561.
- 206 Baffreau, J.; Ordronneau, L.; Leroy-Lhez, S.; Hudhomme, P. *J. Org. Chem* **2008**, *73*, 6142.
- 207 Baffreau, J.; Leroy-Lhez, S.; Vân Anh, N.; Williams, R. M.; Hudhomme, P. *Chem. Eur. J.* **2008**, *14*, 4974.
- 208 Pelado, B.; Abou-Chachine, F.; Calbo, J.; Caballero, R.; de la Cruz, P.; Junquera-Hernández, J. M.; Ortéi, E.; Tkachenko, N.; Langa, F. *Chem. Eur. J.* **2015**, *21*, 5814.

-
- 209 D'Souza, F.; Chitta, R.; Ohkubo, K.; Tasior, M.; Subbaiyan, N. K.; Zandler, M. E. Rogacki, M. K.; Gryko, D. T.; Fukuzumi, S. *J. Am. Chem. Soc.*, **2008**, *130*, 14263.
- 210 Das, S. K.; Mahler, A.; Wilson, A. K.; D'Souza, F. *ChemPhysChem* **2014**, *15*, 2462.
- 211 Banerji, N.; Wang, M.; Fan, J.; Chesnut, E. S.; Wudl, F.; Moser, J.-E. *J. Mater. Chem.* **2012**, *22*, 13286.
- 212 Hao, Z.; Iqbal, A. *Chem. Soc. Rev.* **1997**, *26*, 203.
- 213 Karsten, B. P.; Smith, P. P.; Tamayo, A. B.; Janssen, R. A. J. *J. Phys. Chem. A* **2012**, *116*, 1146.
- 214 Bronstein, H.; Chen, Z.; Ashraf, R. S.; Zhang, W.; Du, J.; Durrant, J. R.; Tuladhar, P. S.; Song, K.; Watkins, S. E.; Geerts, Y.; Wienk, M. M.; Janssen, R. A. J.; Anthopoulos, T.; Sirringhaus, H.; Heeney, M.; McCulloch, I. *J. Am. Chem. Soc.* **2011**, *133*, 3272.
- 215 Karsten, B. P.; Bouwer, R. K. M.; Hummelen, J. C.; Williams, R. M.; Janssen, R. A. J. *Photochem. Photobiol. Sci.* **2010**, *9*, 1055.
- 216 Christian J. Mueller, Chetan R. Singh, Martina Fried, Sven Huettner, Mukundan Thelakkat, *Advanced Functional Materials* **2015**, *25*, 2725
- 217 M. Kirkus, L. Wang, S. Mothy, D. Beljonne, J. Cornil, R. A. J. Janssen, S. C. J. Meskers, *J. Phys. Chem. A*, **2012**, 7927.
- 218 (a) W. Hong, B. Sun, H. Aziz, W.-T. Park, Y.-Y. Noh, Y. Li, *Chem. Commun.* **2012**, *48*, 8413; (b) B. P. Karsten, J. C. Bijleveld, R. A. J. Janssen, *Macromol. Rapid Commun.* **2010**, *31*, 1554.
- 219 A. Gügel, P. Belik, M. Walter, A. Kraus, E. Harth, M. Wagner, J. Spickermann, K. Müllen, *Tetrahedron* **1996**, *52*, 5007.
- 220 Ramanitra, H. H.; Santos Silva, H.; Bregadiolli, B. A.; Khoukh, A.; Combe, C. M. S.; Dowland, S. A.; Bégué, D.; Graeff, C. F. O.; Dagron-Lartigau, C.; Distler, A.; Morse, G.; Hiorns, R. C. *Macromolecules* **2016**, *49* (5), 1681.

-
- 221 (a) F. Neese, F. Wennmohs, A. Hansen, U. Becker, *Chem. Phys.* **2009**, 356, 98; (b) C. Huber, T. Klamroth, *J. Chem. Phys.* **2011**, 134, 054113.
- 222 (a) A. D. Becke, *J. Chem. Phys.* **1993**, 98, 5648; (b) C. Lee, W. Yang, R. G. Parr, *Phys. Rev. B* **1988**, 37, 785; (c) S. H. Vosko, L. Wilk, M. Nusair, *Can. J. Phys.* **1980**, 58, 1200; (d) P. J. Stephens, F. J. Devlin, C. F. Chabalowski, M. J. Frisch, *J. Phys. Chem.* **1994**, 98, 11623;
- 223 Stephen, M.; Ramanitra, H. H.; Santos Silva, H.; Dowland, S.; Bégué, D.; Genevičius, K.; Arlauskas, K.; Juška, G.; Morse, G. E.; Distler, A.; Hiorns, R. C. *submitted*.
- 224 Yanai, T.; Tew, D.; Handy, N. *Chem. Phys. Lett.*, **2004**, 393, 51.
- 225 Gordon, M. S.; Binkley, J. S.; Pople, J. A.; Pietro, W. J.; Hehre, W. J. *J. Am. Chem. Soc.* **1982**, 104, 2797.
- 226 M. Schrödner, S. Sensfuss, H. Schache, K. Schultheis, T. Welzel, K. Heinemann, R. Milker, J. Marten, L. Blankenburg, *Sol. Energ. Mat. Sol. Cells* **2012**, 107, 283
- 227 (a) Ankur Solanki, Bo Wu, Teddy Salim, Yeng Ming Lam, Tze Chien Sum, *Phys.Chem.Chem.Phys.* **2015**, 17, 26111; (b) Jenny Clark, Carlos Silva, Richard H. Friend, Frank C. Spano, *Physical Review Letters* **2007**, 98, 206406; (c) Vishal Shrotriya, Jianyong Ouyang, Ricky J. Tseng, Gang Li, Yang Yang, *Chemical Physics Letters* **2005**, 411, 138
- 228 J. Peet, L. Wen, P. Byrne, S. Rodman, K. Forberich, Y. Shao, N. Drolet, R. Gaudiana, G. Dennler, D. Waller, *Applied Physics Letters* **2011**, 98, 043301
- 229 Craig H. Peters, I. T. Sachs-Quintana, William R. Mateker, Thomas Heumueller, Jonathan Rivnay, Rodigo Noriega, Zach M. Beiley, Eric T. Hoke, Alberto Salleo, Michael D. McGehee, *Advanced Materials* **2012**, 24, 663
- 230 F. Neese, *WIREs Comput Mol Sci*, **2012**, 2, 73
- 231 (a) A. D. Becke, *J. Chem. Phys.* **1993**, 98, 5648; (b) C. Lee, W. Yang, R. G. Parr, *Phys. Rev. B* **1988**, 37, 785; (c) S. H. Vosko, L. Wilk, M. Nusair, *Can. J.*

Phys. **1980**, *58*, 1200; (d) P. J. Stephens, F. J. Devlin, C. F. Chabalowski, M. J. Frisch, *J. Phys. Chem.* **1994**, *98*, 11623; (d) T. Yanai, D. Tew, N. Handy, *Chem. Phys. Lett.* **2004**, *393*, 51.